Title
Pore Control in Mesoporous Silica for Cargo Delivery and Sensing Applications

Author
Russell, Melissa Mei-Lee

Publication Date
2013

Peer reviewed|Thesis/dissertation

UNIVERSITY OF CALIFORNIA

Los Angeles

Pore Control in Mesoporous Silica for Cargo Delivery and Sensing Applications

A dissertation submitted in partial satisfaction of the requirements for the degree Doctor of Philosophy in Chemistry

by

Melissa Mei-Lee Russell

2013

ABSTRACT OF THE DISSERTATION

Pore Control in Mesoporous Silica for Cargo Delivery and Sensing Applications

by

Melissa Mei-Lee Russell

Doctor of Philosophy in Chemistry

University of California, Los Angeles, 2013

Professor Jeffrey I. Zink, Chair

Mesoporous silica materials can range from films to nanoparticles. Due to the Si-OH groups on the surface of the materials they can be functionalized to control the pore openings. Some examples of these functionalizations are the attachment of polymers or molecules that serve as a pore cap. This leads to a wide variety of applications because of their ability to contain cargo molecules. The work covered in this thesis focuses on the development of different mesoporous silica materials for the purpose of trapping various cargo molecules for cargo delivery and sensing applications. The first project discusses the

thermal trapping and release of cargo molecules of a mesoporous silica film with a thermal sensitive polymer attached to the surface. The second project focuses on a light activated polymer attached to MCM-41 silica nanoparticles and the delivery of fluorescent molecules inside of cells. The third project discussed in this thesis utilizes hollow mesoporous silica nanoparticles to crystalize a perchlorate sensor inside the core to be used as “smart sand” for perchlorate detection. The last project focuses on periodic mesoporous organosilica (PMO) nanoparticles and their ability to trap and release cargo molecules. This research demonstrates the versatility of mesoporous silica materials and its potential in both microscopic and macroscopic applications.

The dissertation of Melissa Mei-Lee Russell is approved.

Richard B. Kaner

Fuyuhiko Tamanoi

Jeffrey I. Zink, Committee Chair

University of California, Los Angeles

2013

This dissertation is dedicated to my most loving parents, Thomas and Beverly Russell, my sister, Katrina Russell, and Cameron Zuber.

TABLE OF CONTENTS

LIST OF TABLES AND FIGURES

Chapter 2 Temperature Controlled Poly(NIPAAm-co-AAm) Modified Mesoporous Thin Films For Pore Control

Chapter 3 Light Activated MCM-41 Silica Nanoparticles Using an Azobenene Based Polymer

Chapter 4 Hollow Mesoporous Silica Nanoparticles Loaded with a Perchlorate Sensor

Chapter 5 PMOs Mechanized with an Acid Valve

ACKNOWLEDGEMENTS

I would first like to acknowledge my advisor, Professor Jeffery I. Zink, for accepting me into his group. He gave me the opportunity to learn about different fields by allowing me to work on so many different projects with various applications. I would like to thank my committee members, Professor Richard Kaner and Fuyuhiko Tamanoi. I would also like to thank my collaborators from Microbiology and Molecular Genetics: Fuyuhiko Tamanoi and his postdoc Jie Lu and my collaborators from the University of Cincinnati in Professor William Connick's group.

I would also like to thank all past and present Zink group members. I am fortunate to call Matt Kiesz, Min Xue, and Derrick Tarn my classmates and my friends. Especially Tania Guardado for all her help, collaborations, and most importantly, her friendship. The five of us joined Professor Zink's lab at the same time and I am so happy that we are able to get our Ph.D.'s together.

Lastly, I would like to thank my most loving family. I hope that I have and continue to make my parents proud. Without their support and their confidence in me when I had none, I would not be getting my Ph.D. This is as much their accomplishment as well as mine. I would like to thank my sister for her support and reassurance. She is truly the best "big sister" anyone could ask for. To my future mother-in-law, her kindness and generosity towards me has been a blessing. Finally, I would like to thank for all his love, support, patience, and always wanting what is best for me, my future husband, Cameron. I cannot thank my family enough for all they have given me.

VITA

1985	Born, San Mateo, California
2007	B.S. Chemistry University of California Davis, California
2008-2010, 2012-2013	Teaching Assistant Department of Chemistry and Biochemistry University of California, Los Angeles Los Angeles, California
2010-2012	Research Assistant Zink Research Group

PUBLICATIONS

Russell, Melissa M.; Raboin, Lorraine; Guardado-Alvarez Tania M.; Zink, Jeffrey I. "Temperature Controlled Poly(NIPAAm-co-AAm) Modified Mesoporous Thin Films for Pore Control". (Submitted)

Russell, Melissa M.; Norton, Amie E.; Connick, William B.; Zink, Jeffrey I. "Activatible Perchlorate Sensor based on Mechanized Hollow Mesoporous Silica Nanoparticles". (In Preparation)

Guardado-Alvarez, Tania M.; Sudha Devi, Lekshmi; **Russell, Melissa M.**; Schwartz, Benjamin; Zink, Jeffrey I. "Activation of Snap-top Capped Mesoporous Silica Nano Containers Using Two Near-Infrared Photons". (Submitted)

Chapter 1

Mesoporous Silica Materials by the Sol-Gel Process

1.1 The Sol-Gel Process

Materials prepared by the sol-gel process have become the basis of an important field of research in materials science. Since the 1970's, sol-gel chemistry has been researched extensively and has shown to produce a variety of inorganic networks.[1] The sol-gel process is a set of reactions that convert an aqueous metal alkoxide, with a molecular formula of $M(OR)_n$ into an inorganic network.[1, 2] This process is able to produce homogeneous, high purity inorganic oxide glasses at room temperature, which is much lower than the high temperatures required by normal glass manufacturing processes. One important advantage of the sol-gel process is its ability to form different types of materials such as, thin films,[3-5] spun fibers,[6, 7] particles,[8-11] aerogels,[12, 13] and xerogels.[14, 15]

1.1.1 Hydrolysis and Condensation

The sol-gel process is the transformation of a sol to a gel.[2, 16] A sol is a colloid of small particles that are well dispersed in a liquid. A gel is made up of a continuous network that also includes a continuous liquid phase.[16-18] The sol-gel process is therefore a series of hydrolysis and condensation reactions of the inorganic alkoxide monomers that forms colloidal particles (sol) and converts them into a continuous network (gel). Tetraethylorthosilicate (TEOS) has been extensively used for the production of silica gels.[3, 10, 11, 19] The hydrolysis step of TEOS is depicted in Equation 1:

Equation 1: $Si(OEt)_4 + H_2O \rightarrow HO\text{-}Si(OEt)_3 + EtOH$

This step takes under neutral conditions and leads to the generation of a silanol group (Si-OH) and an alcohol. The second step is the condensation of the silanol group and can occur in two different ways and is depicted in Equation 2.1 and Equation 3:

Equation 2: $HO\text{-}Si(OEt)_3 + HO\text{-}Si(OEt)_3 \rightarrow (EtO)_3\text{-}Si\text{-}O\text{-}Si(OEt)_3 + H_2O$

Equation 3: $HO\text{-}Si(OEt)_3 + Si(OEt)_4 \rightarrow (EtO)_3\text{-}Si\text{-}O\text{-}Si(OEt)_3 + EtOH$

The silanol group condenses with either another silanol group or with an alkoxide to create a siloxane bond (Si-O-Si) with the loss of water or an alcohol. As the reaction continues, the number of siloxane bonds increase forming siloxane colloids, which forms the sol. From there, the colloids aggregate and condense further to form a continuous network that spans the solution forming the gel.

1.1.2 Acid/Base Catalysis

The hydrolysis reactions of TEOS are strongly affected by the presence of an acid or base catalyst.[16-18, 20] If an acid catalyst is present, the hydrolysis step involves and electrophilic attack of the proton on the alkoxide oxygen atom. This yields a positive charge on the oxygen. The bond between the silicon center and the attacked oxygen becomes more polarized, which later facilitates the departure of the alcohol group.[21] The oxygen on the

water molecule attacks the silicon and forms a penta-coordinated transition state in which the silicon center is partially bonded to both the water and the positively charged alcohol group. The alcohol then leaves and the silanol bond is formed after the loss of a hydrogen from the water. For a base catalyzed reaction, the –OH attacks the Si and forms the penta-coordinated transition state first and then the alcohol group leaves forming $HO\text{-}Si(OEt)_3$. Also, the rate of hydrolysis is much faster under acidic conditions than basic conditions.

The condensation rates and mechanisms are also dependent on the pH of the reaction. Under acidic conditions the condensation reactions happens in two steps.[22] The first step is the electrophilic attack of the proton on the oxygen of the silanol group results in the silanol oxygen becoming positively charged. The second step is the formation of the siloxane bond after the loss of the hydronium cation as a result of the reaction between a protonated silanol group and an unprotonated one. Under basic conditions the condensation reaction also happens in two steps.[2, 16] However, in this reaction the hydrogen on the silanol group gets deprotonated by the hydroxide ion and leaves a negatively charged oxygen on the silanol. The siloxane linkage is then formed through an SN2 attack of the latter ion onto the silicon center of a different silanol group and regenerates the hydroxide ion. The condensation rate under basic conditions is also faster than that under acidic conditions.

Since the hydrolysis rates and condensation rates differ depending on the catalyst, the structure of the network, as the sol is allowed to gel, will also differ. For acid catalysis the hydrolysis reaction is faster than the condensation reaction. This produces networks with less siloxane bonds and a higher concentration of silanol groups, yielding more

linearly branched polymeric species. This is highly favorable for the formation of thin films. Films experience internal stress that is caused by non-uniform evaporation of the solvent and inhomogeneous shrinkage. Less condensed silica alleviates this stress since it is more flexible and creates materials with fewer cracks. On the other hand, the condensation reaction is much faster using base as a catalyst. Therefore, there are fewer silanol groups in the network. The network is then consisted of highly branched clusters, which yields highly dense materials. This is important for the formation of particles.

1.2 Mesoporous Silica Materials

Mesostructured silica particles were discovered in 1992 and have since been a subject of intensive research due to the materials having a large surface area and having the ability to modify the particle and pore size.[23, 24] These mesoporous materials are formed by the assembly of inorganic species and organic surfactants. The structure of the mesoporous materials is based on the fact that the surfactant molecules form different structures depending on the concentration of the surfactant in the sol.[25] At very low concentrations, the surfactant molecules exist as monomolecules, but with increasing concentration they combine together and form micelles and decrease the system entropy.[25-27] These micelles then aggregate together and the alkoxysilanes condense around the structure. The surfactant can then be removed through calcination[28, 29] or through solvent extraction[30, 31] forming the mesotructured silica material.

1.3 Functionalized Mesoporous Silica Materials

Sol-gel chemistry also allows the introduction of organic functionalities in the pore walls and on the surface of mesoporous.[32, 33] The surface of the materials can be modified post-synthesis and, after the removal of the surfactant, the pore walls can be modified as well. Mesoporous silica materials possess silanol groups that facilitate the attachment of organic groups onto the silica surface. The most common way to functionalize the mesoporous materials is through silylation[33] which is when the organic group contains silanol groups that can condense onto the surface in a similar fashion described in Equation 3. Silylation happens on all surface silanol groups and allows the mesoporous structure to be maintained after the modification.

Surface functionalized mesoporous silica materials are of particular interest because of their potential use in a variety of applications.[1] One in particular is the growing interest in trapping guest molecules inside the pores.[3, 9, 34, 35]

1.4 Materials Discussed in Thesis

Herein, the study of trapping guest molecules inside different types of mesoporous silica materials is explored. Chapter 2 focuses on mesostructured sol-gel thin films formed by evaporation induced self-assembly (EISA).[36, 37] A sol containing a silica precursor and a template agent is deposited as a thin liquid layer onto a suitable substrate. The evaporation of the solvent drives the formation of surfactant micelles, which further assembles into a

liquid crystal. At the same time the silica condenses around the micelles. The surfactant molecules can be removed from the pores of the film by solvent extraction or calcination, thus giving the possibility to fill the empty pores with nano-sized cargos.

The rest of the thesis focuses on nanoscale devices, in particular mechanized silica nanoparticles. Chapter 3 focuses on MCM-41 type particles for biological applications. These particles are rigid, robust, chemically inert, and relatively easy to make.[38-40] Chapter 4 explores how hollow mesoporous silica nanoparticles can be used to create a core/shell nanoparticle. The hollow cavity can act as a reservoir, which can be controllably filled with a different material than the shell and thus create a particle with properties that are not available in normal one component nanoparticles.[41] Chapter 5, the last chapter, focuses on nanoparticles that are made up of organic/inorganic components called "periodic mesoporous organosilicas", or PMOs.[42-44] This allows the particles to be imbued with different properties.

1.5 References

1. Al-Othman, Z. A., A Review: Fundamental Aspects of Silicate Mesoporous Materials. Materials 2012, 5, 2874-2902.

2. Brinker, C. J.; Scherer, G. W., Sol-gel science: the physics and chemistry of sol-gel processing. Academic Pr: 1990.

3. Klichko, Y.; Khashab, N. M.; Yang, Y.-W.; Angelos, S.; Stoddart, J. F.; Zink, J. I., Improving pore exposure in mesoporous silica films for mechanized control of the pores. Microporous and Mesoporous Materials 2010, 132, 435-441.

4. Johansson, E.; Zink, J. I., Nanostructured Silica Thin Films Self-Assembled with Electron Donors and Acceptors to Measure Electron Tunneling. Journal of the American Chemical Society 2007, 129, 14437-14443.

5. Koganti, V. R.; Rankin, S. E., Synthesis of surfactant-templated silica films with orthogonally aligned hexagonal mesophase. The Journal of Physical Chemistry B 2005, 109, 3279-3283.

6. Lee, S. W.; Kim, Y. U.; Choi, S.-S.; Park, T. Y.; Joo, Y. L.; Lee, S. G., Preparation of SiO< sub> 2</sub>/TiO< sub> 2</sub> composite fibers by sol–gel reaction and electrospinning. Materials Letters 2007, 61, 889-893.

7. Choi, S.-S.; Lee, S. G.; Im, S. S.; Kim, S. H.; Joo, Y. L., Silica nanofibers from electrospinning/sol-gel process. Journal of materials science letters 2003, 22, 891-893.

8. Wu, S.-H.; Mou, C.-Y.; Lin, H.-P., Synthesis of mesoporous silica nanoparticles. Chemical Society Reviews 2013.

9. Vallet-Regí, M., Mesoporous Silica Nanoparticles: Their Projection in Nanomedicine. ISRN Materials Science 2012, 2012.

10. Li, Z.; Barnes, J. C.; Bosoy, A.; Stoddart, J. F.; Zink, J. I., Mesoporous silica nanoparticles in biomedical applications. Chemical Society Reviews 2012, 41, 2590-2605.

11. Ambrogio, M. W.; Thomas, C. R.; Zhao, Y.-L.; Zink, J. I.; Stoddart, J. F., Mechanized silica nanoparticles: a new frontier in theranostic nanomedicine. Accounts of chemical research 2011, 44, 903-913.

12. Hüsing, N.; Schubert, U., Aerogels—airy materials: chemistry, structure, and properties. Angewandte Chemie International Edition 1998, 37, 22-45.

13. Pierre, A. C.; Pajonk, G. M., Chemistry of aerogels and their applications. Chemical Reviews-Columbus 2002, 102, 4243-4266.

14. Fields, S. M., Silica xerogel as a continuous column support for high-performance liquid chromatography. Analytical chemistry 1996, 68, 2709-2712.

15. Huang, H. Y.; Yang, R. T.; Chinn, D.; Munson, C. L., Amine-grafted MCM-48 and silica xerogel as superior sorbents for acidic gas removal from natural gas. Industrial & engineering chemistry research 2003, 42, 2427-2433.

16. Brinker, C. J., Sol-gel processing of silica. Advances in Chemistry Series 1994, 234, 361-361.

17. Ng, L. V.; Thompson, P.; Sanchez, J.; Macosko, C. W.; McCormick, A. V., Formation of cagelike intermediates from nonrandom cyclization during acid-catalyzed sol-gel polymerization of tetraethyl orthosilicate. Macromolecules 1995, 28, 6471-6476.

18. Wen, J.; Wilkes, G. L., Organic/inorganic hybrid network materials by the sol-gel approach. Chemistry of Materials 1996, 8, 1667-1681.

19. Klein, L., Sol-gel processing of silicates. Annual Review of Materials Science 1985, 15, 227-248.

20. Alberius, P. C. A.; Frindell, K. L.; Hayward, R. C.; Kramer, E. J.; Stucky, G. D.; Chmelka, B. F., General Predictive Syntheses of Cubic, Hexagonal, and Lamellar Silica and Titania Mesostructured Thin Films §. Chemistry of Materials 2002, 14, 3284-3294.

21. Schmidt, H.; Scholze, H.; Kaiser, A., Principles of hydrolysis and condensation reaction of alkoxysilanes. Journal of Non-Crystalline Solids 1984, 63, 1-11.

22. Hench, L. L.; West, J. K., The sol-gel process. Chemical Reviews 1990, 90, 33-72.

23. Beck, J. S.; Vartuli, J. C.; Roth, W. J.; Leonowicz, M. E.; Kresge, C. T.; Schmitt, K. D.; Chu, C. T. W.; Olson, D. H.; Sheppard, E. W., A new family of mesoporous molecular sieves prepared with liquid crystal templates. Journal of the American Chemical Society 1992, 114, 10834-10843.

24. Stein, A.; Melde, B. J.; Schroden, R. C., Hybrid inorganic–organic mesoporous silicates—nanoscopic reactors coming of age. Advanced Materials 2000, 12, 1403-1419.

25. Broekhoff, J., Mesopore Determination from Nitrogen Sorption Isotherms: Fundamentals, Scope, Limitations. Studies in Surface Science and Catalysis 1979, 3, 663-684.

26. Zhao, X. S.; Lu, G.; Millar, G. J., Advances in mesoporous molecular sieve MCM-41. Industrial & engineering chemistry research 1996, 35, 2075-2090.

27. Steel, A.; Carr, S. W.; Anderson, M. W., 14 N NMR study of surfactant mesophases in the synthesis of mesoporous silicates. J. Chem. Soc., Chem. Commun. 1994, 1571-1572.

28. Dattelbaum, A. M.; Amweg, M. L.; Ruiz, J. D.; Ecke, L. E.; Shreve, A. P.; Parikh, A. N., Surfactant removal and silica condensation during the photochemical calcination of thin film silica mesophases. The Journal of Physical Chemistry B 2005, 109, 14551-14556.

29. Kleitz, F.; Schmidt, W.; Schüth, F., Calcination behavior of different surfactant-templated mesostructured silica materials. Microporous and mesoporous materials 2003, 65, 1-29.

30. Hua, Z.-L.; Shi, J.-L.; Wang, L.; Zhang, W.-H., Preparation of mesoporous silica films on a glass slide: surfactant template removal by solvent extraction. Journal of non-crystalline solids 2001, 292, 177-183.

31. Doyle, A.; Hodnett, B., Synthesis of 2-cyanoethyl-modified MCM-48 stable to surfactant removal by solvent extraction: Influence of organic modifier, base and surfactant. Microporous and mesoporous materials 2003, 58, 255-261.

32. Brinker, C., Hydrolysis and condensation of silicates: effects on structure. Journal of Non-Crystalline Solids 1988, 100, 31-50.

33. Anwander, R., SOMC@ PMS. Surface organometallic chemistry at periodic mesoporous silica. Chemistry of materials 2001, 13, 4419-4438.

34. Rieter, W. J.; Taylor, K. M.; Lin, W., Surface modification and functionalization of nanoscale metal-organic frameworks for controlled release and luminescence sensing. Journal of the American Chemical Society 2007, 129, 9852-9853.

35. Wang, Y.; Price, A. D.; Caruso, F., Nanoporous colloids: building blocks for a new generation of structured materials. Journal of Materials Chemistry 2009, 19, 6451-6464.

36. Klichko, Y.; Khashab, N. M.; Yang, Y.-W.; Angelos, S.; Stoddart, J. F.; Zink, J. I., Improving pore exposure in mesoporous silica films for mechanized control of the pores. *Microporous and Mesoporous Materials* 2010, 132, 435-441.

37. Brinker, C. J.; Lu, Y.; Sellinger, A.; Fan, H., Evaporation-induced self-assembly: nanostructures made easy. *Advanced Materials* 1999, 11, 579-585.

38. Brinker, C. J.; Scherer, G. W., *Sol-gel science: the physics and chemistry of sol-gel processing*. Academic Pr: 1990.

39. Ogawa, M., A simple sol–gel route for the preparation of silica–surfactant mesostructured materials. *Chemical Communications* 1996, 1149-1150.

40. Trewyn, B. G.; Slowing, I. I.; Giri, S.; Chen, H.-T.; Lin, V. S.-Y., Synthesis and functionalization of a mesoporous silica nanoparticle based on the sol–gel process and applications in controlled release. *Accounts of chemical research* 2007, 40, 846-853.

41. Lee, I. S.; Lee, N.; Park, J.; Kim, B. H.; Yi, Y.-W.; Kim, T.; Kim, T. K.; Lee, I. H.; Paik, S. R.; Hyeon, T., Ni/NiO core/shell nanoparticles for selective binding and magnetic separation of histidine-tagged proteins. *Journal of the American Chemical Society* 2006, 128, 10658-10659.

42. Asefa, T.; MacLachlan, M. J.; Coombs, N.; Ozin, G. A., Periodic mesoporous organosilicas with organic groups inside the channel walls. *Nature* 1999, 402, 867-871.

43. Inagaki, S.; Guan, S.; Fukushima, Y.; Ohsuna, T.; Terasaki, O., Novel mesoporous materials with a uniform distribution of organic groups and inorganic oxide in their frameworks. *Journal of the American Chemical Society* 1999, 121, 9611-9614.

44. Hoffmann, F.; Fröba, M., Vitalising porous inorganic silica networks with organic functions—PMOs and related hybrid materials. *Chemical Society Reviews* 2011, 40, 608-620.

Chapter 2

Temperature Controlled Poly(NIPAAm-co-AAm) Modified Mesoporous Thin Films For Pore Control

2.1 Introduction

Mesoporous silica materials, prepared by sol–gel methods, have been of great interest because of their many attractive features, such as stable mesoporous structures, large surface areas, tunable pore sizes, and the simplicity in modifying the inside pores with organic groups.[1-5] The nanopores exhibit narrow pore size distributions in the range of 2-50 nm to store a wide variety of molecules.[6, 7] Accordingly, these materials have been studied for many applications including catalysis,[8-10] medical drug delivery,[6, 11, 12] or separation technology.[2, 13, 14]

Mesostructured sol-gel thin films formed by evaporation induced self assembly (EISA) during dip- or spin-coating have also been studied.[15-21] A sol containing a silica precursor and a template agent is deposited as a thin liquid layer onto a suitable substrate. The evaporation of the solvent drives the formation of surfactant micelles, which further assembles into a liquid crystal. At the same time the silica condenses around the micelles. By choosing a specific composition of the sol, environmental conditions, and the method of deposition, mesostructured films with highly-ordered hexagonal, lamellar, or cubic structures can be produced.[20, 22] The surfactant molecules can be removed from the pores of the film by solvent extraction or calcination, thus giving the possibility to fill the empty pores with nano-sized cargos. The release of stored molecules in the nanopores is attracting increasing interest because a macro-substrate can be more easily handled and manipulated than nanospheres. Thin films containing mesopores would be very convenient if the openings of the nanopores were accessible to molecules outside of the films.

Many efforts have been made to prepare films in which the pore openings are oriented towards the surface of the films.[23-27] Unfortunately such procedures remain extremely complex and difficult, involve the use of polymers, or the types of surfactants that can be used are limited. Another method to make silica films with vertical pores can take up to three days to just make the film.[28] An alternative approach consists of preparing a film with a well-known structure such as a 2D-hexagonal structure in which arrays of tubes in highly arranged stacks are aligned parallel to the upper surface of the films, then etching away selectively narrow regions of the film that are perpendicular to the nanopore orientation. This procedure allows for the creation and the exposure of pore openings. Such films, with a pore diameter of 2.5 nm, have been previously prepared by Klichko et al.[29] Based on these patterned films, a molecular storage and on-demand release system was realized. In this chapter, an improved material that allows more cargo to be stored inside the pores. By changing the surfactant from CTAB to F127 the pore size changes from ~2 nm to ~5 nm. This material could be useful in biomedical applications to deliver larger doses of drugs as well as the potential to deliver larger cargo molecules. In order to test the loading capacity of this material, a well studied synthetic responsive co-polymer, poly(N-isopropylacrylamide-co-Acrylamide) (poly(NIPAAm-co-AAm)), which undergoes a sharp coil–globule transition in water at 41 °C, changing from a hydrophilic state below this temperature, to a hydrophobic state above it.[30-33] The temperature at which this occurs is called the lower critical solution temperature (LCST). While this polymer has been used on silica to release cargo, the results have been either leaky or releases at room temperature.[34-36] Due to the pores being aligned horizontally, the grafted polymer acts as a

gate. At room temperature the polymer stands erect in front of the pores, entrapping the cargo inside. Above the LCST the polymer collapses allowing the cargo to flow freely out of the pores. Since the polymer is also covalently attached onto the surface of the film, after an initial release, the films can be re-loaded with cargo to preform a second release. The overall system is depicted in Figure 2.1.

2.2 Experimental Section

2.2.1 Preparation of Mesoporous Silica Films

Three porous silica films were synthetized with different pore diameters. The three different pore sizes were obtained using different silica templates. Large pore films (pore size 5.5 nm) were prepared using triblock copolymers as templates, while small pore films (pore size 2.5 nm) were produced by surfactant templating. Additional microporous films (pore size < nm) were created using no template.

Synthetic Procedure

Mesostructured silica films were synthesized according to a two-step process as previously reported.[22, 37] First, a stock solution was prepared by mixing TEOS [$Si(OC_2H_5)_4$], absolute ethanol, water and HCl (mole ratios 1 : 3.8 : 1 : $5x10^{-5}$), and heating at 60 °C for 1.5 hrs. Then, a 7.5 mL sample of this initial solution was cooled to room temperature and

mixed to 1 mL of 0.07 M HCl and 0.35 mL of water. After stirring for 15 min, the mixture was allowed to age for 15 min. without stirring, followed by dilution with two equivalents of absolute ethanol. Finally, after the sol was aged for 3 days, triblock copolymer poly(ethyleneoxide$_{106}$-propyleneoxide$_{70}$-ethyeleneoxide$_{106}$) (Pluronic F127) or cethyltrimethylammonium bromide (CTAB) was added. The surfactant/TEOS mole ratios were 0.007 for Pluronic F127 and 0.1 for CTAB, respectively. An additional mixture was prepared without adding surfactant into the silica sol.

The as-prepared mixtures were dip-coated on silicon or glass substrates at a constant speed of 3 mm s^{-1} to yield the mesostructured films. Before deposition, the substrates were soaked in a 1M HNO_3 solution overnight, then rinsed with water, ethanol and acetone, to remove contaminates. The entire film-pulling apparatus was placed inside a controlled-humidity chamber. The relative humidity was fixed to 35 ± 5% when using Pluronic F127, and 55 ± 5% when using CTAB. This results in several hundred nanometer thick crack-free films. Only one side of the substrate consists of the mesostructured film as the other side was cleaned using dilute HF.

Stamp Preparation and Micropatterning

An AFM calibration grating (Mikromasch TGZ04) was used as a source of the pattern. The pattern consists in lines 1.5 μm wide, 1 μm high, with 3 μm pitch. A poly(dimethylsiloxane) (PDMS, Sylgard 184) mixture was poured onto the grating and heated at 100 °C until it solidified. The PDMS stamp was then removed from the grating

surface, rinsed with ethanol and dried in air. The micropatterned films were prepared by gently pressing the PDMS stamp onto the surface of the as-synthetized films right after the dip-coating. The films covered with the stamp were heated at 100 °C for 30 min then allowed to cool at room temperature. The stamp was delicately peeled off using tweezers. A successful pattern transfer leaves a visible indication as a diffraction effect is observed at the film surface. The micropatterned mesostructured films were heated at 100 °C overnight to consolidate the silica network. Finally, the films were calcined at 500 °C for 5 hrs. in air to remove the template, and stored in a vacuum sealed desiccator. The mesoporosity of the films was verified by XRD and TEM.

MEH-PPV Incorporation

First, the inner pore surface of the patterned films was made hydrophobic to aid in incorporation of the fluorescent polymer (MEH-PPV). The films were treated with a solution of dimethyldichlorosilane in dry toluene in presence of triethylamine as an activating base. After reaction, the films were washed with ethanol and water, and cured at 100°C for 1 hr. To incorporate the polymer MEH-PPV (average Mn = 40 000 - 70 000 Da) into the pores, the hydrophobic films were soaked in a 1% solution of MEH-PPV in cholorobenzene for 48 hrs. at 80 °C. The samples were extensively washed with chlorobenzene and chloroform, dried in air, and stored in a dark nitrogen atmosphere.

2.2.2 Synthesis of Thermoresponsive Silica Films

Polymerization of Poly(NIPAAm-co-AAm)

NIPAAm (3.66 g), AAm (0.26 g), N,N,N',N'-pentamethyldiethylenetriamine (PMDETA) (35 µl), 2-bromo-2-methyl propionic acid (0.01 g), deionized water (36 ml) and methanol (24 ml) were mixed in a Schlenk flask and degassed by freeze-pump-thaw cycles. While the mixture was frozen, CuBr (0.01 g) was added. The flask was then filled with argon and the mixture was left to melt at room temperature. The reaction solution was magnetically stirred overnight at room temperature. After evaporation of the solvent, the crude product was dissolved in water and purified by dialysis to yield poly(NIPAAm-co-AAm) with an LCST close to 41 °C.

Surface Modification of Films

The films were soaked in a 0.01 M solution of 3-aminopropyltriethoxysilane (APTES) in dry toluene under nitrogen and stirred at reflux overnight. Finally the surface were extensively rinsed with dry toluene and dried in vacuum. 50 mg of poly(NIPAAm-co-AAm) is dissolved in 10 ml of deionized water. 50 mg of 1-Ethyl-3-(3-dimethylaminopropyl)carbodiimide (EDAC) was added and the amine modified silica film was immediately added afterwards. The solution was stirred overnight at room temperature. After the reaction, the films were removed from the solution, extensively

rinsed with deionized water and dried in vacuum. The surface modification was confirmed from by FTIR and AFM.

Dye Loading and Release Studies

Poly(NIPAAm-co-AAm) modified patterned films were loaded with propidium iodide as a fluorescent dye. The film was submerged in a 2 mM propidium iodide solution (10 mL), heated to 50 °C (> LCST), and left stirring for 24 hrs. Afterwards, the loaded film was removed from the solution, thoroughly rinsed with room temperature water, and used for release studies right away to avoid propidium iodide degradation.

The operation of the thermoresponsive films was monitored using fluorescence spectroscopy. A small 1 cm x 1 cm film (size of pattern 0.8 cm x 0.8 cm) was placed on the bottom of a cuvette. 6 mL of deionized water and a small stir-bar were added. The sealed cuvette was placed on a temperature-controlled plate. The emission of propidium iodide in the solution above the film was measured as a function of time by using a 377 nm excitation beam (10 mW) to excite the dye molecules as they are released from the film. The emission spectrum was recorded as a function of time at 1 second intervals. The release profiles were obtained by plotting luminescence intensities of propidium iodide at the emission maximum (650 nm) as a function of time. The release of the cargo dye was activated by increasing the aqueous media temperature from room temperature (< LCST) to 45 °C (> LCST).

2.2.3 Characterization Methods

The structure of mesostructured silica films were investigated by X-ray diffraction (XRD) experiments in Bragg-Brentano geometry (θ-2θ) on a Philips X'Pert Powder Diffractometer operated at 40 kV, 40 mA using CuKα radiation (λ=1.54 Å). For the observation of the mesoporous films with transmission electron microscopy (TEM), the films were detached from the substrates and dispersed in ethanol, then deposited and dried on a carbon Cu grid. Micrographs were recorded on a JEM1200-EX (JEOL) electron microscope operating at 50 kV. Infrared (FTIR) measurements were acquired on a Jasco Model 420 spectrometer after the samples were dehydrated under vacuum for 5 hrs. at room temperature. The thickness and the surface morphology of the patterned films were determined by atomic force microscopy (AFM) on a Dimension 5000 instrument in contact mode. For fluorescence depolarization measurements, mesoporous films treated with the MEH-PPV polymer were illuminated using the 407 nm line of a Coherent I302C krypton ion laser (10 mW). A polarizer was used to select out parallel and perpendicular emission components. A 420 nm filter was placed in front of the polarizer to block stray laser light. The photoluminescence spectra of the samples were collected throughout the visible region using an Acton 2300i monochromator and a Princeton Instruments CCD. Fluorescence microscopy images of poly(NIPAAm-co-AAm) derivatized patterned films were acquired on a Leica confocal SP5 MP-STED microscope. The films were loaded with Rhodamine B, then the pores were closed, sealing the dye inside the pores. The excess dye on the surface was washed off.

The LCST was measured spectrosphotometrically with a polymer solution being heated 1 °C every three minutes. When the light transmittance is 90% of the original transmittance (at 450nm), is defined as the LCST. The average molecular weight (Mn) and polydispersity index (PDI) of the polymer was measured by Gel Permeation Chromatograph (GPC) using a Waters 515 Differential Refactometer with Waters 410 HPLC pump and two styrage HR 5E columns in THF (0.1 mg/L) as an eluent at 42 °C, calibrated with polystyrene standards.

2.3 Results and Discussion

2.3.1 Micropatterned Nanoporous Silica Films

In this section, a method for the preparation of mesoporous films with a significant accessibility to the pore openings is reported. While the nanopore orientation can easily be controlled in the plane of the film,[38-40] it is difficult to synthetize films in which the pores are running perpendicular to the film surface. Only few reports show a successful orientation of the pore openings toward the upper surface,[23-26] The procedure remains difficult and a limited number of surfactants can be handled, that restricts the range of pore sizes that can be studied. Thus, to cause accessibility to the interior of the films *via* the nanopores, a simple dry-stamping procedure that selectively removes narrow regions of a film that are perpendicular to the pore orientation was implemented. The films preferentially consist of highly arranged arrays of aligned tubes in the plane of the films.

Organized Mesostructured Silica Films

The first step consists in preparing organized nanostructured films with various pore sizes. The films studied were prepared through evaporation-induced self-assembly (EISA).[21, 22] Ordered mesostructured films were obtained using F127 and CTAB as templates. Dip-coating was used to deposit the films rather than spin-coating to have a preferential orientation of the pores along the direction of the pull. The XRD patterns of the as-synthetized films are consistent with a 2D-hexagonal mesostructure with lattice spacings of 114 Å and 39.4 Å for F127 and CTAB, respectively (Figure 2.2). This is confirmed by TEM characterization (Figure 2.3). The micrographs show straight mesochannels regularly arrayed parallel to the substrate with a wall-to-wall distance estimated to around 10 nm and 6 nm for F127 and CTAB, respectively. Additional films were prepared using no template. No structure was recorded by XRD and no pores were observed by TEM. The porosity of such films is expected to be sub-nanometric.[41, 42]

Micropatterning of Films

The second step consists in micro-patterning the as-prepared films. Molecular transport is extremely limited in the 2D-hexagonal structure as the nanopore openings are only present at defects or at each end of the films. To create pore accessibility, a PDMS stamp is pressed on the continuous films, as previously described, thus allowing the

creation of surface defects according to a known pattern. This procedure has to be done immediately after the deposition while the silica network is soft. As the stamp is placed on the silica material, the film regions that are in physical contact with the highest parts of the patterned stamp are constricted. After 30 min at 100 °C to consolidate the framework, the stamp is removed. The pattern leaves strips of silica material 1.5 μm wide and 600 nm high, that approximately corresponds to the thickness of the films. Profiles remain similar regardless pore sizes. The stamp is pressed in a way that the strips run perpendicular to the nanopore orientation. Therefore the nanopores that are inside the strips are exposed and open along the vertical sides of these strips.

The patterned films contain template molecules that are removed by calcination at 500 °C. The silica films conserve its 2D-hexagonal mesostructure, as shown by XRD and TEM. After calcination, the pore diameters were estimated to around 5.5 ± 1.0 nm and 2.5 ± 0.5 nm for F127 and CTAB, respectively. For the remainder of this chapter, the resulting mesoporous patterned films will be referred to as large pore films, small pore films and micropore films, using F127, CTAB, and no template, respectively.

Our method has been suggested as an alternative to usual printing techniques, that are soft lithography[43-45] and reactive wet-stamping methods (r-WETS).[46, 47] Our procedure is a one-step technique based on a mechanical compression that does not require surface preparation, layer deposition and/or use of reactives, which makes it easy-to-use and cheap. In addition, it should be noted that reactive wet-stamping techniques could not be used for our films. Attempts were made to etch a pattern into films by having them come into a contact with a micro-patterned hydrogel stamp. The stamp was soaked in a buffered

hydrofluoric acid (BHF) solution, as described by Klichko *et al.*[29] Although this method was successful for CTAB-templated films (pore size 2.5 nm), it systematically failed for F127-templated films (pore size 5.5 nm) as BHF drastically infiltrates the porosity and quickly diffuses into the silica framework to destroy the film.

2.3.2 Nanopore Alignment and Accessibility

To explore the ability for external molecules to enter the porosity of the films, fluorescence polarization of a long-chain linear polymer (MEH-PPV) incorporated into the pores of a patterned film were investigated. In addition, a film infiltrated with a small dye molecule, Rhodamine B, and was characterized by confocal microscopy.

Polymer Incorporation and Spectroscopic Characterization

A fluorescent polymer MEH-PPV was infiltrated into the pores of a large pore film. It is known that the conformation of the polymer chains controls the polymer photophysics.[48] Emission polarization, as optical properties, can be affected by the orientation, the degree of aggregation and the surrounding environment of the polymer chains.[49-51] In an homogeneous solution, polymer strands are randomly oriented and free to move, which leads to a non-polarized fluorescence. On the other hand, when polymers are excited with a given polarization of light they show a preferential orientation. Photoluminescence is expected to be stronger in the direction parallel to the excited polarization than at 90° to

the excitation. Inside the pores of a patterned film, the polymer chains are forced to stretch out and be aligned in the direction of the nanopores. This preferential alignment gives rise to polarized fluorescence. The polymer that is not in the pore has random orientation, which gives non-polarized fluorescence.

Fluorescence emission spectrum of infiltrated materials are shown in Figure 2.4a. Both the polarization of the emitted light and the peak shifts in the polymer emission are examined. As the sample is not washed, three main peaks are observed at 492 nm, 568 nm, and 625 nm. A difference in the parallel and perpendicular intensities is observed and is particularly pronounced for the peak at 492 nm. This peak corresponds to polymer chains aligned preferentially inside the nanopores while the other peaks correspond to polymers at the surface. In fact, the polarization effect is the greatest at 492 nm, which would correspond to the behavior of aligned chains in the direction of the nanopores. In contrast, the emission peaks of the polymer on the outside of the film are only slightly polarized, probably caused by the tail of the 492 nm polarized band. In addition, a polymer chain that is surrounded only by silica or silane that is confined in a nanopore is expected to result in a blue shift in emission, compared to polymer chains surrounded by other polymers.[51, 52] This effect has been observed by Klichko and coworkers for mesoporous CTAB-templated silica films infiltrated by MEH-PPV.[29] Finally, as the sample is extensively washed (Figure 2.4a), only the peak at 492 nm remains. That is supplementary evidence that the peak at 492 nm corresponds to polymers that infiltrated the nanopores. Once the sample is washed, aggregated polymer chains are removed from the surface while polymer strands are kept inside the pores.

Fluorescence Microscopy

A patterned mesoporous large pore film was derivatized with poly(NIPAAm-co-AAm), as described below, and loaded with Rhodamine B. The polymer chains blocked the pore openings, sealing in the dye inside the pores, and the excess dye on the surface was washed off. A fluorescence confocal microscopy revealed the presence of the dye inside the material (Figure 2.4b). The patterned film surface appears as fluorescent parallel lines, while regions where the silica was constricted are dark. This is evidence that molecules of Rhodamine B size are able to enter the pores and to be retained inside by the polymer.

2.3.3 Thermoresponsive Poly(NIPAAm-co-AAm) modified Films

Synthesis and Characterization of poly(NIPAAm-co-AAm)

The synthesis of poly(NIPAAm-co-AAm) is depicted in Figure 2.5.[32] 2-Bromo-2-methylpropionic acid reacts with N-isopropyl acrylamide and acrylamide in the presence of copper bromide to form long polymer chains (M_n = 102,000 g/mol, M_n/M_w = 1.42 through atom transfer radical polymerization. The LCST of the polymer was determined to be 41 °C by plotting the percent transmittance vs. temperature at 450 nm (Figure 2.6).

Attachment of poly(NIPAAm-co-AAm) onto Films

The patterned silica films are submerged in dry toluene upon which APTES is added to the solution and then refluxed for 24 hrs. under nitrogen (Figure 2.7). Afterwards, the films are thoroughly rinsed and then left to dry. Poly(NIPAAm-co-AAm) is dissolved in water and immediately after adding EDAC the amine modified films are carefully placed in the solution. After 24 hrs. the long polymer chains are grafted onto the stamped silica surface. Figure 2.8 is an AFM image of the film before and after the polymer grafting. The channels of the pattern are well defined before the polymer is grafted. Afterwards, the polymer fills the insides of the channels as well as the top surface of the film.

2.3.4 Release Studies

As stated in the introduction, Figure 2.1 is a schematic of how the polymer coated film works. Below 41 °C, the polymer strands stand erect due to hydrophilisity and block the pores. To load the film, the film is placed in a solution containing the desired cargo molecules and heated above 41 °C. The polymer changes from hydrophilic to hydrophobic, collapsing the polymer and exposing the pore openings. The solution is then cooled to room temperature allowing the polymer to once again block the pores. The film is the washed to remove excess dye. When the film is heated above 41 °C a second time, the cargo molecules are allowed to exit the unblocked pores, again due to the polymer changing to a hydrophobic state.

The polymer coated large, small, and microporous films were submerged in 2 mM propidium iodide solution. The solution was heated to 50 °C and was left stirring for 24 hrs. The films were then thoroughly washed.

Release of Polymer Coated Films

The operation of the thermoresponsive films was monitored in an aqueous solution using luminescence spectroscopy. Figure 2.9 and Figure 2.10 depict the release profiles of propidium iodide for polymer coated films and non-polymer coated films, respectively. The emission intensity was monitored for 1 hr. at room temperature before the solution was heated to 45°C. The decrease in the baselines indicates the degradation of propidium iodide that was absorbed onto the silica film due to the 377 nm probe beam.

In order to confirm that the large pore film can contain more cargo than the small pore film release studies were conducted using six different films; large pore, small pore, and microporous films with and without polymer. Figure 2.9 shows the release profiles for the films with polymer. The large pore film's intensity increases the most and the microporous film's intensity increases the least. The small pore film released only half as much propidium iodide than the large pore film. This indicates that more cargo can be contained due to the larger sized pores, which was expected. The small release on the microporous film is caused by dye trapped solely by the polymer, which is roughly 15% of the amount the large pore can release. Therefore, 85% of dye is being released from the

pores of the large pore film. The data implies that the larger the pore the more dye or cargo can potentially be trapped and released.

Looking at Figure 2.10, the same trend can be seen. The large pore non-polymer coated film has a slightly higher intensity compared to the small pored non-polymer coated film, and the microporous non-polymer coated film has a negligible increase. The reason there is an increase in intensity is due to some dye being trapped inside the pores even after several washings. Heat causes the dye that is trapped or absorbed onto the surface to leave the films and thus the increase is observed.

Comparing the two figures, the data shows that, in all three cases, the films with the polymer coating traps and releases more dye than the films without polymer coating. For the large and small pore film, this suggests that the polymer is blocking the pore opening and is successfully trapping the dye inside. The release from the polymer coated microporous film suggests that the polymer is trapping some dye onto the surface.

Reusability of the Films

To test the reusability of the films, a large pored film was used. The film was loaded with propidium iodide using the same method as before. After the first release experiment, the film was reloaded with propidium iodide and a second release experiment was conducted. Figure 2.11 shows the results of the experiment. The reloaded film does not hold as much dye a fresh film, as seen from the data, but the sharp increase in intensity indicates that the polymer on the film is still able to trap and release dye. The data shows

that the films can be reused, however it has been observed that after the second release the film degrades and you can no longer see the pattern on the film.

Temperature Control Release

To ensure that the polymer keeps the dye trapped in the pores until the temperature is past 41 °C, temperature studies were done. Figure 2.12 shows the temperature release dependence on a large pore film. The initial temperature was set at 35 °C and then ramped to 45 °C and then 55 °C. No increase in intensity was observed at 35 °C. This implies that the polymer is still blocking the pore openings. At 45 °C the intensity starts to increase and at 55 °C the intensity increases only slightly faster. The data shows that the release is caused by the collapse of the polymer chains once the LCST is reached.

2.4 Conclusion

Films with pore sizes of ~2 nm and ~5 nm aligned in the pulling direction were synthesized. The thickness of the films were determined to be 600 nm and the patterned features were 1.5 μm wide strips oriented perpendicular to the direction of the nanopores which are separated from each other by 1.5 μm gaps. The patterned features were obtained using a PDMS stamp without the need of acid. Loading the films with a fluorescent polymer and measuring the emission and polarization of the polymer inside the pores confirmed the nanopores accessibility and orientation.

Poly(NIPAAm-co-AAm) was grafted onto the surface of the films. The films with the polymer grafted on the surface were able to entrap more dye than the films with no polymer. The large pored film contained more dye than both the smaller pored and the no pored films. Release of the dye was only observed when the temperature reached the polymers LCST. While less dye was released, the films proved that when the pattern stays intact the film can be re-loaded with dye and a second release can be obtained.

These smart materials utilize the micropatterned structure to successfully load and release cargo using a thermal sensitive polymer. Since the polymer operates slightly above body temperature, the films could be useful in biomedical application.

2.5 Figures and Tables

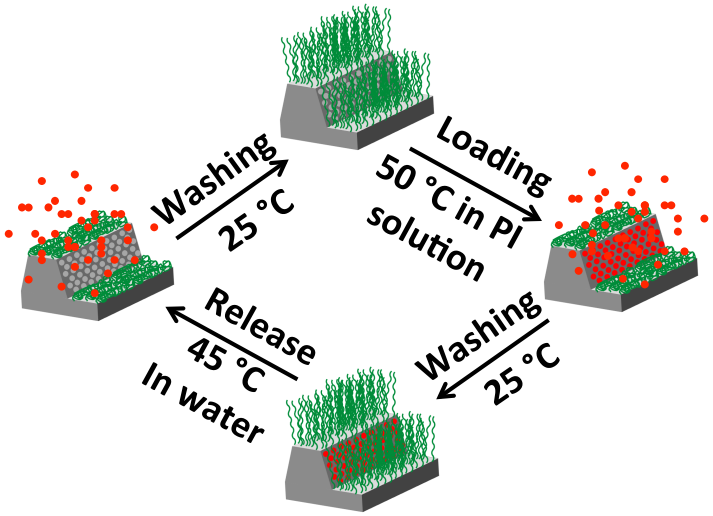

Figure 2.1 The operation of the temperature-activated opening of the nanopores. A side view of one of the stamped channels is illustrated. When heated past the polymer's LCST, the polymer chains collapse allowing cargo molecules to enter the pores. Washing with cool water below the LCST causes the chains to go back to their extended conformation, blocking the pore openings. Heating the water again causes the polymer to shrink, releasing the cargo. This process can be repeated.

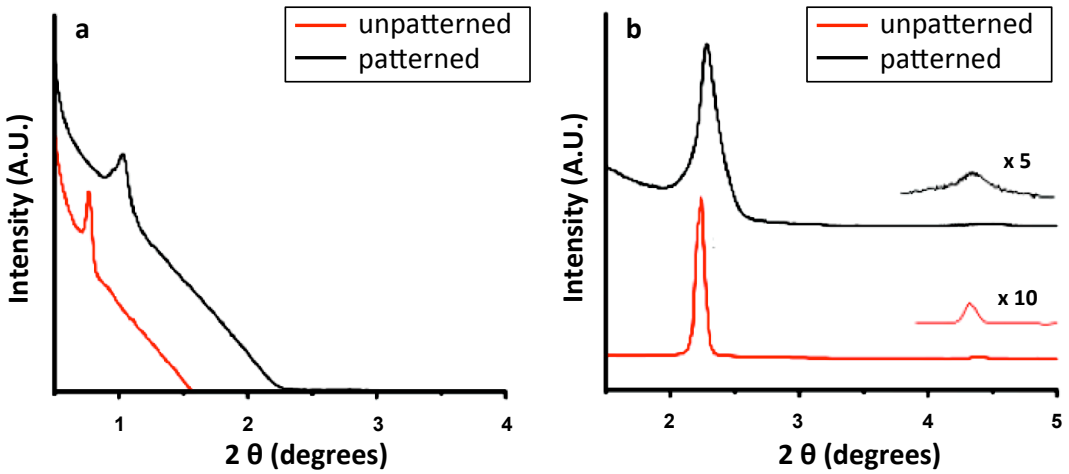

Figure 2.2 X-ray diffraction spectra of mesostructured (red line) and patterned mesoporous (black line) silica films prepared using (a) Pluronic F127 and (b) CTAB.

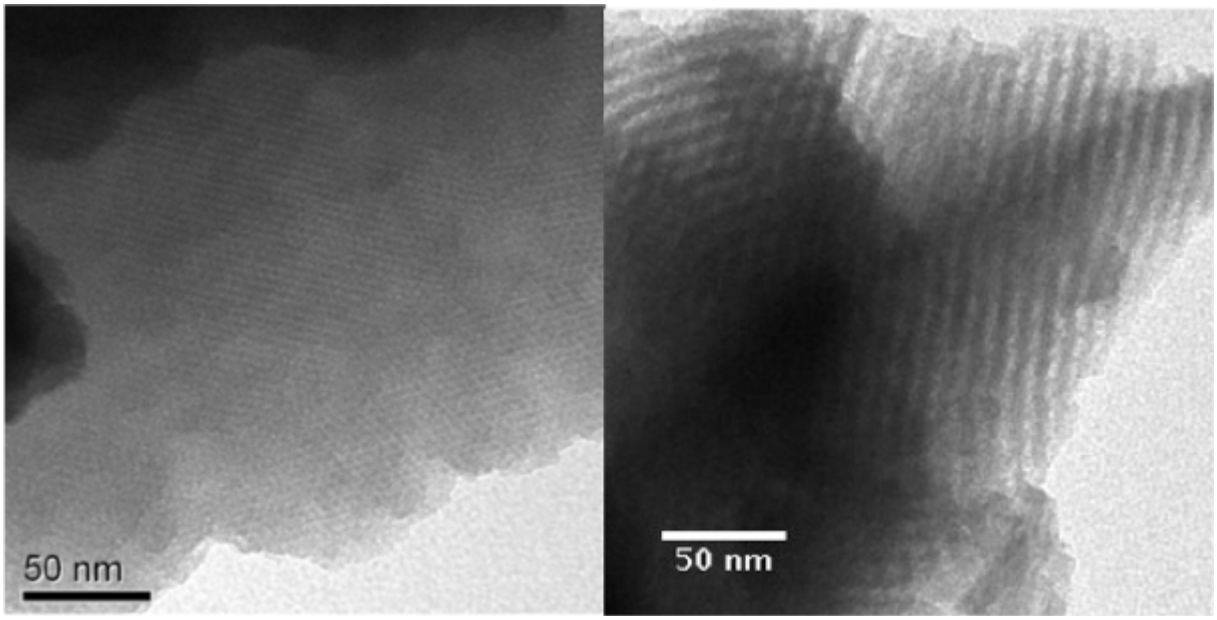

Figure 2.3 TEM images of mesostructured silica films prepared using CTAB (left) and Pluronic F127 (right).

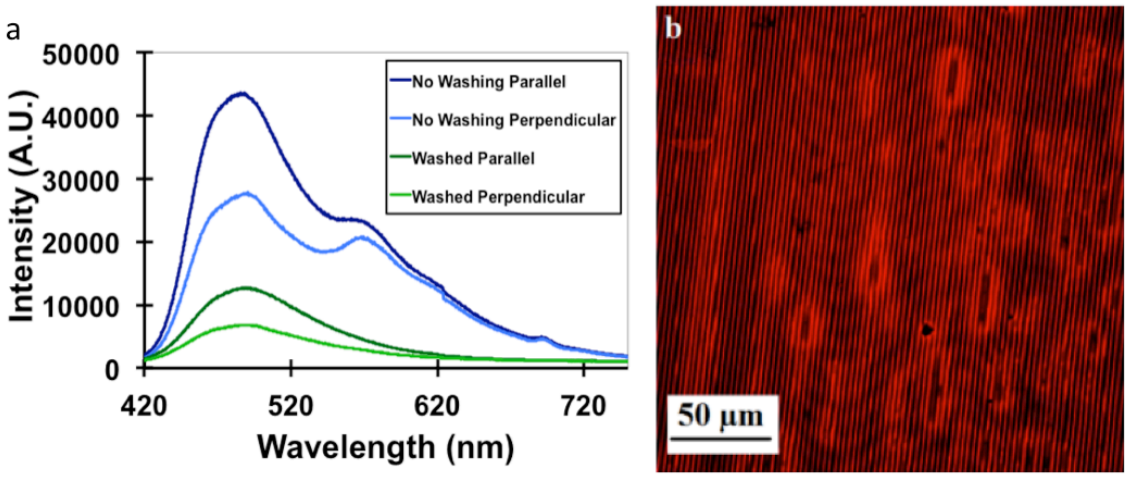

Figure 2.4 (a) Fluorescence emission spectrum of MEH-PPV incorporated into a patterned large pore film. As the sample is not washed (blue lines), multiple peaks are observed which correspond to various environments. As the sample is extensively washed (black lines), the peak at 492 nm corresponds to polymer chains aligned preferentially inside the nanopores. The emission intensity is greater in the plane parallel to the orientation of the pores (solid) compared to perpendicular (dashed). (b) Fluorescence confocal microscopy images of Rhodamine B dye doped patterned F127-templated mesoporous silica films after derivatization of poly(NIPAAm-co-AAm) polymer using (a) Pluronic F127 and (b) CTAB.

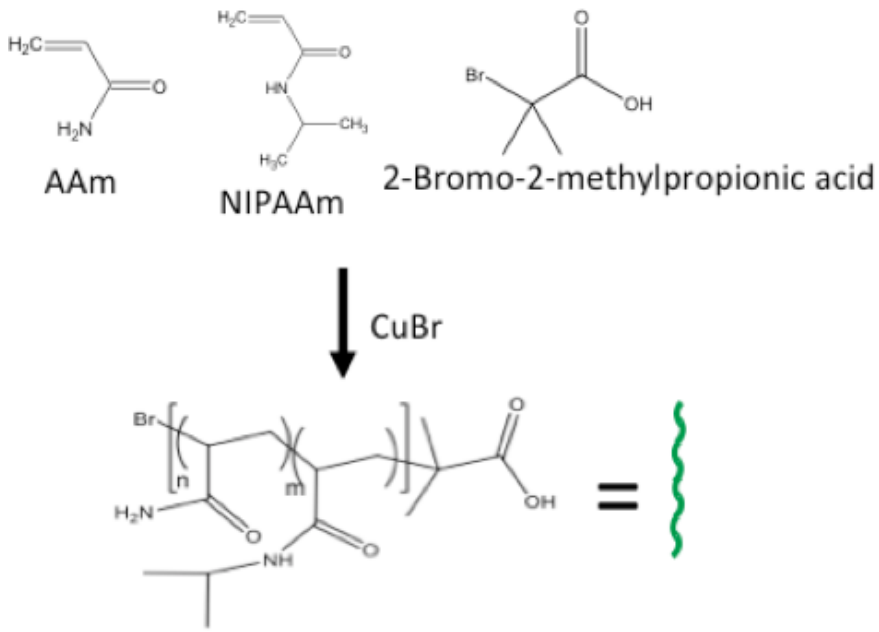

Figure 2.5 Atom-transfer radical polymerization of NIPAAm and AAm monomers (at a molar ratio of *m=7n) as initiated by* 2-bromo-2-methylpropionic acid in the presence of a Cu(I) catalyst.

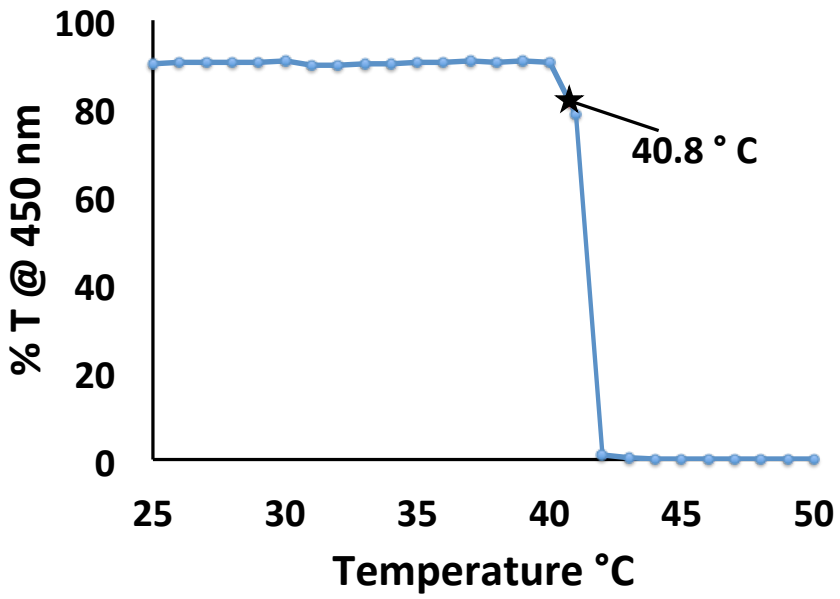

Figure 2.6 Percent transmittance vs. temperature at 450 nm.

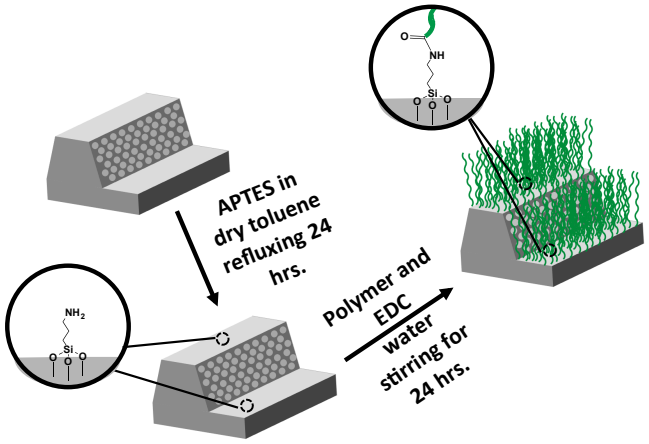

Figure 2.7 Attachment of the thermal polymer onto the stamped silicon film. In dry toluene, APTES is added to the film refluxing for 24 hours.The polymer can then be attached using EDC in water stirring for 24 hours at room temperature.

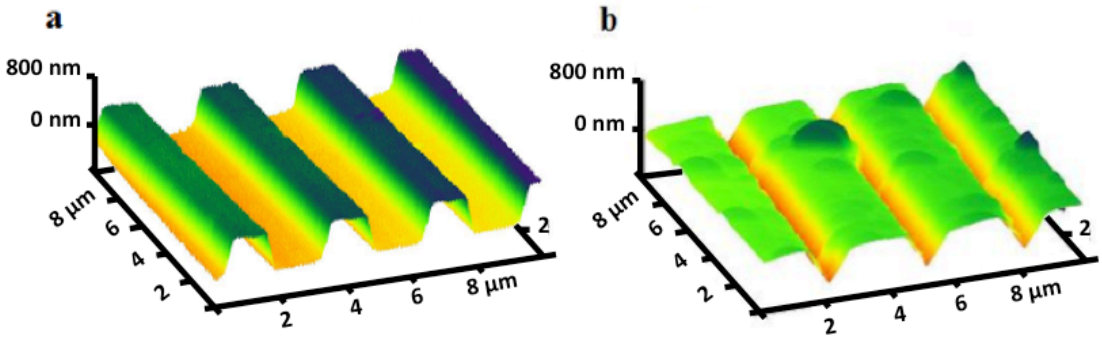

Figure 2.8 AFM images of a patterned mesoporous silica film prepared using Pluronic F127 (a) before and (b) after derivatization with chain poly(NIPAAm-co-AAm) polymer. The scanned ared is 10 x 10 µm. The patterned features are strips 1.5 µm wide, 500 nm high, with 3 µm pitch.

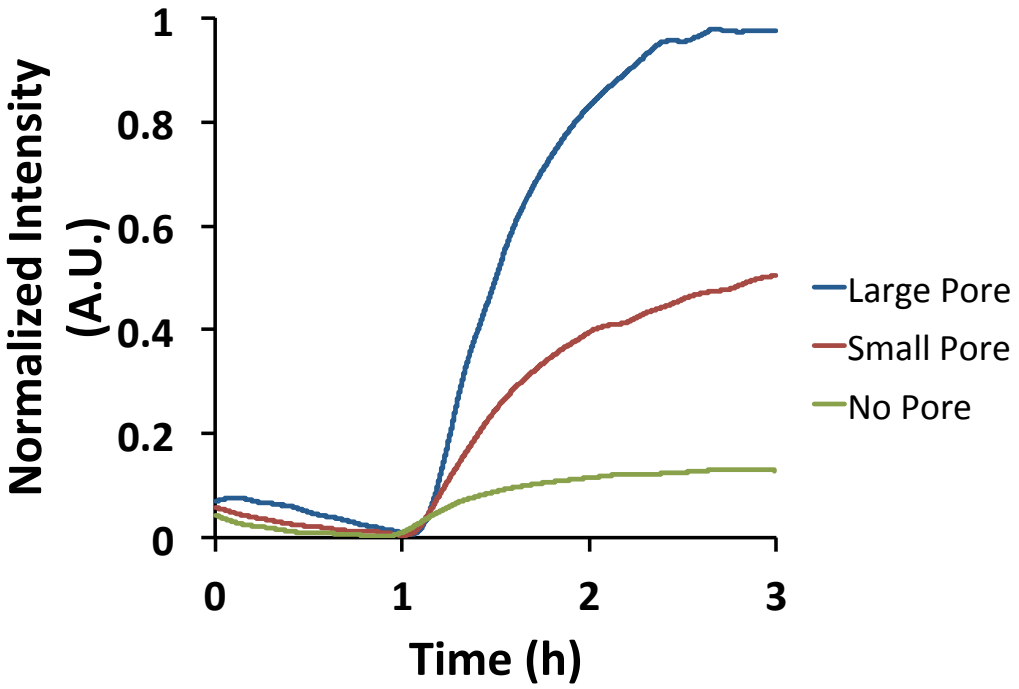

Figure 2.9 Release of propidium iodide from a poly(NIPAAm-co-AAm) modified large/small/no pore films.

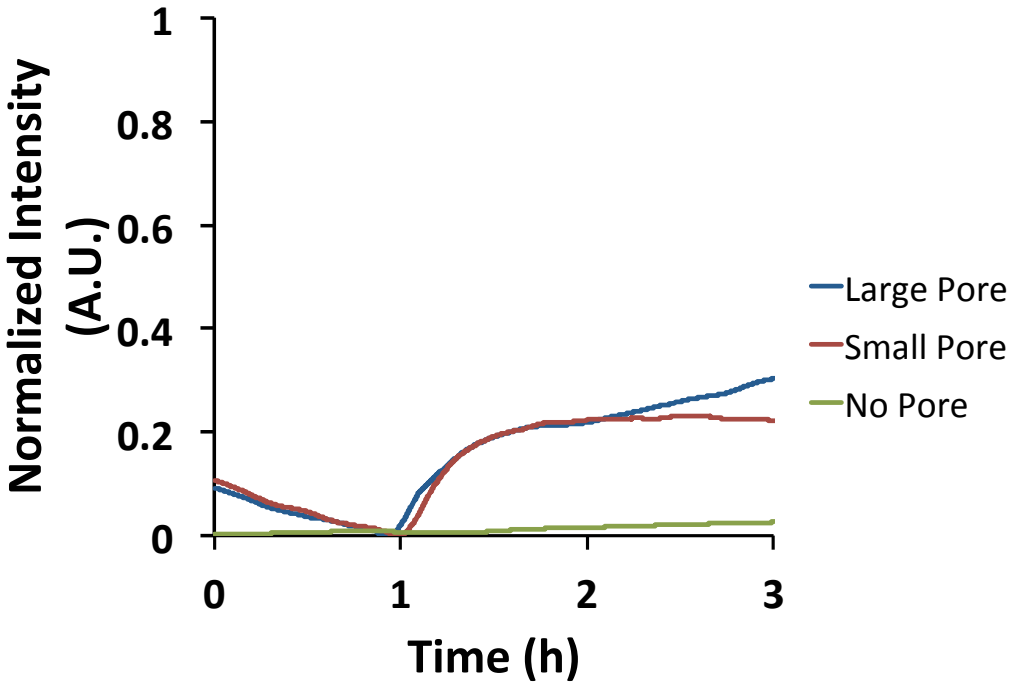

Figure 2.10 Release of unmodified large/small/no pore films.

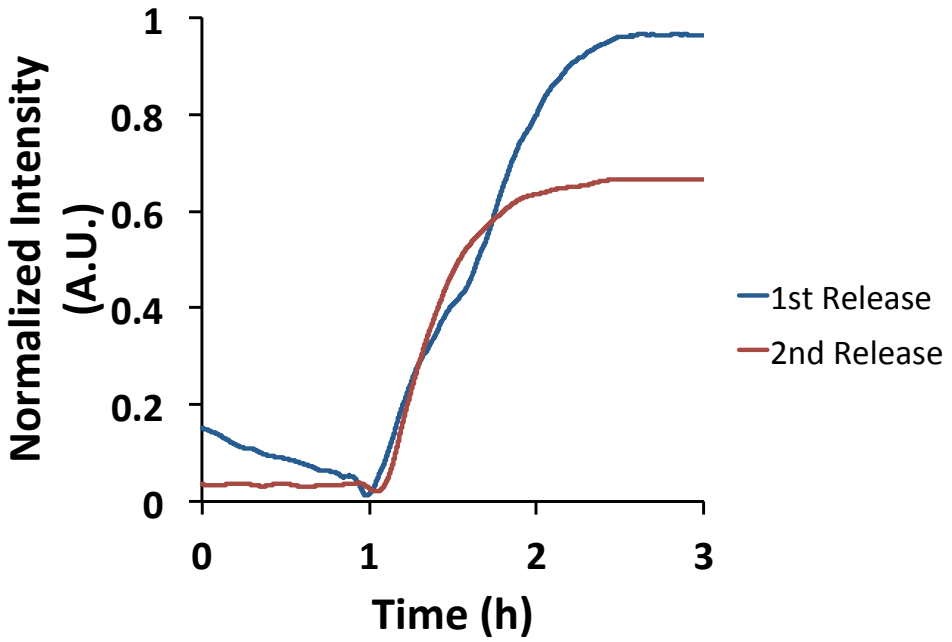

Figure 2.11 Release profile of a large pore film (blue). Release profile of the same large pore film re-loaded with cargo after the first release (red).

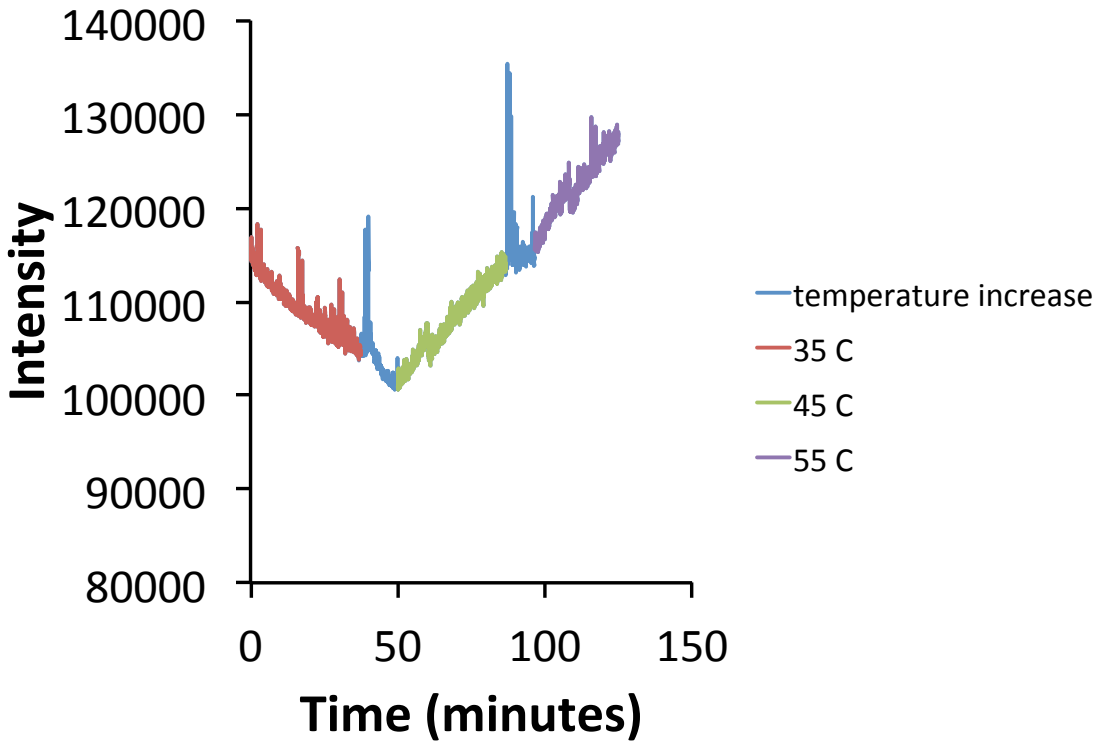

Figure 2.12 Release profile of a large pore film with the baseline set at 35 °C. The temperature was then ramped to 45 °C and then 55 °C. The blue temperature increse sections indicate the period of time when the hot plate was turned on to reach the next temperature level.

2.6 References

1. Beck, J. S.; Vartuli, J. C.; Roth, W. J.; Leonowicz, M. E.; Kresge, C. T.; Schmitt, K. D.; Chu, C. T. W.; Olson, D. H.; Sheppard, E. W., A new family of mesoporous molecular sieves prepared with liquid crystal templates. *Journal of the American Chemical Society* 1992, 114, 10834-10843.

2. Stein, A.; Melde, B. J.; Schroden, R. C., Hybrid inorganic–organic mesoporous silicates—nanoscopic reactors coming of age. *Advanced Materials* 2000, 12, 1403-1419.

3. Liong, M.; Lu, J.; Kovochich, M.; Xia, T.; Ruehm, S. G.; Nel, A. E.; Tamanoi, F.; Zink, J. I., Multifunctional inorganic nanoparticles for imaging, targeting, and drug delivery. *Acs Nano* 2008, 2, 889-896.

4. Cai, Q.; Luo, Z.-S.; Pang, W.-Q.; Fan, Y.-W.; Chen, X.-H.; Cui, F.-Z., Dilute solution routes to various controllable morphologies of MCM-41 silica with a basic medium. *Chemistry of materials* 2001, 13, 258-263.

5. Huh, S.; Wiench, J. W.; Yoo, J.-C.; Pruski, M.; Lin, V. S. Y., Organic functionalization and morphology control of mesoporous silicas via a co-condensation synthesis method. *Chemistry of materials* 2003, 15, 4247-4256.

6. Vallet-Regí, M.; Balas, F.; Arcos, D., Mesoporous materials for drug delivery. *Angewandte Chemie International Edition* 2007, 46, 7548-7558.

7. Han, Y. J.; Stucky, G. D.; Butler, A., Mesoporous silicate sequestration and release of proteins. *Journal of the American Chemical Society* 1999, 121, 9897-9898.

8. Rác, B.; Molnár, Á.; Forgo, P.; Mohai, M.; Bertóti, I., A comparative study of solid sulfonic acid catalysts based on various ordered mesoporous silica materials. *Journal of Molecular Catalysis A: Chemical* 2006, 244, 46-57.

9. Dufaud, V.; Beauchesne, F.; Bonneviot, L., Organometallic chemistry inside the pore walls of mesostructured silica materials. *Angewandte Chemie* 2005, 117, 3541-3543.

10. Van Rhijn, W.; De Vos, D.; Sels, B.; Bossaert, W., Sulfonic acid functionalised ordered mesoporous materials as catalysts for condensation and esterification reactions. *Chemical communications* 1998, 317-318.

11. Lu, J.; Liong, M.; Li, Z.; Zink, J. I.; Tamanoi, F., Biocompatibility, Biodistribution, and Drug-Delivery Efficiency of Mesoporous Silica Nanoparticles for Cancer Therapy in Animals. *Small* 2010, 6, 1794-1805.

12. Lu, J.; Liong, M.; Zink, J. I.; Tamanoi, F., Mesoporous silica nanoparticles as a delivery system for hydrophobic anticancer drugs. *Small* 2007, 3, 1341-1346.

13. Feng, X.; Fryxell, G. E.; Wang, L. Q.; Kim, A. Y.; Liu, J.; Kemner, K. M., Functionalized monolayers on ordered mesoporous supports. *Science* 1997, 276, 923-926.

14. Mercier, L.; Pinnavaia, T. J., Access in mesoporous materials: Advantages of a uniform pore structure in the design of a heavy metal ion adsorbent for environmental remediation. *Advanced Materials* 1997, 9, 500-503.

15. Alberius, P. C. A.; Frindell, K. L.; Hayward, R. C.; Kramer, E. J.; Stucky, G. D.; Chmelka, B. F., General Predictive Syntheses of Cubic, Hexagonal, and Lamellar Silica and Titania Mesostructured Thin Films §. *Chemistry of Materials* 2002, 14, 3284-3294.

16. Zhao, D.; Yang, P.; Margolese, D. I.; Stucky, G. D., Synthesis of continuous mesoporous silica thin films with three-dimensional accessible pore structures. *Chemical Communications* 1998, 2499-2500.

17. Zhao, D.; Yang, P.; Melosh, N.; Feng, J.; Chmelka, B. F.; Stucky, G. D., Continuous mesoporous silica films with highly ordered large pore structures. *Advanced Materials* 1998, 10, 1380-1385.

18. Hatton, B. D.; Landskron, K.; Whitnall, W.; Perovic, D. D.; Ozin, G. A., Spin-Coated Periodic Mesoporous Organosilica Thin Films—Towards a New Generation of Low-Dielectric-Constant Materials. *Advanced Functional Materials* 2005, 15, 823-829.

19. Ogawa, M., A simple sol–gel route for the preparation of silica–surfactant mesostructured materials. *Chemical Communications* 1996, 1149-1150.

20. Ogawa, M.; Masukawa, N., Preparation of transparent thin films of lamellar, hexagonal and cubic silica-surfactant mesostructured materials by rapid solvent evaporation methods. *Microporous and mesoporous materials* 2000, 38, 35-41.

21. Brinker, C. J.; Lu, Y.; Sellinger, A.; Fan, H., Evaporation-induced self-assembly: nanostructures made easy. *Advanced Materials* 1999, 11, 579-585.

22. Lu, Y.; Ganguli, R.; Drewien, C. A.; Anderson, M. T.; Brinker, C. J.; Gong, W.; Guo, Y.; Soyez, H.; Dunn, B.; Huang, M. H., Continuous formation of supported cubic and hexagonal mesoporous films by sol–gel dip-coating. *Nature* 1997, 389, 364-368.

23. Richman, E. K.; Brezesinski, T.; Tolbert, S. H., Vertically oriented hexagonal mesoporous films formed through nanometre-scale epitaxy. *Nature materials* 2008, 7, 712-717.

24. Koganti, V. R.; Rankin, S. E., Synthesis of surfactant-templated silica films with orthogonally aligned hexagonal mesophase. *The Journal of Physical Chemistry B* 2005, 109, 3279-3283.

25. Koganti, V. R.; Dunphy, D.; Gowrishankar, V.; McGehee, M. D.; Li, X.; Wang, J.; Rankin, S. E., Generalized coating route to silica and titania films with orthogonally tilted cylindrical nanopore arrays. *Nano letters* 2006, 6, 2567-2570.

26. Freer, E. M.; Krupp, L. E.; Hinsberg, W. D.; Rice, P. M.; Hedrick, J. L.; Cha, J. N.; Miller, R. D.; Kim, H.-C., Oriented mesoporous organosilicate thin films. *Nano letters* 2005, 5, 2014-2018.

27. Shan, F.; Lu, X.; Zhang, Q.; Wu, J.; Wang, Y.; Bian, F.; Lu, Q.; Fei, Z.; Dyson, P. J., A Facile Approach for Controlling the Orientation of One-Dimensional Mesochannels in Mesoporous Titania Films. *Journal of the American Chemical Society* 2012, 134, 20238-20241.

28. Teng, Z.; Zheng, G.; Dou, Y.; Li, W.; Mou, C. Y.; Zhang, X.; Asiri, A. M.; Zhao, D., Highly Ordered Mesoporous Silica Films with Perpendicular Mesochannels by a Simple Stöber-Solution Growth Approach. *Angewandte Chemie International Edition* 2012, 51, 2173-2177.

29. Klichko, Y.; Khashab, N. M.; Yang, Y.-W.; Angelos, S.; Stoddart, J. F.; Zink, J. I., Improving pore exposure in mesoporous silica films for mechanized control of the pores. *Microporous and Mesoporous Materials* 2010, 132, 435-441.

30. de las Heras Alarcón, C.; Pennadam, S.; Alexander, C., Stimuli responsive polymers for biomedical applications. *Chemical Society Reviews* 2005, 34, 276-285.

31. Stuart, M. A. C.; Huck, W. T. S.; Genzer, J.; Müller, M.; Ober, C.; Stamm, M.; Sukhorukov, G. B.; Szleifer, I.; Tsukruk, V. V.; Urban, M., Emerging applications of stimuli-responsive polymer materials. *Nature materials* 2010, 9, 101-113.

32. Yavuz, M. S.; Cheng, Y.; Chen, J.; Cobley, C. M.; Zhang, Q.; Rycenga, M.; Xie, J.; Kim, C.; Song, K. H.; Schwartz, A. G., Gold nanocages covered by smart polymers for controlled release with near-infrared light. *Nature materials* 2009, 8, 935-939.

33. Hoffman, A. S., Stimuli-responsive Polymers: Biomedical Applications and Challenges for Clinical Translation. *Advanced drug delivery reviews* 2012.

34. You, Y.-Z.; Kalebaila, K. K.; Brock, S. L., Temperature-controlled uptake and release in PNIPAM-modified porous silica nanoparticles. *Chemistry of Materials* 2008, 20, 3354-3359.

35. Fu, Q.; Rama Rao, G. V.; Ward, T. L.; Lu, Y.; Lopez, G. P., Thermoresponsive transport through ordered mesoporous silica/PNIPAAm copolymer membranes and microspheres. *Langmuir* 2007, 23, 170-174.

36. Zhang, X.; Yang, P.; Dai, Y.; Ma, P. a.; Li, X.; Cheng, Z.; Hou, Z.; Kang, X.; Li, C.; Lin, J., Multifunctional Up-Converting Nanocomposites with Smart Polymer Brushes Gated Mesopores for Cell Imaging and Thermo/pH Dual-Responsive Drug Controlled Release. *Advanced Functional Materials* 2013.

37. Johansson, E.; Zink, J. I., Nanostructured Silica Thin Films Self-Assembled with Electron Donors and Acceptors to Measure Electron Tunneling. *Journal of the American Chemical Society* 2007, 129, 14437-14443.

38. Miyata, H.; Kuroda, K., Preferred alignment of mesochannels in a mesoporous silica film grown on a silicon (110) surface. *Journal of the American Chemical Society* 1999, 121, 7618-7624.

39. Miyata, H.; Suzuki, T.; Fukuoka, A.; Sawada, T.; Watanabe, M.; Noma, T.; Takada, K.; Mukaide, T.; Kuroda, K., Silica films with a single-crystalline mesoporous structure. *Nature materials* 2004, 3, 651-656.

40. Tolbert, S. H.; Firouzi, A.; Stucky, G. D.; Chmelka, B. F., Magnetic field alignment of ordered silicate-surfactant composites and mesoporous silica. *Science* 1997, 278, 264-268.

41. Brinker, C. J.; Scherer, G. W., *Sol-gel science: the physics and chemistry of sol-gel processing*. Academic Pr: 1990.

42. Bourgeois, A.; Brunet-bruneau, A.; Fisson, S.; Rivory, J.; Matheron, M.; Gacoin, T.; Boilot, J.-p., Adsorption and Desorption Isotherms at Ambient Temperature Obtained by Ellipsometric Porosimetry to Probe Micropores in Ordered Mesoporous Silica Films. *Adsorption* 2005, 11, 195-199.

43. Xia, Y.; Whitesides, G. M., Soft Lithography. 1998, 37, 24.

44. Quake, S. R.; Scherer, A., From micro-to nanofabrication with soft materials. *Science* 2000, 290, 1536-1540.

45. Rogers, J. A.; Nuzzo, R. G., Recent progress in soft lithography. *Materials today* 2005, 8, 50-56.

46. Campbell, C. J.; Smoukov, S. K.; Bishop, K. J. M.; Grzybowski, B. A., Reactive surface micropatterning by wet stamping. *Langmuir* 2005, 21, 2637-2640.

47. Smoukov, S. K.; Bishop, K. J. M.; Klajn, R.; Campbell, C. J.; Grzybowski, B. A., Cutting into solids with micropatterned gels. *Advanced Materials* 2005, 17, 1361-1365.

48. Schwartz, B. J., Conjugated polymers as molecular materials: How chain conformation and film morphology influence energy transfer and interchain interactions. *Annual review of physical chemistry* 2003, 54, 141-172.

49. Lin, H.-N.; Lin, H.-L.; Wang, S.-S.; Yu, L.-S.; Perng, G.-Y.; Chen, S.-A.; Chen, S.-H., Nanoscale charge transport in an electroluminescent polymer investigated by conducting atomic force microscopy. *Applied physics letters* 2002, 81, 2572-2574.

50. Schaller, R. D.; Lee, L. F.; Johnson, J. C.; Haber, L. H.; Saykally, R. J.; Vieceli, J.; Benjamin, I.; Nguyen, T.-Q.; Schwartz, B. J., The nature of interchain excitations in conjugated polymers: Spatially-varying interfacial solvatochromism of annealed MEH-PPV films studied by near-field scanning optical microscopy (NSOM). *The Journal of Physical Chemistry B* 2002, 106, 9496-9506.

51. Cadby, A. J.; Tolbert, S. H., Controlling optical properties and interchain interactions in semiconducting polymers by encapsulation in periodic nanoporous silicas with different pore sizes. *The Journal of Physical Chemistry B* 2005, 109, 17879-17886.

52. Greenfield, S. R.; Svec, W. A.; Gosztola, D.; Wasielewski, M. R., Multistep photochemical charge separation in rod-like molecules based on aromatic imides and diimides. *Journal of the American Chemical Society* 1996, 118, 6767-6777.

Chapter 3

Light Activated MCM-41 Silica Nanoparticles Using an Azobenene Based Polymer

3.1 Introduction

Nanoscale devices, in particular mechanized silica nanoparticles, have become prevalent in the field of medicine.[1-6] All mechanized silica nanoparticles have three main components. They all have a solid support, a payload of cargo molecules, and some form of external machinery. Mesoporous silica nanoparticles, in particular MCM-41 are chosen[7] as the solid support. These particles are rigid, robust, chemically inert, and relatively easy to make.[8-10] It has been proven that by functionalizing the surface of silica nanoparticles with various machines that can block the pore openings,[5, 11-14] cargo molecules, such as chemotherapy drugs, can be contained within. Under various stimuli, such as pH,[12, 15-18] redox potentials,[19-21] and even enzymes,[22-24] the machine activates allowing the controlled release of the cargo molecules in both aqueous and organic solutions. Since drug delivery is one of the most important applications for these mechanized nanoparticles,[2, 3, 5] having activation occur inside the cell is the most common form of activation. However, there are limitations on the degree of control, which leaves room for undesired activation to occur. Instead of relying on internal biological normalities and abnormalities, a different approach uses a system that responds to an external stimulus. Light as a stimulus offers the possibility of precise spatial localization of the release and also of the timing of the cargo delivery.[6, 25-29]

In this chapter the synthesis of an azobenzene-based polymer that is grafted onto the surface of MCM-41 nanoparticles in order to trap and deliver cargo molecules to cells is described (Figure 3.1). It is well known that azobenzene, like other photochromic molecules, have two molecular states; stable and metastable. These states can be inter-

converted by irradiation using different wavelengths of light. Upon photo-induced isomerization, azobenzene has a reversible conformational change from its stable trans state to its metastable cis state. Thermodynamically the most stable state is the trans state, which is around 50 kJ/mol lower in energy than the cis state.[30-32] When excited with UV light, there is a $\pi \rightarrow \pi^*$ transition which causes the azobenzene molecule to switch to its cis state around the azo bond. Under visible light the system undergoes a $n \rightarrow \pi^*$ transition, reverting the azobenzene back to its trans state.

It is also well known that the trans isomer of azobenzene has a dipole moment of less than 0.5 D and the dipole moment of the cis isomer is around 3.1 D.[33-35] This results in different affinities of the trans and cis isomer of azobenzene to the surface of water.[33, 36, 37] Therefore, in water based systems, when the azobenzene polymer is exposed to visible light, the polymer will shrink around the MCM-41 nanoparticles. This will cause the polymer to block the pore openings and trap cargo inside the nanoparticles. When the azobenzene polymer is exposed to UV light the polymer will expand and thus allow the trapped cargo to diffuse out of the pores. By attaching the azobenzene polymer onto the surface of MCM-41, a light activated delivery system to cells can be achieved.

3.2 Experimental Section

3.2.1 Synthesis of the Light Activated Cargo Delivery System

The synthesis of the azobenzene polymer is adapted from a previously published paper.[38] The first step is to synthesize the azobenzene monomer unit *trans*-4-methacryloyloxyazobenzene. From there, the azobenzene polymer will be made with *trans*-4-methacryloyloxyazobenzene, vinyltrimethoxysilane and methacrylic through free radical polymerization using azobisisobutyronitrile (AIBN) as the radical initiator. MCM-41 nanoparticles will be made using the sol-gel method. The polymer will then be grafted onto the surface of the particles creating the light activated cargo delivery system

Synthesis of trans-4-Methacryloyloxyazobenzene

In order to synthesize the *trans*-4-methacryloyloxyazobenzene, 10 g of 4-hydroxyazobenzene is first dissolved in 120 mL of THF. Then 5.12 g (50.6 mmol) of triethylamine and 5 mg of 2,6-di-tert-butyl-p-cresol to act as an inhibitor were added. The THF solution was purged with nitrogen gas and was allowed to stir for 30 min at room temperature. The solution was then brought below 5 °C using an ice bath. Next, 15 mL of methacryloyl chloride was slowly injected into the solution using a glass syringe. The solution was then allowed to return to room temperature and was left stirring for 48 hrs. The precipitate, triethylammonium chloride, was filtered off and any excess methacryloyl

chloride was hydrolyzed. The remaining solution was diluted four times by adding a mixture of $CHCl_3$ and water in a 3:1 ratio. The organic layer was washed three times with deionized water. The yellow organic layer was then dried on anhydrous Na_2SO_4 and the residual solvent was removed. The yellow solid was then purified using silica column chromatography using chloroform as the solvent. The product was crystalized from n-hexane and was then dried.

Synthesizing the Azobenzene Polymer Through Free Radical Polymerization

To synthesize the azobenzene polymer, 0.9 g of *trans*-4-methacryloyloxyazobenzene, 2.90 mL of methacrylic acid, 0.52 mL of vinyltrimethoxysilane, and 60 mg of AIBN was dissolved in 20 mL of THF. The mixture was degassed under vacuum by freezing the solution in liquid nitrogen. This was repeated three times to ensure the complete removal of air from the flask. The solution was then heated to 65 °C for 72 hrs. The product was then precipitated from methanol and then purified by precipitating it from DCM/methanol mixture.

Synthesizing MCM-41 Nanoparticles

MCM-41 nanoparticles are synthesized using the sol-gel method. First, 250 mg of cetyltrimethylammonium bromide (CTAB) is added to 120 mL of deionized water. Then, 1.12 mL of a 2 M NaOH solution is added. The solution is then brought to 80 °C and allowed

to stir for 30 min. in order for the micelles to form. After which 0.9 mL of tetraethylorthosilicate is added to the solution and the reaction continues for 2 hrs. The particles are then washed with methanol through centrifugation three times. To remove the surfactant, the particles are placed in a solution containing 40 mL of methanol and 2 mL of concentrated HCl. The solution is left refluxing for 12 hrs. at which point the particles are washed three times with methanol and then allowed to dry.

Grafting the Azobenzene Polymer onto MCM-41

To graft the polymer onto the silica surface, 50 mg of MCM-41 nanoparticles were suspended in 3 mL of methanol. 20 mg of the azobenzene polymer were dissolved in 2 mL of methanol and added drop wise to the particle suspension. The solution was left stirring for 24 hrs. The particles were then washed twice with methanol.

Loading with a Fluorescent Cargo

The particles were then loaded with propidium iodide by suspending the particles in 1 mL methanol solution of 2 mM propidium iodide. The particles were left in the solution for two days and then washed thoroughly with water.

3.2.2 Activation of the System in Water

The operation of the system was monitored using fluorescence spectroscopy. A small sample of particles was placed in the corner of a 2 X 1 cm cuvette. 6 mL of water was carefully added in order to not disturb the particles, and the cuvette was placed in front of a CCD. A stirring magnet was carefully placed in the opposite corner and the solution was stirred in order to help with mixing. The emission of propidium iodide was measured as a function of time by using a 448 nm probe beam (15 mW). The emission spectrum was recorded as a function of time at 1 second intervals. The activation of the system was achieved by exposing the particles to a 377 nm laser (15 mW). A release profile was obtained by plotting luminescence intensities of propidium iodide at the emission maximum (650 nm) as a function of time. A control was done following the same set up, but the particles were exposed to a 514 nm laser (40 mW) instead of the 377 nm laser.

3.2.3 Cell Studies

Cell Culture

Human pancreatic cancer cell line, MiaPaca-2, obtained from the American Type Culture Collection were cultured in Dulbecco's modified Eagle's medium (DMEM) supplemented with 10% fetal calf serum (Sigma), 2% L-glutamine, 1% penicillin, and 1% streptomycin stock solutions, incubated at 37 °C under a 5% CO_2 95% air atmosphere. The

media were changed every 3 days, and the cells were passaged by trypsinization before confluence.

Cytotoxicity Assay

Cells were cultured in 96-well plates (3000 cells/well) with fresh DMEM at 37 °C in a 5% CO_2/95% air atmosphere for 24 hrs., then washed with PBS and the medium was changed to a fresh medium along with unloaded particles at the various concentrations. 24 hrs. later, the cells were washed with PBS to remove any particles that were not taken up by the cells and continued incubating in DMEM for an additional 48 hrs. 10% WST-8 solution (cell counting kit-8, Dojindo Molecular Technologies, Inc.) was then added to cells and incubated for another 2 hrs. The absorbance of each well was measured at 450 nm with a plate reader.

Activation of the System Invitro

The cells were incubated for two hours with particles loaded with propidium iodide at a concentration of 40 μg/μL. A 403 nm laser was used at 80 mW and the beam was enlarged to 1 cm in order to expose the entire well. The each well was exposed at 10 min intervals until the total exposure time was 1 hr. To determine if propidium iodide was released, fluorescence microscopy was used.

3.2.4 Characterization

The structure of MCM-41 was investigated by X-ray diffraction (XRD) experiments in Bragg-Brentano geometry (θ-2θ) on a Philips X'Pert Powder Diffractometer operated at 40 kV, 40 mA using CuKα radiation (λ=1.54 Å). To measure the size of the particles and if the polymer attached onto the silica surface, transmission electron microscopy (TEM) was used. The particles were dispersed in ethanol and then deposited and dried on a carbon Cu grid. Micrographs were recorded on a JEM1200-EX (JEOL) electron microscope operating at 50 kV. Infrared (FTIR) measurements of the particles were acquired on a Jasco Model 420 spectrometer after the samples were dried at room temperature. A Perkin Elmer Diamond Thermogravimmetric/Differential Thermal Analyzer (TG/DTA) was used to calculate the how much of the polymer condensed around the particles.

The average molecular weight (Mn) and polydispersity index (PDI) of the polymer was measured by Gel Permeation Chromatograph (GPC) using a Waters 515 Differential Refactometer with Waters 410 HPLC pump and two styrage HR 5E columns in THF (0.1 mg/L) as an eluent at 42 °C, calibrated with polystyrene standards. H^1 NMR of the azobenzene monomer and polymer were taken on a Bruker ARX-400. UV-vis spectrum of the polymer was taken on a Cary 5000 UV-vis-NIP spectrophotometer.

The time resolved controlled released profiles were obtained using fluorescence spectroscopy monitored with an Acton SpectraPro 2300i CCD spectrophotometer and detection and excitation was carried out using a CUBE 445 and a CUBE 375 (Coherent Inc., Santa Clara, CA, USA). A 475 nm filter was placed in front of the polarizer to block stray

laser light. For the control experiment the probe beam used was a 514 nm line of a Coherent I306C argon ion laser (40 mW). For the cell studies, a CUBE 405 set at 80 mW with the beam 1 cm in diameter (Coherent Inc., Santa Clara, CA, USA) was used to excite the particles in the well in order to release the propidium iodide. A fluorescence microscope was used to determine if any propidium iodide stained the nuclei.

3.3 Results and Discussion

3.3.1 An Azobenzene Polymer on MCM-41

The Azobenzene Polymer

In order to create the azobenzene polymer, the first step is to synthesize *trans*-4-methacryloyloxyazobenzene. 4-hydroxyazobenzene, triethylamine, 2,6-di-tert-butyl-p-cresol were dissolved in THF. The solution was purged with nitrogen gas and was allowed to stir for 30 min at room temperature. The solution was then brought below 5 °C using an ice bath. Then, methacryloyl chloride was slowly injected into the solution using a glass syringe. The solution was then brought back to room temperature and the reaction continued for another 48 hrs. After purification of the product was done as described in the previous section, the *trans*-4-methacryloyloxyazobenzene was dissolved in methanol and a H^1-NMR was taken (Figure 3.2). The peaks confirm that *trans*-4-methacryloyloxyazobenzene was synthesized and purified.

To synthesize the polymer, *trans*-4-methacryloyloxyazobenzene along with methacrylic acid, and vinyltrimethoxysilane in a 1:10:1 ratio were polymerized using AIBN in THF. The mixture was degassed under vacuum by freezing the solution in liquid nitrogen and once the air was completely removed the solution was then heated to 65 °C for 72 hrs. The product was then precipitated from methanol and then purified by precipitating it from DCM/methanol mixture. Figure 3.3 in a H^1-NMR of the polymer dissolved in deuterated chloroform. The tallest peak is the solvent peak and the peaks from 0-2 ppm are indication of C-H bonds. It is difficult to see any aromaticity since the polymer contains very little of the *trans*-4-methacryloyloxyazobenzene. However, when taking a UV-vis of the polymer in methanol (Figure 3.4), the peak at ~325 nm is the $\pi \rightarrow \pi^*$ transition of azobenzene[30, 39] indicating the presence of the azobenzene in the polymer chain. The UV-vis also indicates where the polymer should be excited in order to stimulate the trans→cis transition. Due to the laser lines available, a 377 nm laser was used to excite the polymer in the methanol solution and a UV-vis was taken. As shown in Figure 3.4, there is a decrease in the $\pi \rightarrow \pi^*$ transition peak and an increase in the $n \rightarrow \pi^*$ transition peak indicating that the azobenzene has gone from trans→cis.[30, 39] The Mw of the polymer is 23,266 Da, Mn is 11921 Da, with a polydispersity index of 1.95.

To test if the polymer would become hydrophilic enough so that it would be able to release cargo from the pores of MCM-41, small samples of the polymer were placed in two separate vials of water with a small stir bar. One vial was left in the fume hood, while the other vial was exposed to a 377 nm laser. Both vials were left stirring in the dark for one hour. Figure 3.5 is the image of the vials after 1 hr. On the left is the vial left in the fume

hood and on the right is the vial exposed to the 377 nm laser. Since the polymer does not dissolve in water, the polymer in the vial on the left is precipitated at the bottom of the vial. However, the solution in the vial on the right, which was exposed to the 377 nm laser, is slightly cloud and orange. This indicates that the polymer was able to become hydrophilic enough to slightly dissolve in the water solution. This means that when attached to the MCM-41 nanoparticles the polymer will be able to swell enough to allow cargo to escape the pores.

The Azobenzene Polymer on MCM-41

MCM-41 silica nanoparticles were synthesized using CTAB as the templating agent. CTAB was dissolved in a solution of water and NaOH was added to make the solution basic. The solution was brought to 80 °C and, after the formation of the micelles, TEOS was added to the solution and the reaction was allowed to continue for 2 hrs. The particles were then washed and the surfactant was removed through solvent extraction under acidic conditions. The pore size of the particles was approximately 2 nm based off of XRD (Figure 3.6).

The particles and a sample of the polymer were placed in a solution of methanol and was left stirring for 24 hrs. This allows the silane groups on the polymer to condense onto the surface of MCM-41. Figure 3.7 is an IR of the polymer (blue), unmodified MCM-41 silica nanoparticles (red) and azobenzene polymer modified MCM-41 silica nanoparticles (green). The azobenzene polymer has an aromatic broad peak around 3100 cm^{-1}, which can

be slightly seen in the green trace. Figure 3.8 are TEM images of the unmodified MCM-41 silica nanoparticles (A) and the azobenzene modified MCM-41 silica nanoparticles (B). There are darker areas on the particle after the azobenzene modified MCM-41 silica nanoparticles that were not present in the TEM image before the modification. This implies that the darker regions on the particle is the polymer on the surface of the particle. Based off of these images, these particles are 50-100 nm in diameter. Thermogravimetric analysis (Figure 3.9) was done to see how much polymer condensed onto the surface of MCM-41. The data indicates that approximately 6 % of the sample's weight is that of the polymer. This proves that there is a sufficient amount of polymer that was able to condense onto the surface in order to block the pore openings.

3.3.2 Release Studies in an Aqueous Medium

Light Activation of the Azobenzene Polymer

The operation of the azobenzene polymer on MCM-41 silica nanoparticles was tested by monitoring the fluorescence intensity of propidium iodide using time-resolved fluorescence spectroscopy. After the polymer was attached onto the surface of MCM-41, the particles were loaded with a solution of a fluorescent molecule, propidium iodide, in methanol. A small sample of the particles (~5 mg) was placed in a cuvette and the experiment was set up following the procedure stated previously. The probe beam was 448 nm and the pump beam was 377 nm. Figure 3.10 shows the result of this experiment. A

baseline is taken for about 2 hrs. with only the probe beam turned on. As seen in the figure the baseline is relatively flat. This shows that no dye leaked out of the pores, which indicates that the polymer is effectively able to trap the propidium iodide inside. After the baseline is taken, the 377 nm laser is turned on and is directed on the sample in order to activate the system. There is a steady increase in intensity indicating that the propidium iodide is diffusing out of the pores and polymer layer and getting into the solution. This proves that the system is activated through the use of light.

On/Off Experiment

Since the polymer switches from hydrophobic to hydrophilic it is possible that the system can be turned on and off. This would allow drugs to be released in dosages which can be beneficial in some cases.[40] The experiment was done in the same manner as the previous experiment, only at a certain point the pump beam was turned off. The result of this experiment is shown in Figure 3.11. The baseline in this experiment is slightly increasing over time, which implies that this particular sample was slightly leaky. However, when the 377 nm is turned on, there is a much greater increase in the amount of propidium iodide being released indicating that the leakage is fairly negligible. The 377 nm laser was left on for 2 hrs. and then it was turned off for 2 hrs. The fluorescence intensity stops increasing at this point proving that the system is no longer releasing propidium iodide and that the polymer is once again blocking the pores. Turning the 377 nm back on, the

fluorescence intensity starts to increase again indicating the continued release of propidium iodide. This experiment proves that the system has an on/off capability.

Control Experiment

In order to make sure that the release of the propidium iodide is caused by light excitation and not through localized heating from the laser, a control experiment was conducted. The set up for the experiment is the same as before, except the pump beam used was a 514 nm laser. Since 514 nm is in the visible region, there should not be and trans→cis isomerization which would mean that the polymer should not swell and release propidium iodide. Figure 3.12 shows the result of this experiment. A baseline was taken for about 2 hrs. and then the 514 nm laser was turned on. There is no increase in intensity after the 514 nm laser was turned on indicating that no propidium iodide is being released. This proves that it is not local heating that is causing the dye to be released, but light activation of the azobenzene polymer.

3.3.3 Cell Studies

Toxicity of the Azobenzene Polymer on MCM-41 Silica Nanoparticles

Before release studies can be done *invitro*, the azobenzene modified MCM-41 silica nanoparticles were incubated with pancreatic cancer cells, MiaPaca-2 and tested for

toxicity. Preparation of the cell culture and the cytotoxicity assay was followed as previously described. The absorbance of each well was measured at 450 nm with a plate reader. Since the absorbance is proportional to the number of viable cells in the medium, the viable cell number was determined using a prepared calibration curve. The result of this experiment is shown in Figure 3.13. Comparing the toxicity of unmodified to modified MCM-41 silica nanoparticles at various concentrations, it is clear that the toxicity of the polymer is minimal. This proves that the azobenzene modified MCM-41 silica nanoparticles are non-toxic up to 100 μg/μL.

Activation of the Azobenzene Polymer in Cells

The cells were prepared in the same manner as previously described only with propidium iodide loaded azobenzene modified MCM-41 silica nanoparticles at a concentration of 40 μg/μL. The particles were incubated for 2 hrs. in square 1 cm wells. To activate the system a 403 nm laser was used since the 377 nm laser has been known to kill the cells in the past. The 403 nm laser was set to a power of 80 mW and the beam was expanded to 1 cm in diameter in order to irradiate the entire well. One well was irradiated for 10 mins. and then the beam was moved to another well and was also irradiated for 10 mins. This was done in order to not kill the cells by over heating them. The process was continued until each well had a total irradiation time of 1 hr in order to give the dye enough time to diffuse through the polymer layer.

Figure 3.14 are images of the cells using a fluorescent microscope. The green fluorescence are the cell membranes stained with phosphomolybdic acid and the red fluorescence is the nuclei stained with propidium iodide. The image on the left was not exposed to the 403 nm laser while the one on the right was. There is a small amount red fluorescence shown in image on the left. Since these cells were kept in the dark the azobenzene polymer was not activated. The small amount of red fluorescence could be caused by the particles uptake by the cell, or some slight leakage of the propidium iodide. The nuclei on the right has a lot of red fluorescence indicating that the azobenzene polymer was able to release enough propidium iodide to stain the nuclei of the cell. Greater than 80 % of the cells that were exposed showed similar results. Since propidium iodide is membrane impermeable, this also proves that the particles had to have been up taken by the cells and activated inside of the cell. This is very important if this system were to be used to deliver chemotherapy drugs to cancer cells.

3.4 Conclusions

A light activated system consisting of an azobenzene polymer and MCM-41 silica nanoparticles were synthesized. The azobenzene within the polymer, when exposed to UV light, under goes a trans→cis isomerization. This leads to an overall change in the way the polymer interacts with water, making it go from a hydrophobic state to a hydrophilic state. This change allows the polymer to trap and release cargo molecules from the pores of MCM-41 when it is condensed onto the silica surface. Not only can it release the cargo, but

it possesses an on/off capability. This allows a greater control over the amount of cargo released from the system, enabling controlled dosages to be delivered instead of a continuous delivery. This system is also proven to be a light activated system rather than activation through local heating. Further studies on this system would be to investigate the amount of propidium iodide released upon light excitation to test the overall efficiency of this drug deliver devise.

This light activated system has little to no toxicity to cells, which is very important if this system were to be used for biological applications. It has been demonstrated that these particles also get up taken by the cells and can be activated inside the cells without killing them. This system is a great candidate for a drug delivery devise since it has shown that it has an on command activation of the system, in an aqueous solution and inside of cells, and is non-toxic. The results obtained with human cancer cells are preliminary and further studies still need to be conducted to optimize this drug deliver devise. Such experiments would include increasing the concentration of propidium iodide loaded into the particles and modifying the amount of polymer on the surface.

3.5 Figures and Tables

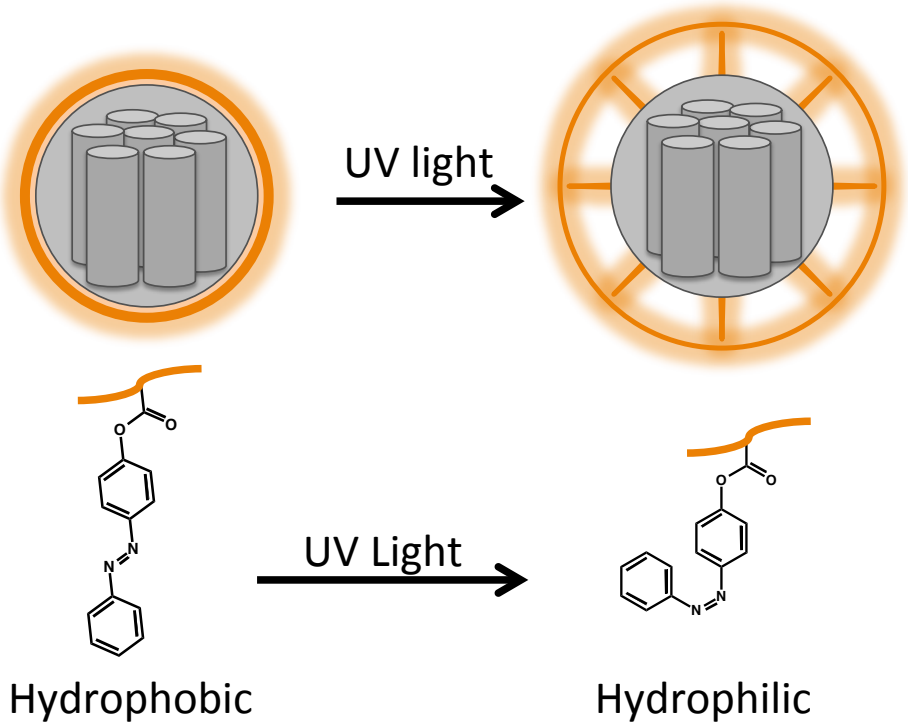

Figure 3.1 The operation of the light activated system. Under visible light, the azobenzene is in its trans state and is hydrophobic. This causes the polymer to shrink around the MCM-41's surface, enabaling it to block the pores. When exposed to UV light, the polymer goes from trans→cis and the polymer becomes hydrphlic. This causes the polymer to swell, allowing cargo to escape the pores.

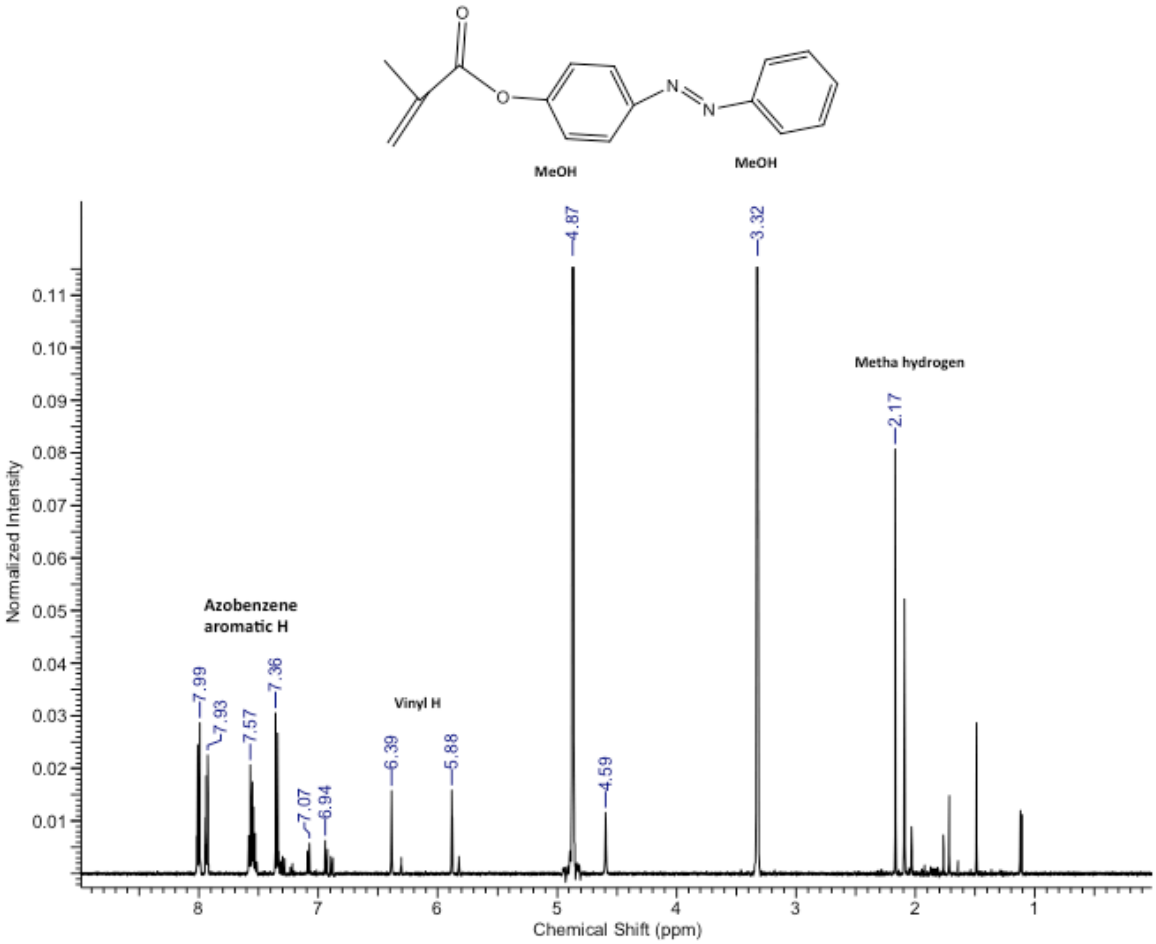

Figure 3.2 H^1-NMR of the *trans*-4-methacryloyloxyazobenzene

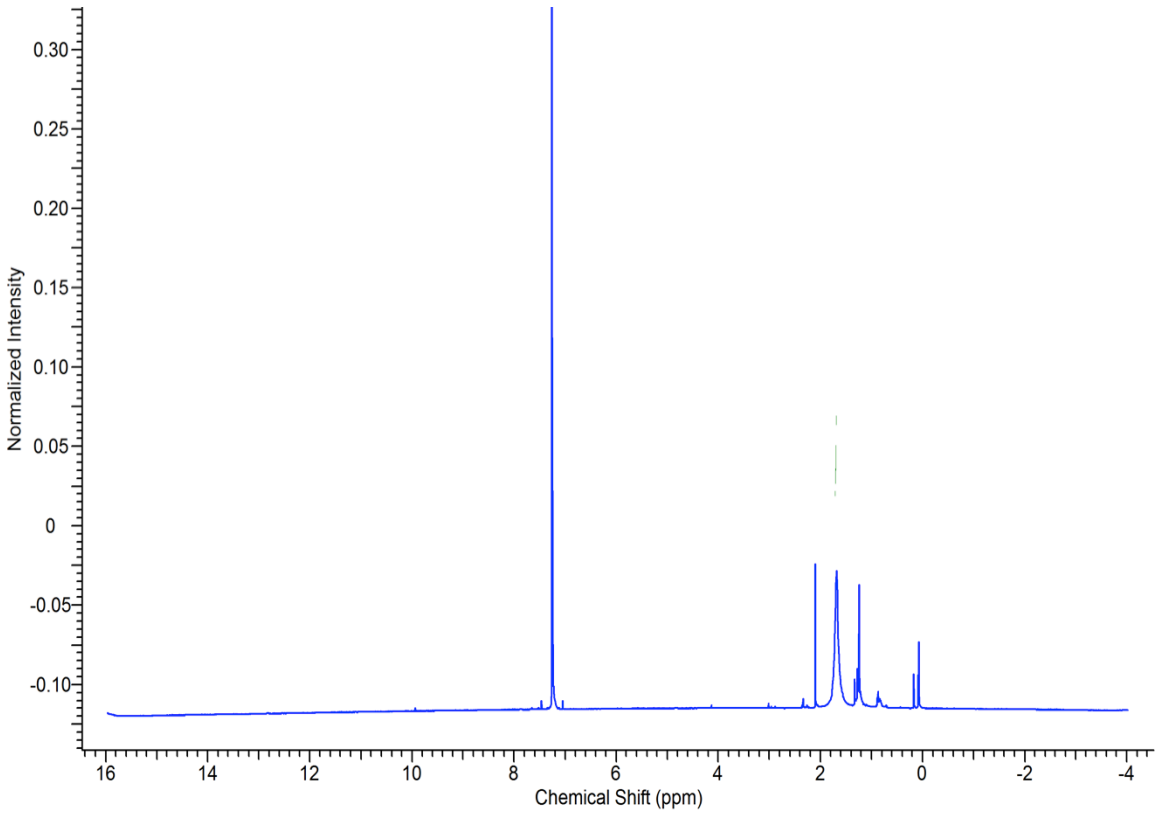

Figure 3.3 H^1-NMR of the azobenzene polymer. There is a small peak at around 10 ppm that could be COOH. Peaks at around 0-2 ppm are C-H. The peak at around 7 is the solvent.

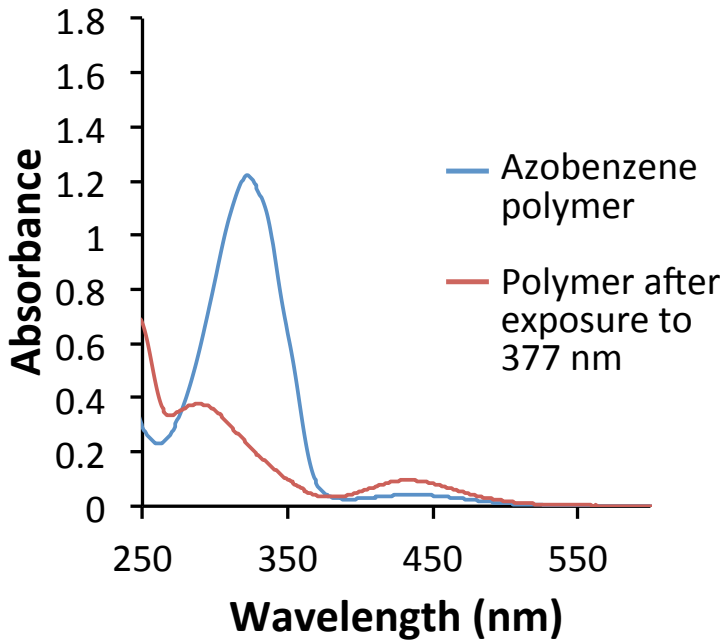

Figure 3.4 UV-vis of the azobenzene polymer in its trans state (blue) and its cis state (red) after being excited with 377 nm.

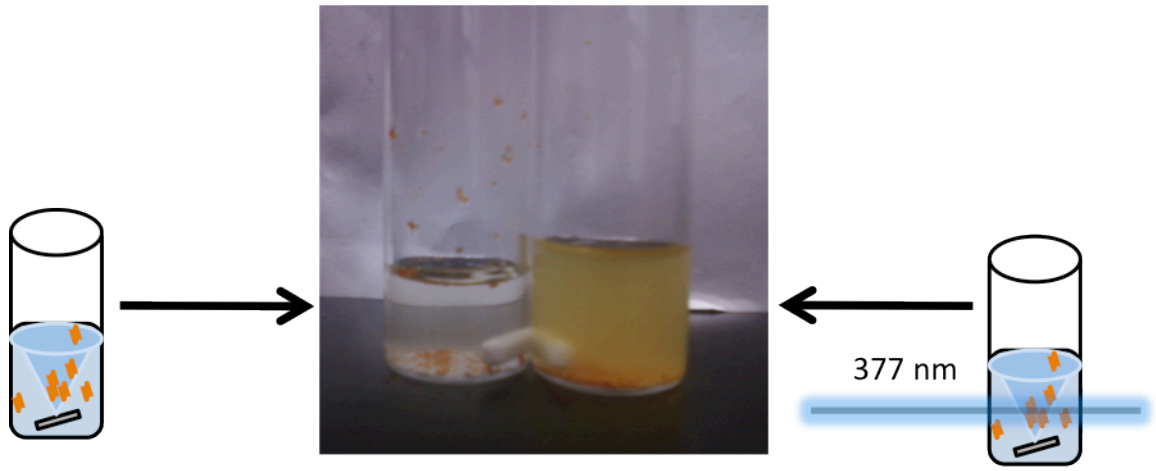

Figure 3.5 Vial on the left was left stirring in the fume hood while the vial on the right was excited with 377 nm for 1 hr.

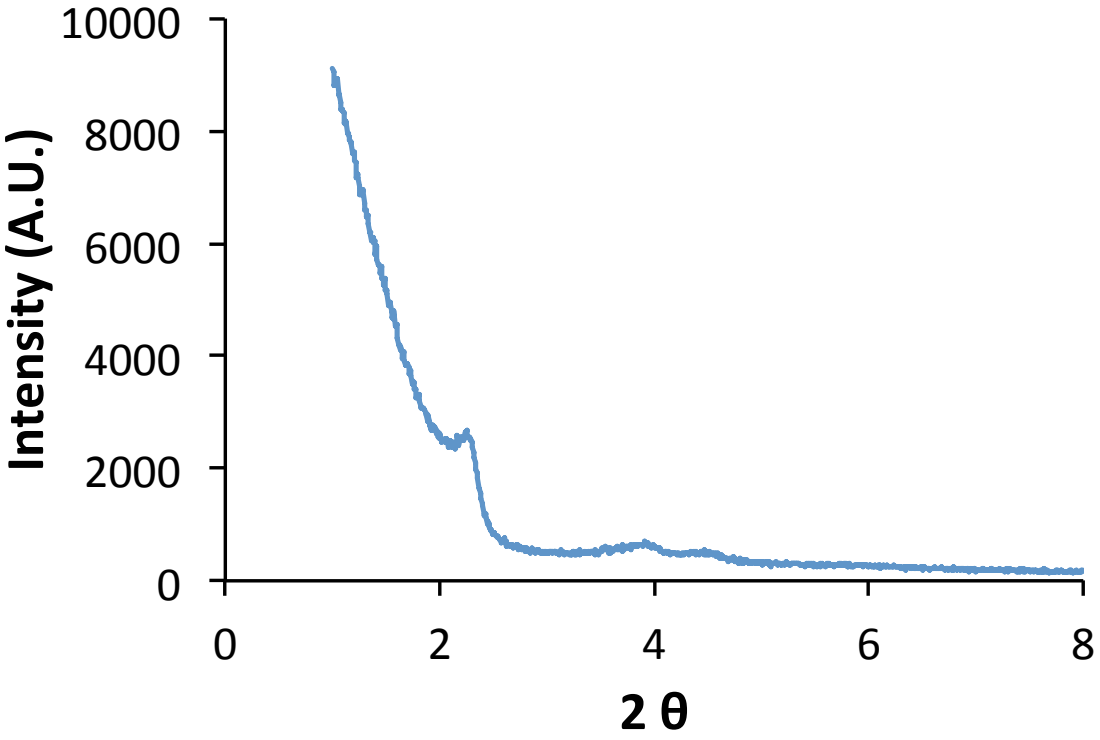

Figure 3.6 XRD of MCM-41 nanoparticles

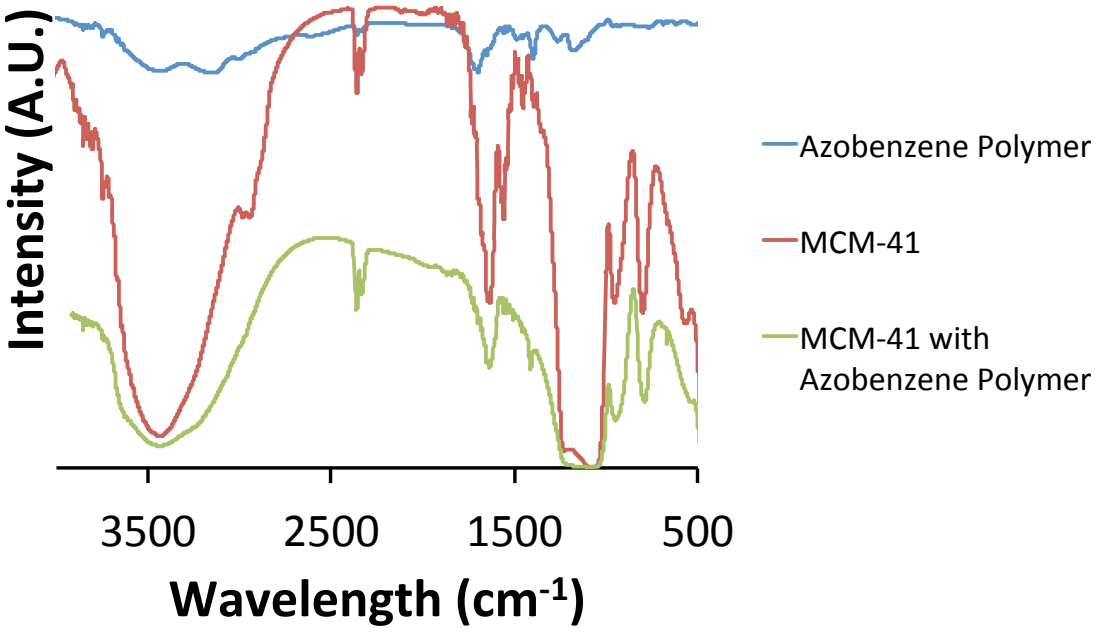

Figure 3.7 IR of the azobenzene polymer (blue), MCM-41 silica nanoparticles (red) and modified MCM-41 with the azobenzene polymer.

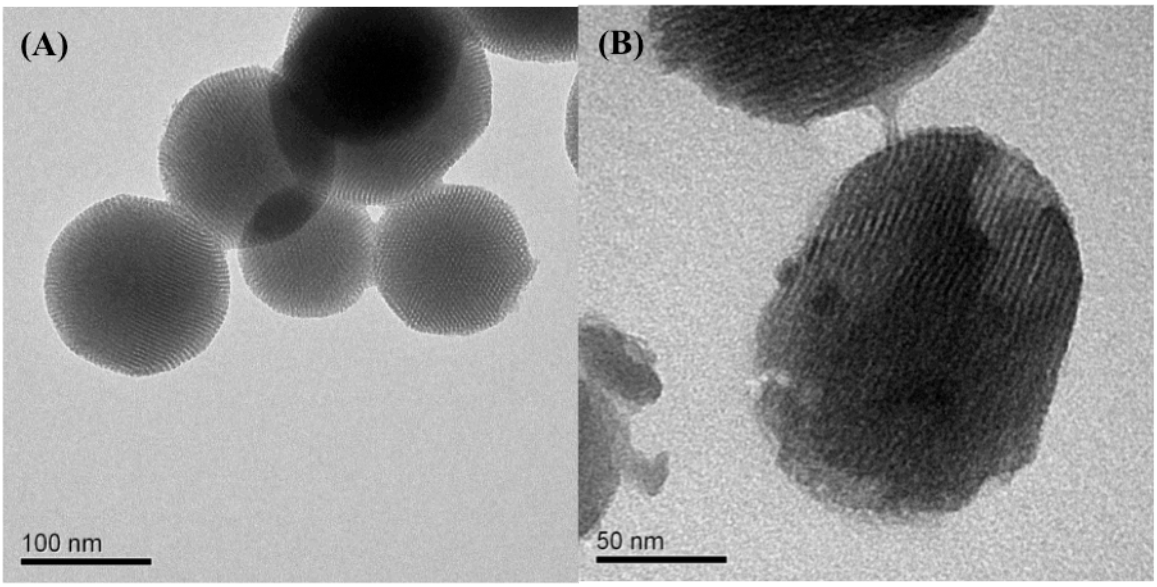

Figure 3.8 TEM images of MCM-41 (A) and modified MCM-41 with the azobenzene polymer (B).

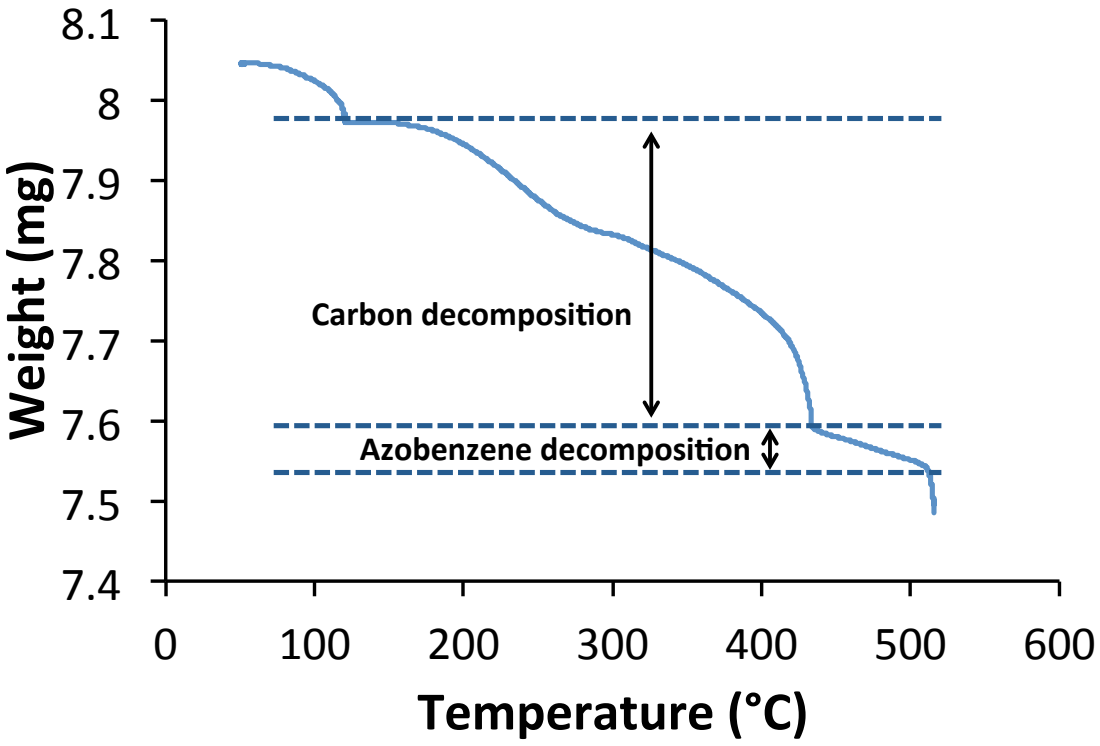

Figure 3.9 TGA of the polymer on MCM-41 silica nanoparticles.

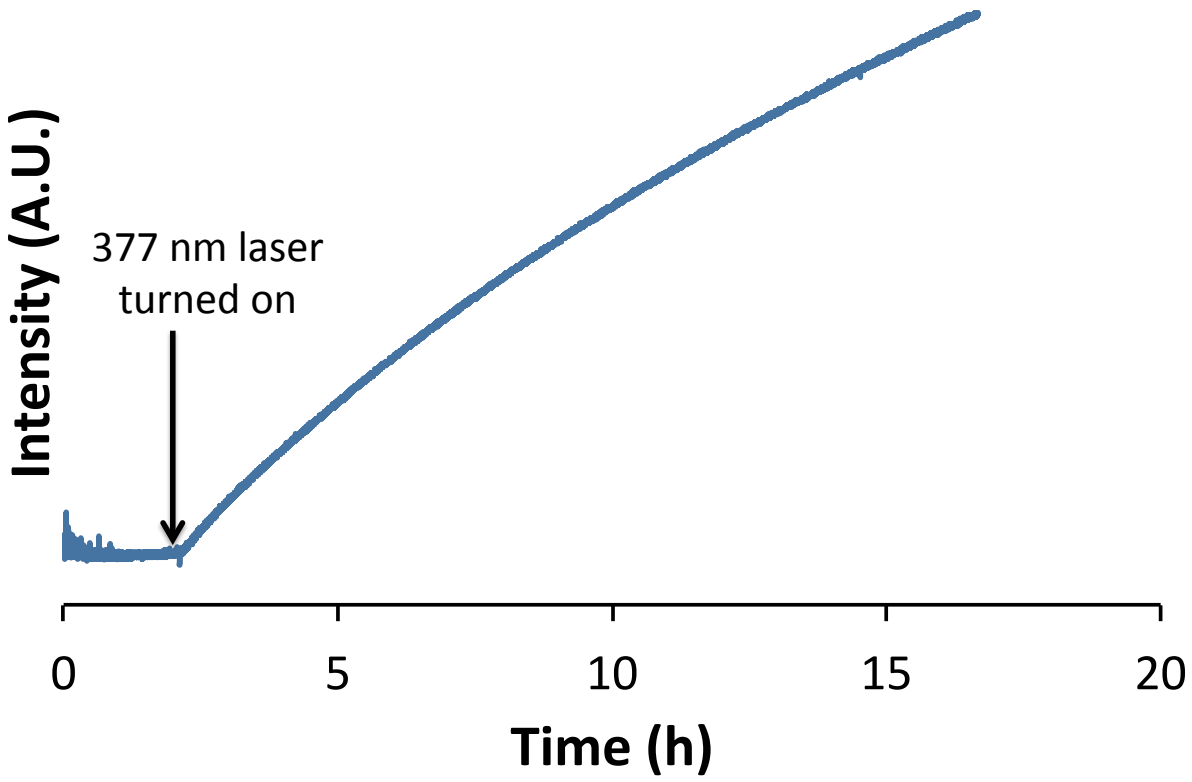

Figure 3.10 Release profile of the system. A baseline was taken for 2 hours, after which the 377 nm laser was turned on to activate the system.

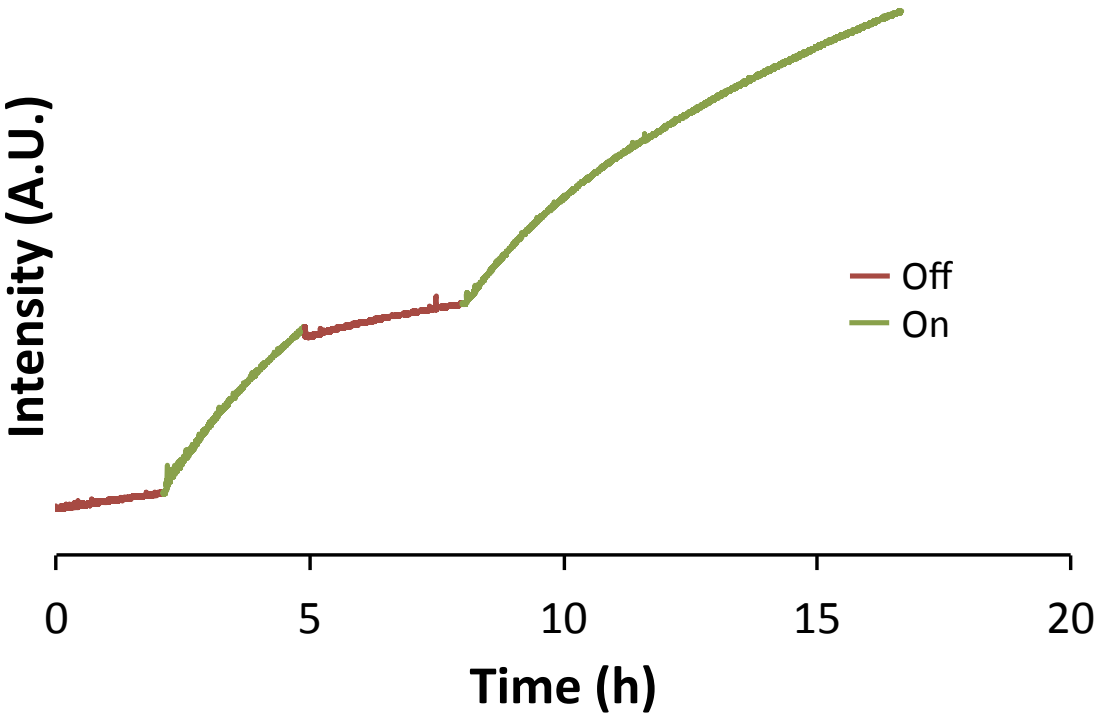

Figure 3.11 On/Off release experiment. After a 2 hour baseline, the 377 nm laser was turned on for 2 hours., then off for 2 hours, and then turned on again.

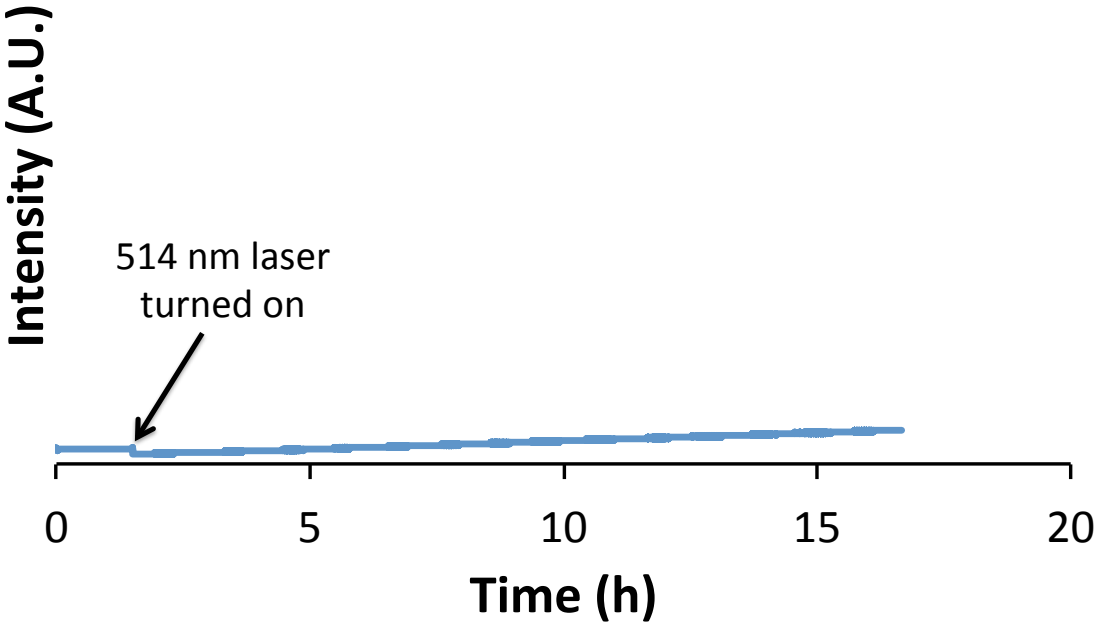

Figure 3.12 Control experiment where the particles were exposed to a 514 nm laser.

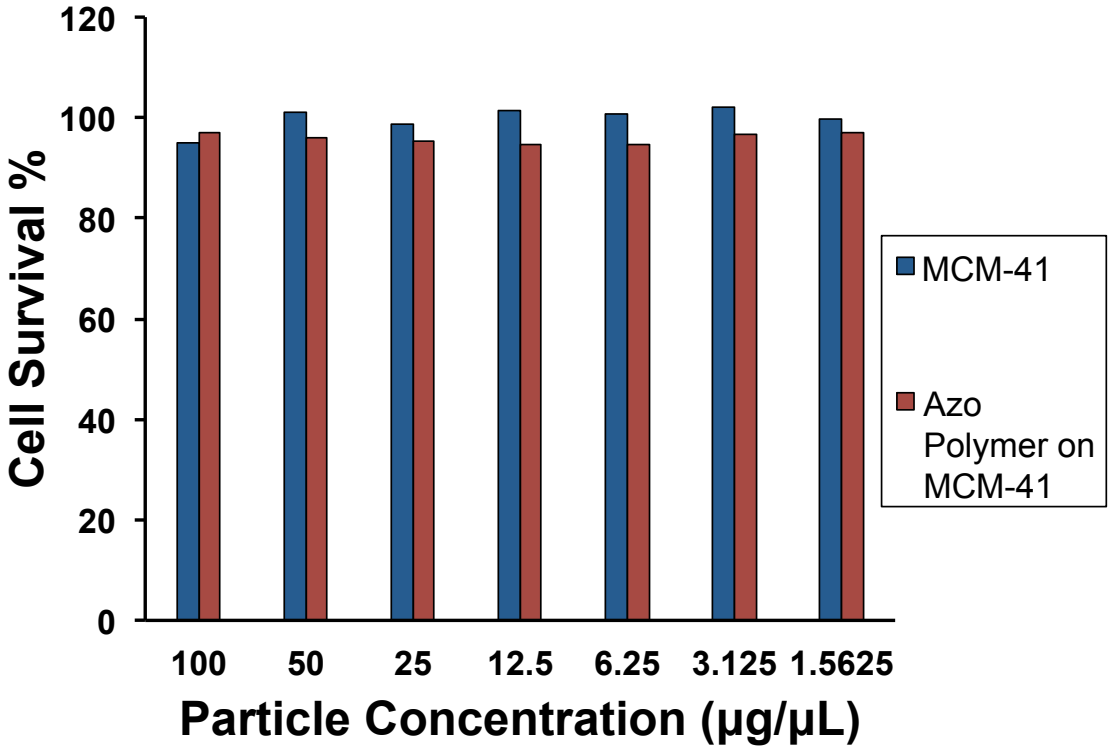

Figure 3.13 Cell toxicity study. Cells were incubated with unmodified and modified MCM-41 nanoparticles under various concentrations.

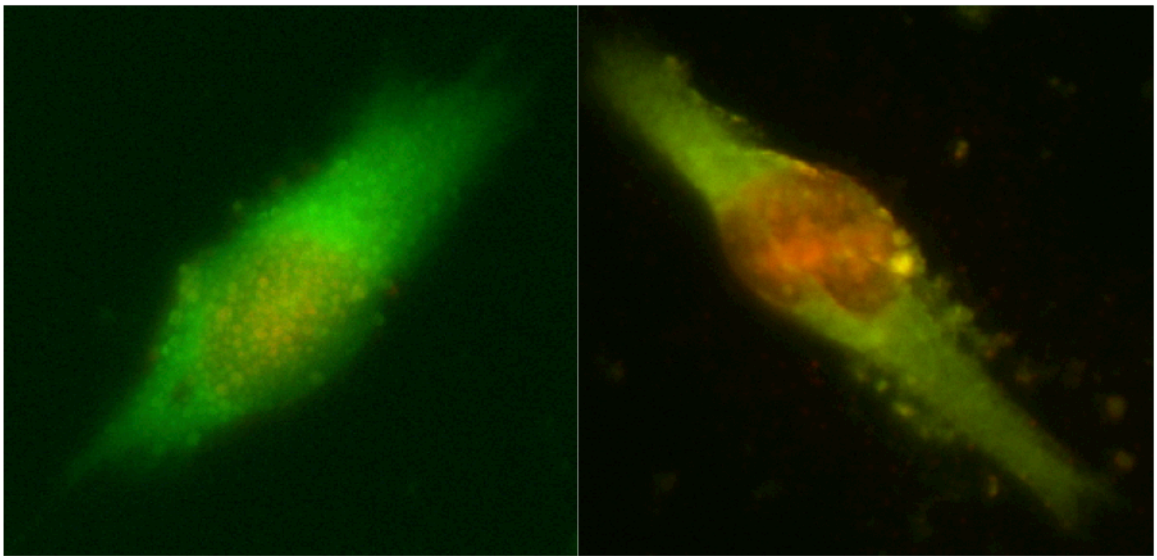

Figure 3.14 Operation of the azobenzene polymer modified MCM-41 silica nanoparticles inside of cells. The images above are representiatve of the results found. Left is an image of a cell that was not exposed to 403 nm and the right is a cell that was exposed to 403 nm. The green fluorescence are the cell membranes stained with phosphomolybdic acid. The red fluorescence is due to propidium iodide binding to the DNA of the nuclei.

3.6 References

1. Arruebo, M.; Galán, M.; Navascués, N.; Téllez, C.; Marquina, C.; Ibarra, M. R.; Santamaría, J., Development of magnetic nanostructured silica-based materials as potential vectors for drug-delivery applications. *Chemistry of materials* 2006, 18, 1911-1919.

2. Vallet‐Regí, M.; Balas, F.; Arcos, D., Mesoporous materials for drug delivery. *Angewandte Chemie International Edition* 2007, 46, 7548-7558.

3. Couvreur, P., Nanoparticles in drug delivery: Past, present and future. *Advanced Drug Delivery Reviews* 2012.

4. Ryu, J.; Cho, B.; Woo, H.-G.; Cho, S.; Sohn, H., Fabrication and Characterization of Photoluminescent Silicon Nanoparticles for Drug Delivery Applications. *Journal of Nanoscience and Nanotechnology* 2013, 13, 157-160.

5. Liong, M.; Lu, J.; Kovochich, M.; Xia, T.; Ruehm, S. G.; Nel, A. E.; Tamanoi, F.; Zink, J. I., Multifunctional inorganic nanoparticles for imaging, targeting, and drug delivery. *Acs Nano* 2008, 2, 889-896.

6. Ferris, D. P.; Zhao, Y. L.; Khashab, N. M.; Khatib, H. A.; Stoddart, J. F.; Zink, J. I., Light-operated mechanized nanoparticles. *Journal of the American Chemical Society* 2009, 131, 1686-1688.

7. Kresge, C. T.; Leonowicz, M. E.; Roth, W. J.; Vartuli, J. C.; Beck, J. S., Ordered mesoporous molecular sieves synthesized by a liquid-crystal template mechanism. *nature* 1992, 359, 710-712.

8. Brinker, C. J.; Scherer, G. W., *Sol-gel science: the physics and chemistry of sol-gel processing*. Academic Pr: 1990.

9. Ogawa, M., A simple sol–gel route for the preparation of silica–surfactant mesostructured materials. *Chemical Communications* 1996, 1149-1150.

10. Trewyn, B. G.; Slowing, I. I.; Giri, S.; Chen, H.-T.; Lin, V. S.-Y., Synthesis and functionalization of a mesoporous silica nanoparticle based on the sol–gel process and applications in controlled release. *Accounts of chemical research* 2007, 40, 846-853.

11. Ambrogio, M. W.; Thomas, C. R.; Zhao, Y.-L.; Zink, J. I.; Stoddart, J. F., Mechanized silica nanoparticles: a new frontier in theranostic nanomedicine. *Accounts of chemical research* 2011, 44, 903-913.

12. Zhao, Y.-L.; Li, Z.; Kabehie, S.; Botros, Y. Y.; Stoddart, J. F.; Zink, J. I., pH-operated nanopistons on the surfaces of mesoporous silica nanoparticles. *Journal of the American Chemical Society* 2010, 132, 13016-13025.

13. Li, Z.; Barnes, J. C.; Bosoy, A.; Stoddart, J. F.; Zink, J. I., Mesoporous silica nanoparticles in biomedical applications. *Chemical Society Reviews* 2012, 41, 2590-2605.

14. Thomas, C. R.; Ferris, D. P.; Lee, J. H.; Choi, E.; Cho, M. H.; Kim, E. S.; Stoddart, J. F.; Shin, J. S.; Cheon, J.; Zink, J. I., Noninvasive remote-controlled release of drug molecules in vitro using magnetic actuation of mechanized nanoparticles. *Journal of the American Chemical Society* 2010, 132, 10623-10625.

15. Angelos, S.; Khashab, N. M.; Yang, Y. W.; Trabolsi, A.; Khatib, H. A.; Stoddart, J. F.; Zink, J. I., pH clock-operated mechanized nanoparticles. *Journal of the American Chemical Society* 2009, 131, 12912-12914.

16. DeMuth, P.; Hurley, M.; Wu, C.; Galanie, S.; Zachariah, M. R.; DeShong, P., Mesoscale porous silica as drug delivery vehicles: Synthesis, characterization, and pH-sensitive release profiles. *Microporous and Mesoporous Materials* 2010.

17. Du, L.; Liao, S.; Khatib, H. A.; Stoddart, J. F.; Zink, J. I., Controlled-access hollow mechanized silica nanocontainers. *Journal of the American Chemical Society* 2009, 131, 15136.

18. Angelos, S.; Yang, Y. W.; Patel, K.; Stoddart, J. F.; Zink, J. I., pH‐Responsive Supramolecular Nanovalves Based on Cucurbit [6] uril Pseudorotaxanes. *Angewandte Chemie* 2008, 120, 2254-2258.

19. Fujiwara, M.; Terashima, S.; Endo, Y.; Shiokawa, K.; Ohue, H., Switching catalytic reaction conducted in pore void of mesoporous material by redox gate control. *Chemical communications* 2006, 4635-4637.

20. Saha, S.; Leung, K. F.; Nguyen, T. D.; Stoddart, J.; Zink, J. I., Nanovalves. *Advanced Functional Materials* 2007, 17, 685-693.

21. Ambrogio, M. W.; Pecorelli, T. A.; Patel, K.; Khashab, N. M.; Trabolsi, A.; Khatib, H. A.; Botros, Y. Y.; Zink, J. I.; Stoddart, J. F., Snap-top nanocarriers. *Organic Letters* 2010, 12, 3304-3307.

22. Andresen, T. L.; Thompson, D. H.; Kaasgaard, T., Enzyme-triggered nanomedicine: Drug release strategies in cancer therapy (Invited Review). *Molecular membrane biology* 2010, 27, 353-363.

23. Patel, K.; Angelos, S.; Dichtel, W. R.; Coskun, A.; Yang, Y. W.; Zink, J. I.; Stoddart, J. F., Enzyme-responsive snap-top covered silica nanocontainers. *Journal of the American Chemical Society* 2008, 130, 2382-2383.

24. Park, C.; Kim, H.; Kim, S.; Kim, C., Enzyme responsive nanocontainers with cyclodextrin gatekeepers and synergistic effects in release of guests. *Journal of the American Chemical Society* 2009, 131, 16614-16615.

25. Choi, S. K.; Thomas, T.; Li, M. H.; Kotlyar, A.; Desai, A.; Baker Jr, J. R., Light-controlled release of caged doxorubicin from folate receptor-targeting PAMAM dendrimer nanoconjugate. *Chemical Communications* 2010, 46, 2632-2634.

26. Johansson, E.; Choi, E.; Angelos, S.; Liong, M.; Zink, J. I., Light-activated functional mesostructured silica. *Journal of Sol-Gel Science and Technology* 2008, 46, 313-322.

27. Lu, J.; Choi, E.; Tamanoi, F.; Zink, J. I., Light‐Activated Nanoimpeller‐Controlled Drug Release in Cancer Cells. *Small* 2008, 4, 421-426.

28. Shamay, Y.; Adar, L.; Ashkenasy, G.; David, A., Light induced drug delivery into cancer cells. *Biomaterials* 2011, 32, 1377-1386.

29. Alvarez‐Lorenzo, C.; Bromberg, L.; Concheiro, A., Light‐sensitive Intelligent Drug Delivery Systems †. *Photochemistry and photobiology* 2009, 85, 848-860.

30. Lau, Y. A.; Ferris, D. P.; Zink, J. I. In *Photo-driven nano-impellers and nanovalves for on-command drug release*, Proceedings of SPIE, 2010; p 75740P.

31. Lai, C. Y.; Trewyn, B. G.; Jeftinija, D. M.; Jeftinija, K.; Xu, S.; Jeftinija, S.; Lin, V. S. Y., A mesoporous silica nanosphere-based carrier system with chemically removable CdS nanoparticle caps for stimuli-responsive controlled release of neurotransmitters and drug molecules. *Journal of the American Chemical Society* 2003, 125, 4451-4459.

32. Mita, I.; Horie, K.; Hirao, K., Photochemistry in polymer solids. 9. Photoisomerization of azobenzene in a polycarbonate film. *Macromolecules* 1989, 22, 558-563.

33. Yu, Y.; Ikeda, T., Photodeformable polymers: A new kind of promising smart material for micro‐and nano‐applications. *Macromolecular Chemistry and Physics* 2005, 206, 1705-1708.

34. Tong, X.; Wang, G.; Soldera, A.; Zhao, Y., How can azobenzene block copolymer vesicles be dissociated and reformed by light? *The Journal of Physical Chemistry B* 2005, 109, 20281-20287.

35. Liu, N.; Dunphy, D. R.; Atanassov, P.; Bunge, S. D.; Chen, Z.; López, G. P.; Boyle, T. J.; Brinker, C. J., Photoregulation of mass transport through a photoresponsive azobenzene-modified nanoporous membrane. *Nano letters* 2004, 4, 551-554.

36. Kinoshita, T., Photoresponsive membrane systems. *Journal of Photochemistry and Photobiology B: Biology* 1998, 42, 12-19.

37. Seki, T., Mono-and multilayers of photoreactive polymers as collective and active supramolecular systems. *Supramolecular Science* 1996, 3, 25-29.

38. Moniruzzaman, M.; Sabey, C. J.; Fernando, G. F., Synthesis of azobenzene-based polymers and the in-situ characterization of their photoviscosity effects. *Macromolecules* 2004, 37, 2572-2577.

39. Sierocki, P.; Maas, H.; Dragut, P.; Richardt, G.; Vögtle, F.; De Cola, L.; Brouwer, F.; Zink, J. I., Photoisomerization of azobenzene derivatives in nanostructured silica. *The Journal of Physical Chemistry B* 2006, 110, 24390-24398.

40. Wang, Y.; Wu, G.; Li, X.; Wang, Y.; Gao, H.; Ma, J., On–off switchable drug release from multi-responsive degradable poly (ether urethane) nanoparticles. *Biomaterials Science* 2013.

Chapter 4

Hollow Mesoporous Silica Nanoparticles Loaded with a Perchlorate Sensor

4.1 Introduction

Core/shell nanoparticles have attracted much attention in recent years due to their adaptability to many different fields such as electronics,[1-3] biomedical,[4-7] pharmaceutical,[8] optics,[9-11] and catalysis.[12, 13] As the name suggests, these materials can be defined as comprising of two or more materials where the inner material (core) and an outer layer material (shell) differ.[14] Core/shell nanoparticles can be created with properties that are not available in normal one component nanoparticles.[15] A component in core/shell nanoparticles that has attracted interest is mesoporous silica due to their robust framework, versatility, and the potential for high storage capacity. Hollow mesoporous silica nanoparticles are of particular interest because the presence of the hollow cavity can act as a reservoir, which can be controllably filled with another material yielding a core/shell nanoparticle.[16]

In this chapter, Pt(tpy)Cl]PF_6 (1•PF_6)[17] (Scheme 4.1) will be crystalized inside mechanized hollow mesoporous silica nanoparticles to create a "smart sand". This "smart sand" is a core/shell nanoparticle that can detect perchlorate anions (Figure 4.1). Perchlorate is used in munitions and explosives manufacturing and has led to groundwater and food supply contamination, which has led to many health concerns. Perchlorate interferes with the thyroid gland's ability to uptake iodine, which can cause disruption of thyroid function.[18-20] However, the detection of specific anions has been a great chemical challenge.[21, 22] 1•PF_6 has been previously reported to be the first solid-state material used for the unambiguous rapid selective detection of perchlorate in an aqueous solution.[22]

$1•PF_6$ is a semi-soluble salt that crystallizes as yellow needles and when exposed to ClO_4^- converts to $[Pt(tpy)Cl]ClO_4•H_2O$ ($1•ClO_4•H_2O$) turning the crystals red.

The absorption spectrum of the crystals has an intense tpy-centered π–π* transition near 340 nm, similar to the $Pt(tpy)Cl^+$ chromophore.[17] Immersion of the crystals in NH_4ClO_4 resulted in the appearance of a new absorption band at around 525 nm. The band is attributed to a metal–metal-to-ligand charge-transfer where the $d\sigma_s$* arises from the interaction of the d_z^2(Pt) orbitals of adjacent complexes.[17, 23] Emission studies were performed and a 532 nm laser was used to selectively excite the metal-metal-to-ligand charge-transfer transition. What was observed was that the emission from $1•PF_6$ was very weak, but once the crystals were exposed to NH_4ClO_4, there was an intense metal-metal-to-ligand charge-transfer emission at 670 nm. This is due to the fact that within each crystal structure the square planar cations stack in a head-to-tail arrangement to form one-dimensional columns (Figure 4.2). The Pt---Pt distances in the yellow crystals of $1•PF_6$ alternate between short and long, whereas the Pt atoms in red crystals of $1•ClO_4•H_2O$ form a nearly linear chain with short Pt---Pt distances.

Crystalizing $1•PF_6$ inside a mechanized mesoporous silica hollow particle will enable a controlled activation of the sensor. The mechanized silica outer shell protects and entraps $1•PF_6$ from external forces until activation of the sensor is desired (Figure 4.1). The machine picked is and acid valve composed of N-phenylaminomethyltriethoxysilane (PhAMTES) and α-cyclodextrin that has been previously reported.[16] It has been shown that α-cyclodextrin has a strong susceptibility for binding to benzene and some of its derivatives due to hydrophobic interactions.[16, 24, 25] When the pH changes from 7 to 3, the

anilinoalkane protonates and thus lowers the binding affinity causing the α-cyclodextrin to dissociate. This will allow the α-cyclodextrin to block the pore openings at neutral pH, preventing perchlorate from entering the pores until activation is desired. Even though perchlorate is a small anion it is actually one of the more hydrophobic inorganic anions[26] and thus the hydrophilic exterior of α-cyclodextrin will help keep the anions away from the pore openings. In turn, this will keep 1•PF_6 safe from perchlorate until activation is desired.

4.2 Experimental Section

4.2.1 Hollow Mesoporous Silica Nanoparticles

Hollow mesoporous silica nanoparticles will be synthesized using the sol-gel method. First, highly charged monodispersed polystyrene beads will be made by emulsion polymerization.[27, 28] The polystyrene beads will act as the template for the hollow cavity. A modified procedure using DI water, dodecyltrimethylammonium bromide (DTAB), NaOH, tetraethylorthosilicate (TEOS), and the polystyrene beads will be used to make the hollow mesoporous silica nanoparticles.[29, 30]

Synthesis of Polystyrene Beads

Polystyrene beads were made using a previously published procedure.[28] In a reaction vessel, 0.171 g of sodium bicarbonate was added to 138 mL of water under

nitrogen. The water solution was then deoxygenated by bubbling nitrogen through the solution for 40 minutes. Afterwards, 2.5 g of Aerosol MA-80-1 was dissolved in 10 mL of water and then added to the solution. The solution was brought to 50 °C and 2.33 g of divinyl benzene and 60 mL of styrene was slowing added. Sodium 1- allyloxy-2-hydroxypropane sulfonate was dissolved in 10 mL of water and was immediately injected into the solution 5 minutes after the addition of divinyl benzene and styrene. The temperature was then brought to 70 °C at which point a solution of 0.75 g of ammonium persulfate in 5 mL of water was injected. The reaction continued for 4 hours. The particles were washed through dialysis for 3 days changing the water twice a day. They were then centrifuged with water twice and then with methanol two more times. They were then left to dry under vacuum. The size of the particles was confirmed by taking a TEM image of the particles.

Synthesis of Hollow Mesoporous Silica Nanoparticles

Hollow mesoporous silica nanoparticles were synthesized by adding 0.5 g of DTAB and 0.25 g of the polystyrene beads into 20 mL of water. The solution was sonicated for 20 minutes and then allowed to rest for 30 minutes to allow any large aggregates of the polystyrene beads to settle. The solution was then carefully poured into 100 mL of water and 450 µL of 2 M NaOH was added. After 30 minutes, 500 µL of TEOS was added and the reaction was left at room temperature for 24 hours. The particles were washed thoroughly with water and methanol and then calcined at 500 °C to remove the surfactant and the

polystyrene beads. XRD was used to confirm the pore size and TEM images were taken to confirm the presence of the hollow cavity as well as to determine the particles shell thickness.

4.2.2 Hollow Particles as "Smart Sand"

Surface Modification of the Hollow Mesoporous Silica Nanoparticles

50 mg of the hollow mesoporous silica nanoparticles and 50 μL of PhAMTES were placed in 3 mL of toluene and the reaction was left overnight stirring at room temperature. The particles were then washed with methanol and then with water and then dried in a vacuum. An IR spectrum of the particles was taken to confirm the presence of PhAMTES.

Crystalizing 1•PF_6 Inside the Hollow Core

A highly concentrated solution of 1•PF_6 was made by taking 10 mg of the crystal and dissolving it in 300 μL of dimethyl sulfoxide. 20 mg of the particles were added to the solution and was left stirring for 24 hours. The solution was then allowed to slowly evaporate until the particles were dry.

Blocking the Pore Openings with α-Cyclodextrin

The particles were washed twice with dimethyl sulfoxide and then twice with water to remove any 1•PF_6 from the surface of the hollow particles. The particles were then left in 1.5 mL of water and 50 mg of α-cyclodextrin was added. The particles were then left stirring overnight. TEM images were taken to confirm the presence of 1•PF_6 inside the hollow core as well as to confirm the absence of 1•PF_6 on the surface of the particles.

Controlled Activation of the "Smart Sand"

The operation of the "smart sand" was monitored using fluorescence spectroscopy. 10 mg of the particles were placed in an NMR tube. Enough water was added to just wet the particles and the NMR tube was placed in front of a CCD. The emission of 1•PF_6 was measured as a function of time at 1 second intervals by using a 514 nm excitation beam (40 mW). The activation profile of the "smart sand" was obtained by plotting luminescence intensities of 1•PF_6 at the emission maximum (670 nm) as a function of time. 40 μL of a 30 mM solution of $NaClO_4$ was added to the sample followed by adding 40 μL of an acid solution to bring the pH to 3 in order to activate the "smart sand".

4.2.3 Characterization Methods

The structure of hollow mesoporous silica nanoparticles was confirmed by X-ray diffraction (XRD) experiments in Bragg-Brentano geometry (θ-2θ) on a Philips X'Pert Powder Diffractometer operated at 40 kV, 40 mA using CuKα radiation (λ=1.54 Å). To confirm the presence of the hollow core, shell thickness, and confirmation that 1•PF_6 crystalized inside the hollow core, transmission electron microscopy (TEM) was done. The particles were dispersed in ethanol and then deposited and dried on a carbon Cu grid. Images were recorded on a JEM1200-EX (JEOL) electron microscope operating at 50 kV. Infrared (FTIR) measurements were acquired on a Jasco Model 420 spectrometer to confirm the attachment of PhAMTES. For monitoring the emission of 1•PF_6, the samples were illuminated using the 514 nm line of a Coherent I306C argon ion laser (40 mW). The photoluminescence spectra of the samples were collected using an Acton 2300i monochromator and a Princeton Instruments CCD. A 550 nm filter was placed in front of the CCD to block stray laser light.

4.3 Results and Discussion

4.3.1 Hollow Mesoporous Silica Particles

Hollow mesoporous silica nanoparticles were synthesized using polystyrene beads

as a templating agent and DTAB for the formation of the pores. The first step was to synthesize the polystyrene beads. The polystyrene beads were synthesized by emulsion polymerization based on an already published procedure.[28] Figure 4.3 are TEM images of the polystyrene beads. The polystyrene beads are well dispersed and are approximately 90 nm in diameter. The polystyrene beads were then placed in a solution of water along with DTAB and NaOH. After the formation of the micelles, TEOS was added to the solution and the reaction was allowed to continue for 24 hours. The particles were then washed and calcined to remove the surfactant and the polystyrene beads. Figure 4.4 are TEM images of the particles after calcination. Based on these images it appears that the shell thickness was around 5 nm. The pore size of the particles was approximately 1.7 nm based on XRD (Figure 4.5).

4.3.2 Hollow Particles as "Smart Sand"

The particles were then placed in toluene and PhAMTES was added to the solution. The reaction was left stirring overnight at room temperature. The particles were then washed with water and IR was taken to confirm the attachment of the valve (Figure 4.6). Comparing the IR from the underivatized hollow particles to that of the ones treated with PhAMTES there is a broad peak at around 2900 cm^{-1} which indicates C-H stretches and a peak at around 1475 cm^{-1} which indicates aromatic C=C stretches from the phenol ring. This shows that PhAMTES has condensed onto the surface of the hollow particles. In order

to grow the 1•PF_6 crystals in the hollow cavity, a saturated solution of 1•PF_6 was made by dissolving the crystals in a solution of DMSO/H_2O. The particles were added to the concentrated solution and left to dry in the fume hood. After the particles were dry, they were washed twice with DMSO. This was to ensure that the surface of the particles didn't have any crystalized 1•PF_6 on the surface. If 1•PF_6 was crystalized onto the surface, the PhAMTES would be covered and the α-cyclodextrin would not be able to bind to the benzene. The particles were then washed with DI water and α-cyclodextrin was added to block the pore openings. Figure 4.7 are the TEM images of the mechanized hollow particles loaded with the crystalized 1•PF_6. It is clear to see that the hollow cores are partially filled with 1•PF_6. While not all the particles are loaded, most of them contain the crystalized sensor.

4.3.3 Controlled Activation of the "Smart Sand"

The "smart sand" was tested by monitoring the fluorescence intensity of 1•PF_6 using time-resolved fluorescence spectroscopy. A small sample of the particles (~10 mg) was placed in an NMR tube with a small amount of water in order to wet the sample. The NMR tube was placed in front of a CCD and a 514 nm laser was used to excite the "smart sand" so that any change in fluorescence could be monitored. The result of this experiment is shown in Figure 4.8. A baseline was taken for the first 45 minutes to establish the initial intensity of 1•PF_6. Then 40 μL of .03 M $NaClO_4$ was added to the NMR tube. As seen in Figure 4.8B, there was no increase in intensity after the addition of $NaClO_4$. The small jump in intensity

was caused by the particles shifting when the 40 μL of .03 $NaClO_4$ came into contact with the surface of the particles. No further increase in intensity was observed and after 2.5 hours, the system was brought to a pH of 3 with the addition of acid. Immediately afterwards, the fluorescence intensity increased. This indicates that the α-cyclodextrin became unbound from the anilinoalkane group allowing the ClO_4^- to enter inside the particles, converting $1•PF_6$ to $1•ClO_4•H_2O$. Figure 4.8C shows the fluorescence intensity peak at various times throughout the experiment, which coincides with what has been presented previously in literature.[22]

In order to ensure that the increase in intensity was caused by the perchlorate and not the pH change, the same experiment was conducted only no perchlorate was added to the "smart sand". Figure 4.9 shows the result of that control experiment. After one hour of baseline collection, acid was added to the particles to bring the solution to pH 3. Once again the initial change in intensity is caused by the particles shifting, but afterwards there was no change in intensity. This indicates that the acid had no effect on the increase in intensity from the previous experiment and that the increase intensity was caused only by the change from $1•PF_6$ to $1•ClO_4•H_2O$.

4.4 Conclusion

In summary, hollow mesoporous silica nanoparticles were synthesized and used to make "smart sand". The particles had a shell thickness of 5 nm and a pore size of 1.7 nm. The particles were mechanized with a known acid valve, PhAMTES, and had the

perchlorate sensor, 1•PF_6, crystalized inside the hollow core. The machine was able to protect the sensor from perchlorate until the machine was activated. Once activated, the emission intensity of the sensor will only increase in the presence of perchlorate. This "smart sand" could be useful in the detection and monitoring of perchlorate because it offers the ability to have a controlled activation of the sensor.

4.5 Figures and Tables

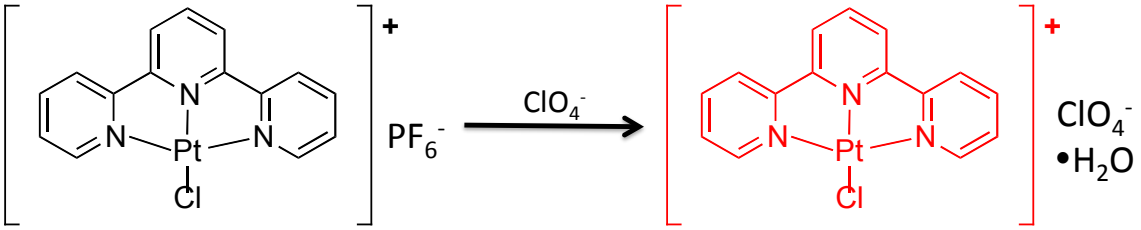

Scheme 4.1 1•PF_6 converting to 1•ClO_4•H_2O upon addition of perchlorate.

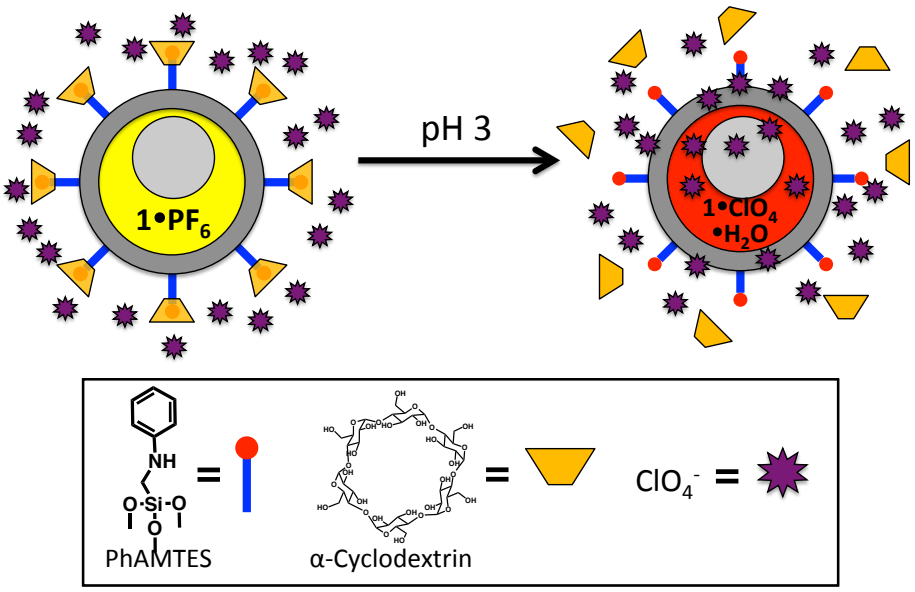

Figure 4.1 The fully assembled system (left) protects the sensor from perchlorate until pH 3 is reached. After the cap comes off, the perchlorate is able to travel through the pores of the hollow particles and reach the sensor crystal and thus activates it (right).

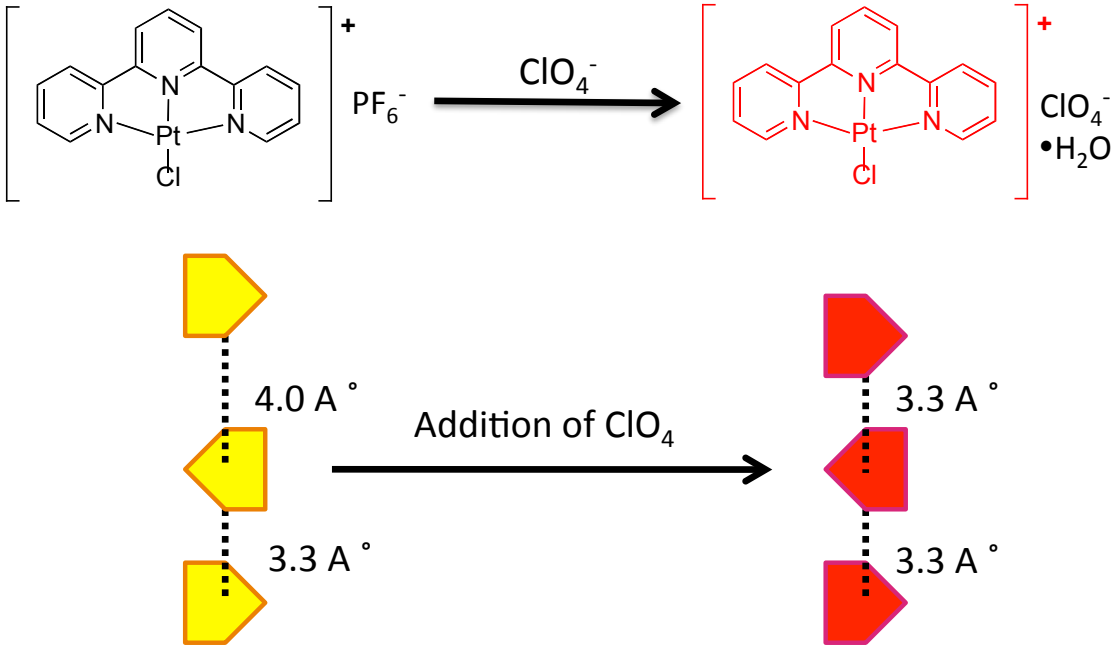

Figure 4.2 Conversion of yellow 1•PF_6 (left) to red 1•ClO_4^-•H_2O (right) upon exposure to aqueous ClO_4^-

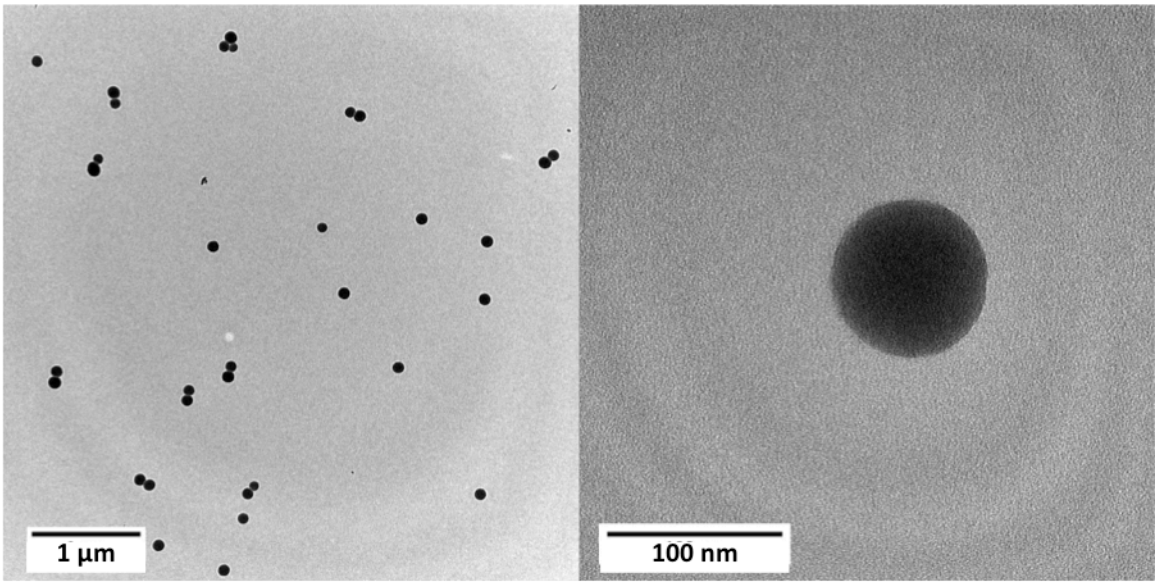

Figure 4.3 TEM images of the polystyrene beads.

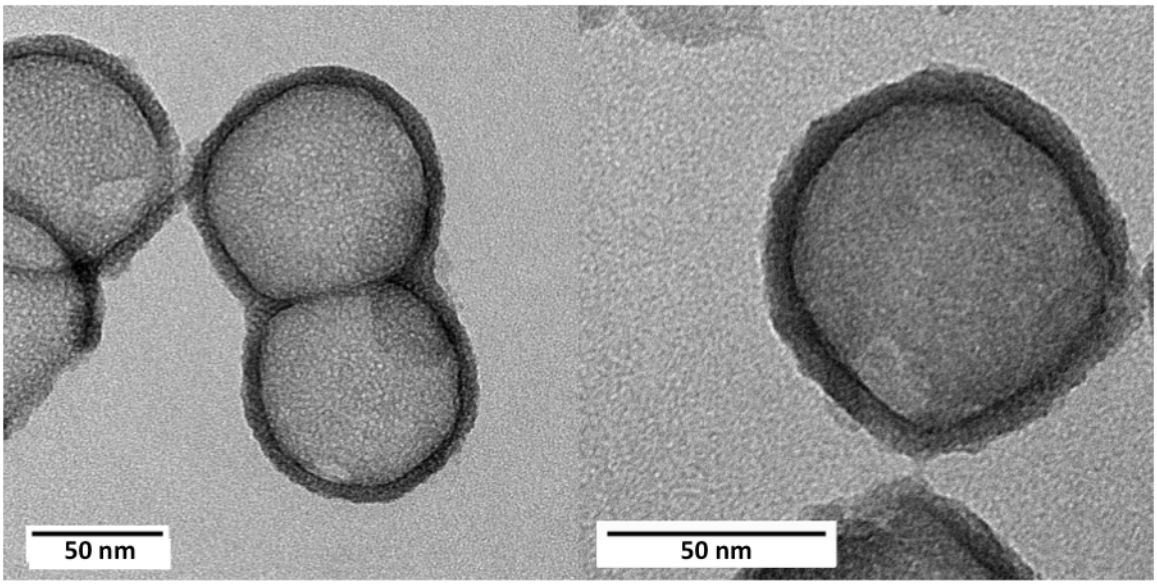

Figure 4.4 TEM images of the hollow mesoporous silica nanoparticles.

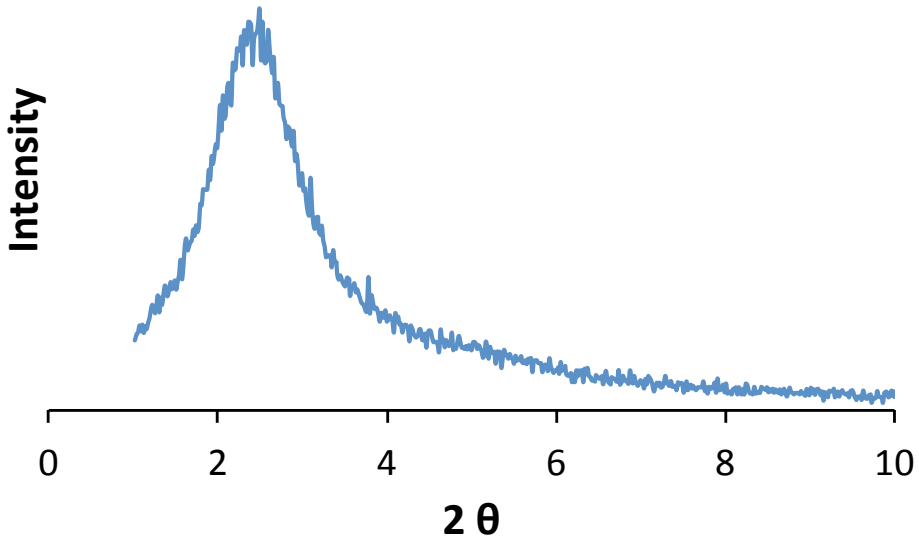

Figure 4.5 XRD of hollow mesoporous silica nanoparticles. The peak is approximately around 2.3°, giving a d spacing of 37 Å. It was then calculated that the pore size is around 1.7 nm in diameter.

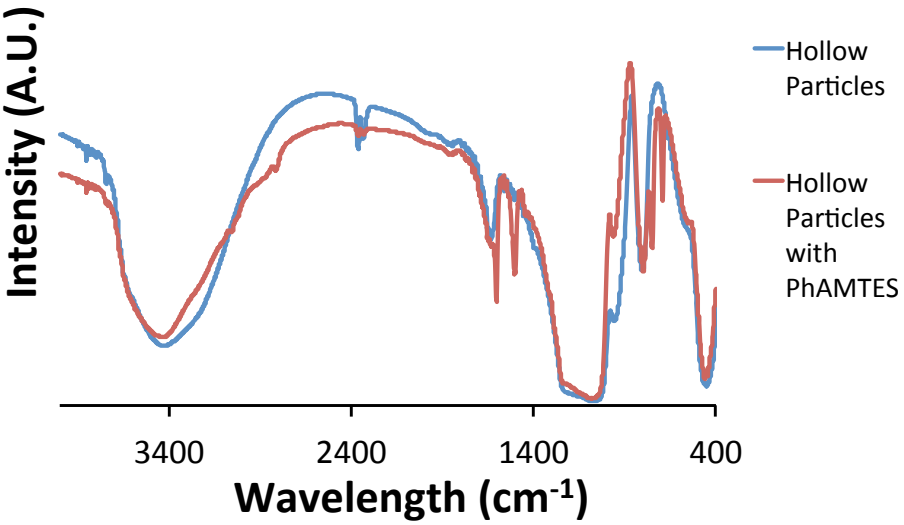

Figure 4.6 IR spectra of hollow particles and hollow particles after PhAMTES modification. 2900 cm^{-1} indicates C-H streches and 1475 cm^{-1} indicates aromatic C=C streches.

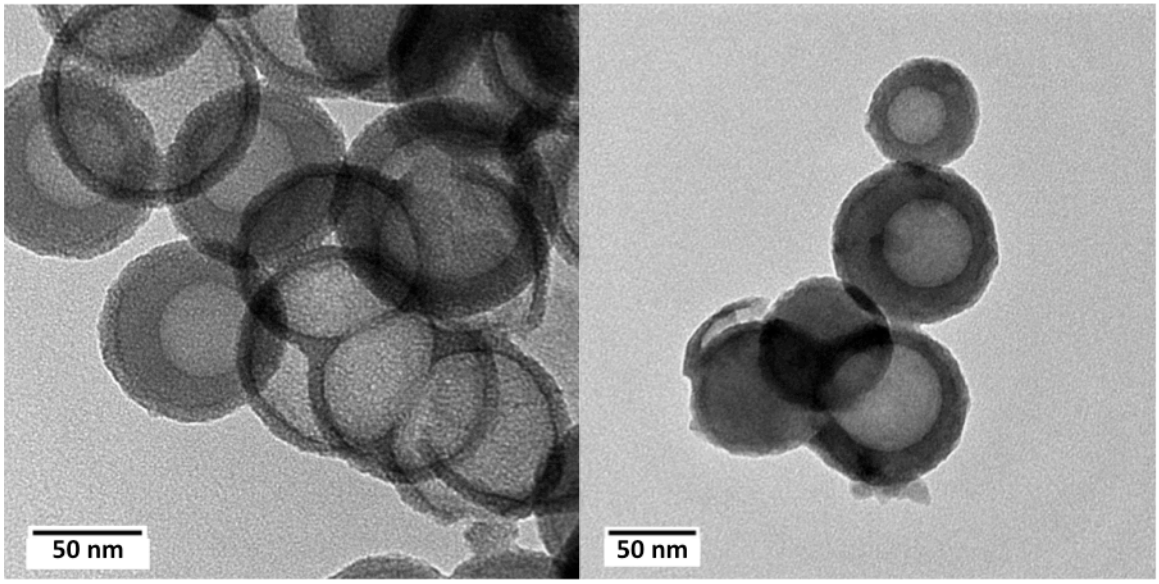

Figure 4.7 TEM images of mesoporous silica nanoparticles with $1 \bullet PF_6$ crystalized inside. Comparing the loaded particles to the unloaded ones, the unloaded particles still retains the void in the center. However, the center void for the of the particles that have $1 \bullet PF_6$ crystalized inside either has shrunk or is no longer present, which can be seen by the TEM.

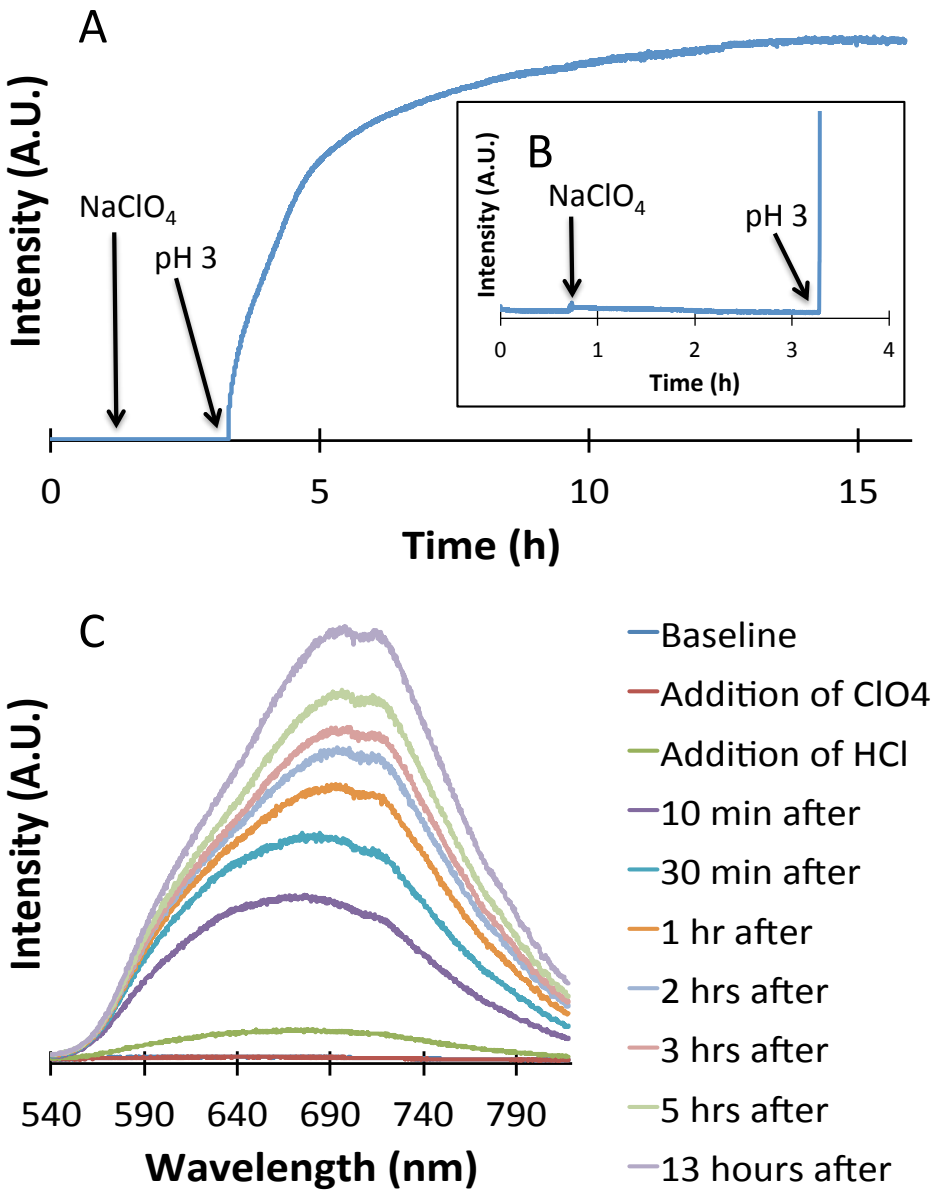

Figure 4.8 Time resolved florescence spectroscopy of the system (Figure 2A). At ~45 mins $NaClO_4^-$ was added and after 2.5 hours the system was brought to a ph of 3. Figure 2B is close up of when $NaClO_4^-$ was added and when the system changed to a ph of 3. Figure 2C is the emission spectrum taken at various points.

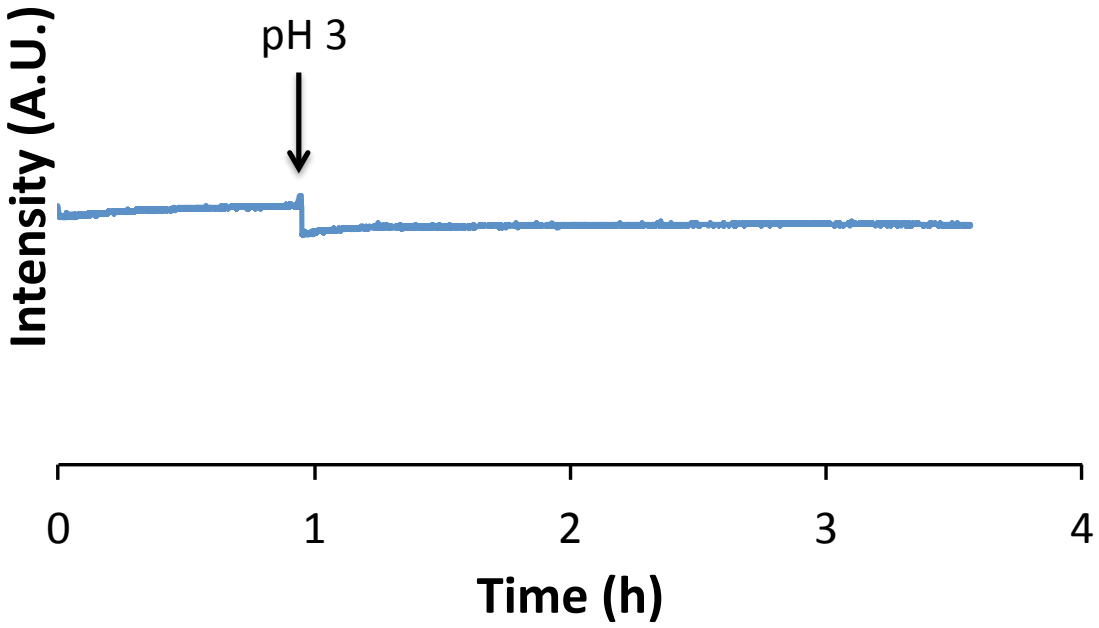

Figure 4.9 After ~ 1hr. the sensor loaded hollow particles were brought to a pH of 3 and the emission was monitored.

4.6 References

1. Hoener, C. F.; Allan, K. A.; Bard, A. J.; Campion, A.; Fox, M. A.; Mallouk, T. E.; Webber, S. E.; White, J. M., Demonstration of a shell-core structure in layered cadmium selenide-zinc selenide small particles by x-ray photoelectron and Auger spectroscopies. *The Journal of Physical Chemistry* 1992, 96, 3812-3817.

2. Kortan, A.; Hull, R.; Opila, R.; Bawendi, M.; Steigerwald, M.; Carroll, P.; Brus, L. E., Nucleation and growth of cadmium selendie on zinc sulfide quantum crystallite seeds, and vice versa, in inverse micelle media. *Journal of the American Chemical Society* 1990, 112, 1327-1332.

3. Qi, L.; Ma, J.; Cheng, H.; Zhao, Z., Synthesis and characterization of mixed CdS 瑎 ZnS nanoparticles in reverse micelles. *Colloids and Surfaces A: Physicochemical and Engineering Aspects* 1996, 111, 195-202.

4. Balakrishnan, S.; Bonder, M. J.; Hadjipanayis, G. C., Particle size effect on phase and magnetic properties of polymer-coated magnetic nanoparticles. *Journal of magnetism and magnetic materials* 2009, 321, 117-122.

5. Kim, M.-J.; Choa, Y.-H.; Kim, D. H.; Kim, K. H., Magnetic behaviors of surface modified superparamagnetic magnetite nanoparticles. *Magnetics, IEEE Transactions on* 2009, 45, 2446-2449.

6. Laurent, S.; Forge, D.; Port, M.; Roch, A.; Robic, C.; Vander Elst, L.; Muller, R. N., Magnetic iron oxide nanoparticles: synthesis, stabilization, vectorization, physicochemical characterizations, and biological applications. *Chemical reviews* 2008, 108, 2064.

7. Salgueiriño‐Maceira, V.; Correa‐Duarte, M. A., Increasing the complexity of magnetic core/shell structured nanocomposites for biological applications. *Advanced Materials* 2007, 19, 4131-4144.

8. Caruso, F., Nanoengineering of particle surfaces. *Advanced Materials* 2001, 13, 11-22.

9. Amalvy, J.; Percy, M.; Armes, S.; Wiese, H., Synthesis and characterization of novel film-forming vinyl polymer/silica colloidal nanocomposites. *Langmuir* 2001, 17, 4770-4778.

10. Lal, M.; Levy, L.; Kim, K.; He, G.; Wang, X.; Min, Y.; Pakatchi, S.; Prasad, P., Silica nanobubbles containing an organic dye in a multilayered organic/inorganic

heterostructure with enhanced luminescence. *Chemistry of materials* 2000, 12, 2632-2639.

11. Xu, X.; Friedman, G.; Humfeld, K. D.; Majetich, S. A.; Asher, S. A., Synthesis and utilization of monodisperse superparamagnetic colloidal particles for magnetically controllable photonic crystals. *Chemistry of materials* 2002, 14, 1249-1256.

12. Daniel, M.-C.; Astruc, D., Gold nanoparticles: assembly, supramolecular chemistry, quantum-size-related properties, and applications toward biology, catalysis, and nanotechnology. *Chemical Reviews-Columbus* 2004, 104, 293.

13. Phadtare, S.; Kumar, A.; Vinod, V.; Dash, C.; Palaskar, D. V.; Rao, M.; Shukla, P. G.; Sivaram, S.; Sastry, M., Direct assembly of gold nanoparticle "shells" on polyurethane microsphere "cores" and their application as enzyme immobilization templates. *Chemistry of materials* 2003, 15, 1944-1949.

14. Chaudhuri, R. G.; Paria, S., Core/shell nanoparticles: classes, properties, synthesis mechanisms, characterization, and applications. *Chem. Rev* 2012, 112, 2373-433.

15. Lee, I. S.; Lee, N.; Park, J.; Kim, B. H.; Yi, Y.-W.; Kim, T.; Kim, T. K.; Lee, I. H.; Paik, S. R.; Hyeon, T., Ni/NiO core/shell nanoparticles for selective binding and magnetic separation of histidine-tagged proteins. *Journal of the American Chemical Society* 2006, 128, 10658-10659.

16. Du, L.; Liao, S.; Khatib, H. A.; Stoddart, J. F.; Zink, J. I., Controlled-access hollow mechanized silica nanocontainers. *Journal of the American Chemical Society* 2009, 131, 15136.

17. Bailey, J. A.; Hill, M. G.; Marsh, R. E.; Miskowski, V. M.; Schaefer, W. P.; Gray, H. B., Electronic Spectroscopy of Chloro (terpyridine) platinum (II). *Inorganic Chemistry* 1995, 34, 4591-4599.

18. Yu, K. O.; Narayanan, L.; Mattie, D. R.; Godfrey, R. J.; Todd, P. N.; Sterner, T. R.; Mahle, D. A.; Lumpkin, M. H.; Fisher, J. W., The pharmacokinetics of perchlorate and its effect on the hypothalamus–pituitary–thyroid axis in the male rat. *Toxicology and applied pharmacology* 2002, 182, 148-159.

19. Clewell, R. A.; Merrill, E. A.; Narayanan, L.; Gearhart, J. M.; Robinson, P. J., Evidence for competitive inhibition of iodide uptake by perchlorate and translocation of perchlorate into the thyroid. *International journal of toxicology* 2004, 23, 17-23.

20. Wolff, J., Perchlorate and the thyroid gland. *Pharmacological reviews* 1998, 50, 89-106.

21. Bendikov, T. A.; Harmon, T. C., Long-lived solid state perchlorate ion selective sensor based on doped poly (3, 4-ethylenedioxythiophene)(PEDOT) films. *Analytica chimica acta* 2005, 551, 30-36.

22. Taylor, S. D.; Howard, W.; Kaval, N.; Hart, R.; Krause, J. A.; Connick, W. B., Solid-state materials for anion sensing in aqueous solution: highly selective colorimetric and luminescence-based detection of perchlorate using a platinum (ii) salt. *Chem. Commun.* 2010, 46, 1070-1072.

23. Miskowski, V. M.; Houlding, V. H., Electronic spectra and photophysics of platinum (II) complexes with. alpha.-diimine ligands. Solid-state effects. 1. Monomers and ligand. pi. dimers. *Inorganic Chemistry* 1989, 28, 1529-1533.

24. Golovanov, I.; Zhenodarova, S.; Tsygankova, I., Quantitative structure-property relationship: XXVII. Estimation of the free energy of formation of host-guest complexes of α-cyclodextrin with benzene derivatives. *Russian journal of general chemistry* 2006, 76, 267-271.

25. Chen, W.; Chang, C.-E.; Gilson, M. K., Calculation of cyclodextrin binding affinities: energy, entropy, and implications for drug design. *Biophysical journal* 2004, 87, 3035-3049.

26. Urbansky, E. T., Perchlorate chemistry: implications for analysis and remediation. *Bioremediation Journal* 1998, 2, 81-95.

27. Shen, S.-C.; Ng, W. K.; Shi, Z.; Chia, L.; Neoh, K. G.; Tan, R. B. H., Mesoporous silica nanoparticle-functionalized poly (methyl methacrylate)-based bone cement for effective antibiotics delivery. *Journal of Materials Science: Materials in Medicine* 2011, 22, 2283-2292.

28. Reese, C. E.; Guerrero, C. D.; Weissman, J. M.; Lee, K.; Asher, S. A., Synthesis of highly charged, monodisperse polystyrene colloidal particles for the fabrication of photonic crystals. *Journal of colloid and interface science* 2000, 232, 76-80.

29. Jiao, Y.; Guo, J.; Shen, S.; Chang, B.; Zhang, Y.; Jiang, X.; Yang, W., Synthesis of discrete and dispersible hollow mesoporous silica nanoparticles with tailored shell thickness for controlled drug release. *Journal of Materials Chemistry* 2012, 22, 17636-17643.

30. Wu, W.; Caruntu, D.; Martin, A.; Yu, M.; O'Connor, C.; Zhou, W.; Chen, J.-F., Synthesis of magnetic hollow silica using polystyrene bead as a template. *Journal of magnetism and magnetic materials* 2007, 311, 578-582.

Chapter 5

PMOs Mechanized with an Acid Valve

5.1 Introduction

Since its first discovery in 1992, periodic mesoporous silica has garnered much attention.[1] Creating materials with ordered and uniform pores around 2 nm would allow for host-guest chemistry with large molecules. It has been shown that the co-assembly of surfactant micelles and a silica precursor, like tetraethyl orthosilicate (TEOS), forms a nanocomposite with ordered cylindrical pores.[2-4] After this discovery there was much research in incorporating organic groups into the silica matrix. This gained must interest because it would allow the material to be imbued with different properties. This was either done by grafting organic groups onto the pore walls by reacting the silanol groups in the material after synthesis, or by co-condensation techniques using TEOS and an organosiloxane group of type $RSi(OEt)_3$.[5-7] There are, however, limitations to these approaches.[8, 9] Both of these synthesis methods can lead to an inhomogeneous distribution of the organic groups throughout the material. Also, the silsesquioxane precursors with organic groups must be co-condensed with TEOS to form a stable periodic mesoporous structure. This can limit the amount of organic content in the material.

To solve these issues, a new class of organic/inorganic nano materials was made known as “periodic mesoporous organosilicas”, or PMOs.[10-13] The organic groups in PMOs are located within the pore walls as bridges between the Si centers, $(EtO)_3Si\text{-}R\text{-}Si\text{-}(OEt)_3$.[14-17] These materials are prepared similarly to periodic mesoporous silica and posses the high degree of order and uniformity of pores. This occurs as long as the organic group, R, is short and rigid and the molecule has favorable condensation kinetics. This helps in

ensuring a homogenous distribution of the organic groups in the pore walls. Many bridge-bonded organic groups have been incorporated and studied in PMOs.[18]

In this chapter PMOs were synthesized using TEOS and the bridged silsesquioxane bis[(3-trimethoxysilyl)propyl]amine (BTMSPA). This silsesquioxane has been used previously along with 1,2-bis(triethoxysilyl)ethane in order to make a dual bridged amine PMO particle.[19] By taking TEOS and co-condensing it with BTMSPA the number of Si-OH groups on the surface would be greater than that of a pure BTMSPA PMO. This allows for further modification after synthesis. By condensing a previously studied acid valve, N-phenylaminopropyltrimethoxysilane (PhAPTMS),[14, 20] onto the surface and using α-cyclodextrin as a capping agent, the PMO would become mechanized and allow the entrapment of cargo molecules inside the pores (Figure 5.1). Under neutral conditions, the α-cyclodextrin will bind with the anilinoalkane group and, due to it's size, will block the pore openings. However, when the pH is lowered to 5 the binding affinity between α-cyclodextrin and the anilinoalkane group diminishes because of the protonation of the aniline, which causes the dissociation of the α-CD and the unblocking of the pore openings. In this chapter, two PMOs were synthesized with different ratios of BTMSPA/TEOS incorporated into the silica matrix. PMO 1 has a ratio of 1/10 and PMO 2 has a ratio of 1/20. The physical properties of these particles were studied as well as their ability to trap and release cargo molecules.

5.2 Experimental Section

The first step is to synthesize PMO 1 and PMO 2 using different ratios of BTMSPA/TEOS. The properties of these particles will be studied before the attachment of the machine. The machine used for the release studies is an acid valve based off on PhAPTMS and α-cyclodextrin, which operates at pH 5.

5.2.1 Synthesis of PMOs

To synthesize PMO 1, 219 mg of CTAB was dissolved in 116 mL of water and 17 mL of ethylene glycol. 6 mL of NH_4OH was added to make the solution basic. The solution was brought to 60 °C and 0.67 mL of TEOS and 0.05 BTMSPA were added slowly. The reaction was left to continue for 4 hrs. while stirring. Afterwards, the stir plate was turned off and the solution remained at 60 °C for 20 hrs. under static conditions. The particles were then collected by centrifugation and washed with water and methanol. The surfactant was removed by refluxing the particles in 40 mL of ethanol and 2 mL of HCl for 16 hrs. The particles were then left to dry at room temperature. In order to make PMO 2 the same exact procedure was followed except that 0.10 mL of BTMSPA was used.

5.2.2 Mechanized PMOs

50 mg of the PMO particles were placed in 5 mL of toluene. 40 μL of PhAPTMS was added to the solution and the reaction was left for 24 hrs. to make sure PhAPTMS condenses fully onto the surface of the PMOs. The particles were washed with methanol and allowed to dry. Once the particles are completely dry they were submerged in 1 mL aqueous solution of 1 mM Rhodamine B solution. The particles were left to load for a day and then 50 mg of α-cyclodextrin was added to the solution. This was left for two days to ensure that the α-cyclodextrin associates with the anilinoalkane group in PhAPTMS in order to efficiently block the pore openings. The particles were then washed thoroughly with water and allowed to dry.

5.2.3 Characterization

The structure of MCM-41 was investigated by X-ray diffraction (XRD) experiments in Bragg-Brentano geometry (θ-2θ) on a Philips X'Pert Powder Diffractometer operated at 40 kV, 40 mA using CuKα radiation (λ=1.54 Å). To see the size of the particles, transmission electron microscopy (TEM) was used. The particles were dispersed in ethanol and then deposited and dried on a carbon Cu grid. Micrographs were recorded on a JEM1200-EX (JEOL) electron microscope operating at 50 kV. Zeta-potential values for the samples, as well as dynamic light scattering (DLS) measurements, were measured by a ZetaSizer Nano

(Malvern Instruments Ltd., Worcestershire, UK). For elemental analysis, 20 mg of the samples were shipped to Midwest Microlabs in Indianapolis, Indiana.

The time resolved controlled released profiles were obtained using fluorescence spectroscopy recorded by Acton SpectraPro 2300i and a CCD. The excitation source was a CUBE 375 (Coherent Inc., Santa Clara, CA, USA). A 430 nm filter was placed in front of the CCD to block stray laser light.

5.3 Results and Discussion

5.3.1 Physical Properties of the PMOs

Elemental Analysis

Samples of PMO 1 and PMO 2 were sent to Midwest Laboratories in order to find the carbon, nitrogen, oxygen, and hydrogen content of these particles. Table 5.1 are the results of the elemental analysis. The percent ash is the remaining SiO_2 for the particles and the percent oxygen is the oxygen that was absorbed onto the surface of SiO_2. As seen in the table, the amount of carbon and nitrogen slightly increases from PMO 1 and PMO 2. This is to be expected since the amount of BTMSPA that was added to PMO 2 is twice as much. However, the percentage of nitrogen does not double from PMO 1 and PMO 2. This means that even though twice as much of BTMSPA was added, not all of it was co-condensed with the TEOS.

Table 5.2 shows the theoretical mass ratios of nitrogen/carbon and nitrogen/silica compared with the elemental analysis conducted by Midwest Laboratories. The nitrogen/carbon ratio should be the same for both samples since in BTMSPA there is one nitrogen per six carbons. Looking at the table, PMO 2 comes very close to that ratio, but PMO 1 is slightly off. When comparing the nitrogen/silica ratio the values for both PMO 1 and PMO 2 are slightly more than what was expected. The reason why all these values are off is because there was such a small amount of nitrogen in the PMOs that the elemental analysis could have a significant error. Despite this, the ratio of nitrogen/silica does increase as well as the percent of nitrogen from PMO 1 to PMO 2 indicating that PMO 2 does contain more of the BTMSPA in its silica matrix.

Size and Pore Diameter of the PMOs

In order to determine the individual size of the particles, TEM images (Figure 5.2) were taken of PMO 1 and PMO 2. Based on these images the particles appear to be well dispersed with a size distribution of 50-100 nm in diameter. DLS was conducted on these particles in water (Figure 5.3) and the average diameter for PMO 1 and PMO 2 are approximately 600 nm and 500 nm respectively. This indicates that in an aqueous solution, these particles start to aggregate together. To see how these particles react in a cell culture medium, the PMOs were placed in Dulbecco's Modified Eagle Medium (DMEM), which contains 10% fetal calf serum, 100 μ/mL penicillin, 100 μg/mL streptomycin, and 2 mM L-glutamine. As shown in Figure 5.4, the particles aggregate even more bringing the average

size to around 900 nm for both PMO 1 and PMO 2. This is most likely caused by the interaction of these PMOs with the proteins in the solution. The BTMSPA could be the reason why these particles aggregate in solution.

The pore size of these particles was determined by XRD (Figure 5.5). PMO 1 and PMO 2 both have pore sizes around 2 nm.

Zeta Potential

Zeta potentials of these particles were taken at various pH conditions in an aqueous solution. Figure 5.6 is the results of those experiments. Under neutral conditions the zeta potential of PMO 1 is 28 and PMO 2 is 33. This makes sense since there is more of the BTMSPA in PMO 2 and thus those particles should be more positively charged. When the pH decreases the zeta potential plateaus, indicating that the particle is fully protonated. However, when the pH increases the zeta potential goes to negative values. This is because the BTMSPA is getting deprotonated causing the particles to become negatively charged.

5.3.2 Release Studies

A small sample of the mechanized PMO 1 was placed in the corner of a 1 X 2 cm cuvette. The cuvette was filled with 6 mL of water and placed on a stir plate in front of the CCD. A 377 nm laser was used to track the fluorescence of Rhodamine B. After a 2 hr. baseline was taken, a solution of acid was added into the cuvette, which brought the pH to

5. The same procedure was followed for the release study of PMO 2. The results of these experiments are shown in Figure 5.7. The baseline for both samples shows that they are leaky. This is because Rhodamine B is a positively charged dye and any dye that got adhered onto the surface of the PMOs, which are also positively charged, easily comes off the surface due to repulsion. As shown in Figure 5.7, PMO 2's baseline has a slightly higher slope. This is because PMO 2 is more positively charged than PMO 1, which was confirmed by its zeta potential. After the addition of acid, both particles show a release of Rhodamine B. PMO 1, however, releases more Rhodamine B than PMO 2. This is because PMO 2 is more positively charged. Therefore, the positively charged Rhodamine B has a harder time entering the pores of PMO 2. However, despite both particles having BTMSPA incorporated into the silica matrix, both particles successfully had PhAPTMS condensed onto the surface of the particles, both particles were able to have Rhodamine B loaded into the pores, and both particles were able to demonstrate a controlled release of Rhodamine B.

5.4 Conclusion

PMOs were synthesized with different amounts of BTMSPA. The pore size of these particles was ~2 nm in diameter which was confirmed through XRD. The range of size of these particles, determined by TEM, was approximately 50-100 nm in diameter. However, according to DLS measurements the particles have a tendency to slightly aggregate under aqueous conditions and form large aggregates when placed in a cell culture medium. PMO 2 has a higher zeta potential and is more positively charged than PMO 1 due to the increased

amount of BTMSPA. The carbon and nitrogen content of these particles was determined through elemental analysis.

Release studies of these particles were conducted and it was found that with more BTMSPA in the silica matrix the less Rhomdaine B gets loaded into the pores. This is due to the fact that the particles and Rhodamine B are positively charged. Despite this, both particles were able to trap and release dye through the use of an acid valve.

5.5 Figures and Tables

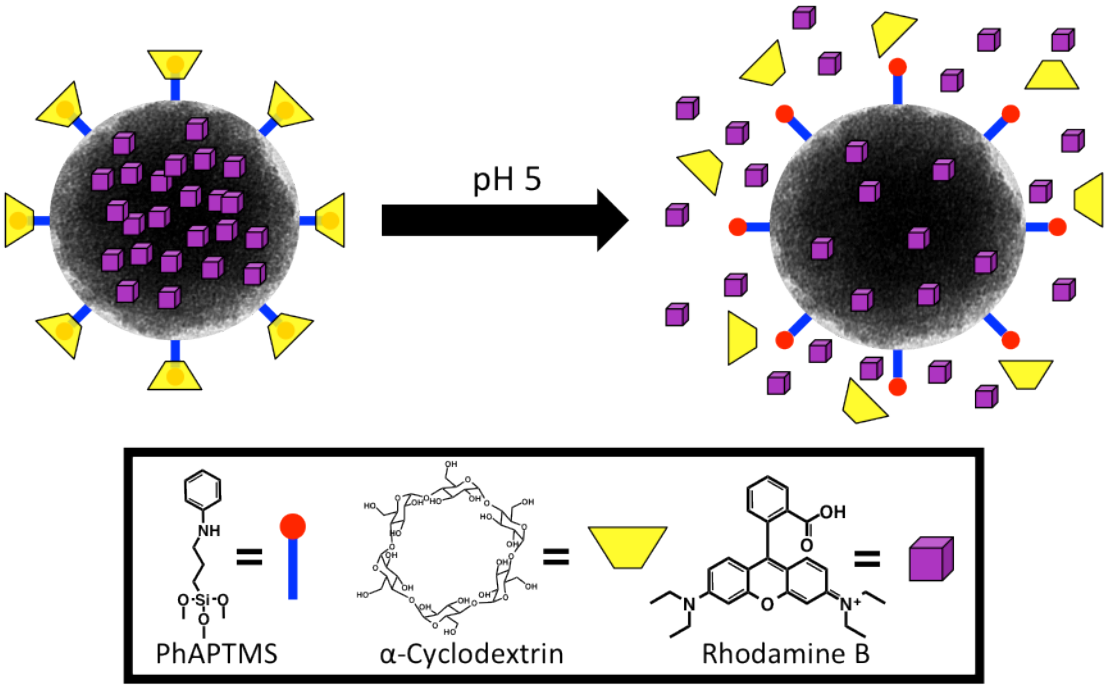

Figure 5.1 Overall scheme of the system. PhAPTMS is condensed onto the surface of the PMO, loaded with Rhodamine B and capped with α-cyclodextrin. When the pH is brought to 5 the α-cyclodextrin dissociates from the PhAPTMS allowing the Rhodamine B to be released.

	PMO 1	PMO 2
%C	7.84	10.36
%H	2.15	2.8
%N	1.29	1.99
%O*	5.57	4.2
% Ash	83.1	80.2

Table 5.1 Elemental analysis of PMO 1 and PMO2.

	PMO 1	PMO 2
N/C ratio Theoretical	0.1944	0.1944
Actual	0.1645	0.1921
N/SI ratio Theoretical	0.0227	0.0417
Actual	0.0332	0.0529

Table 5.2 Calculated and actual ratios of N/C and N/Si in PMO 1 and PMO 2.

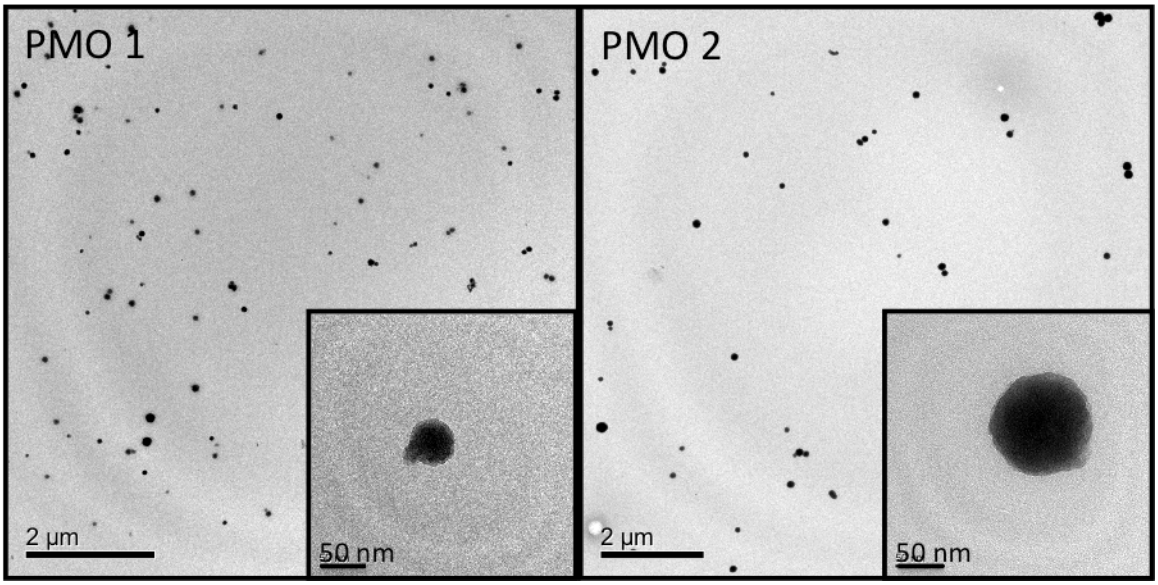

Figure 5.2 TEM images of PMO 1 (left) and PMO 2 (right). The size distribution is roughly 50-100 nm.

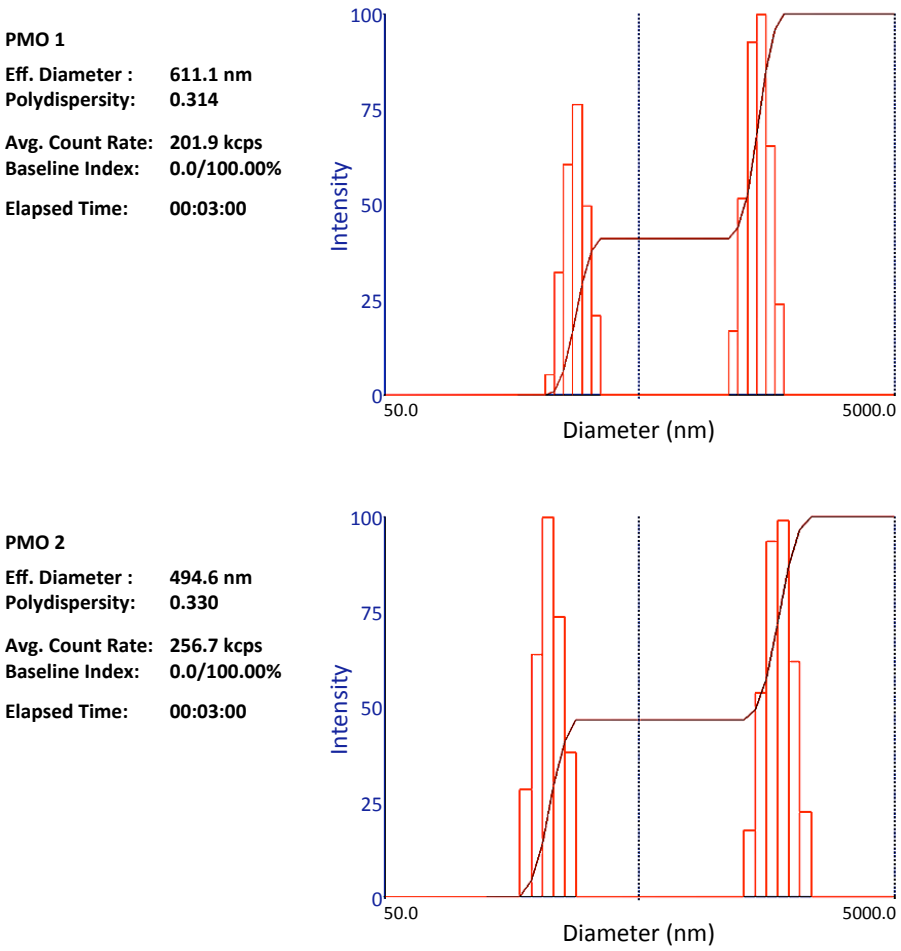

Figure 5.3 DLS of PMO 1 and PMO 2 in deionized water.

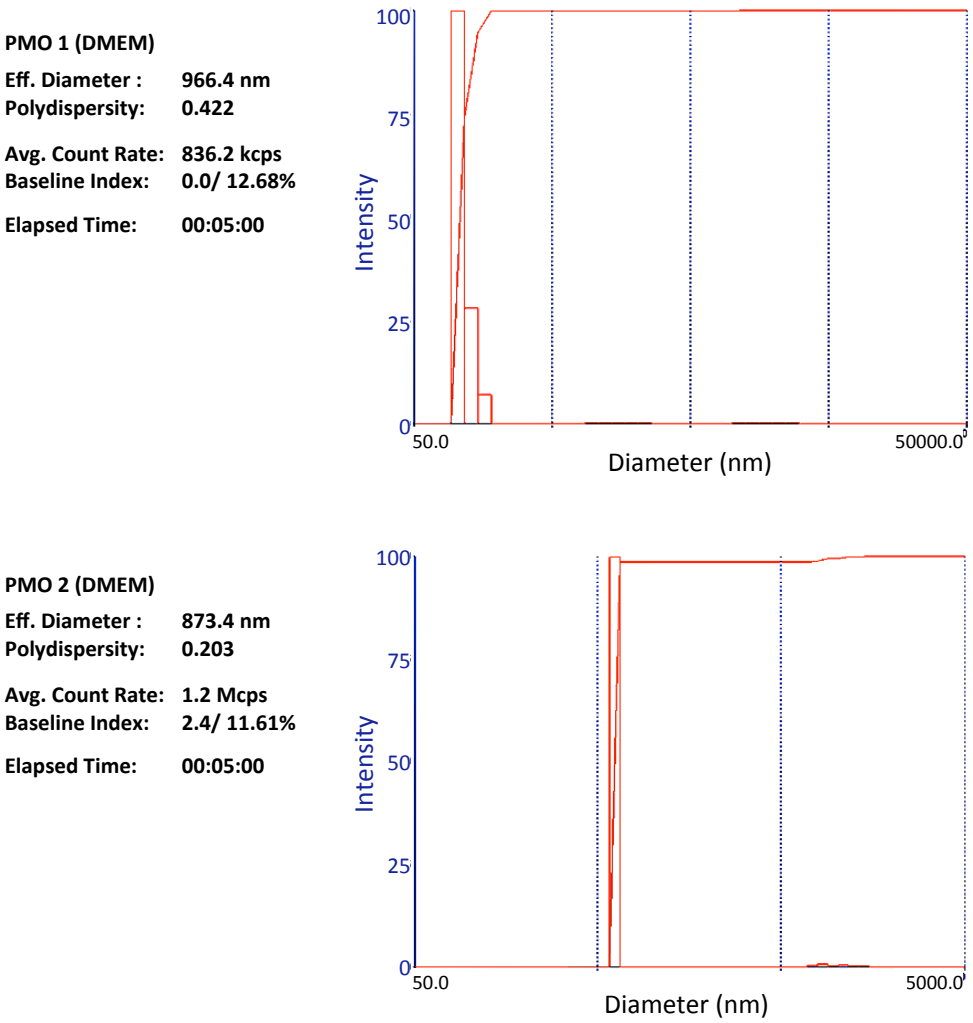

Figure 5.4 DLS of PMO 1 and PMO 2 in DMEM.

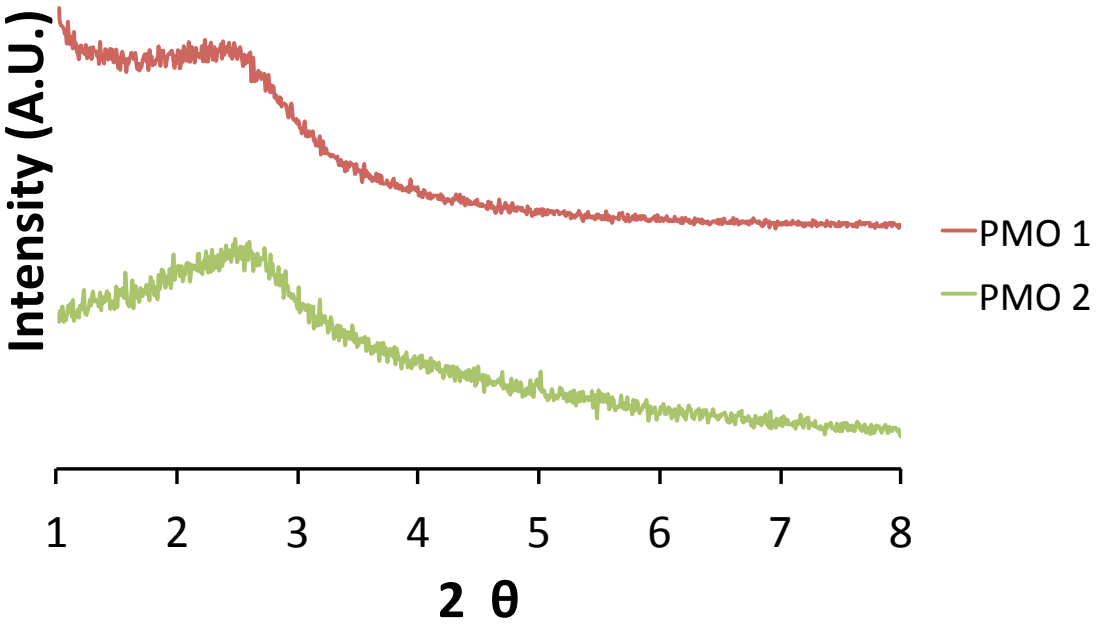

Figure 5.5 XRD of PMO 1 (red trace) and PMO 2 (green trace).

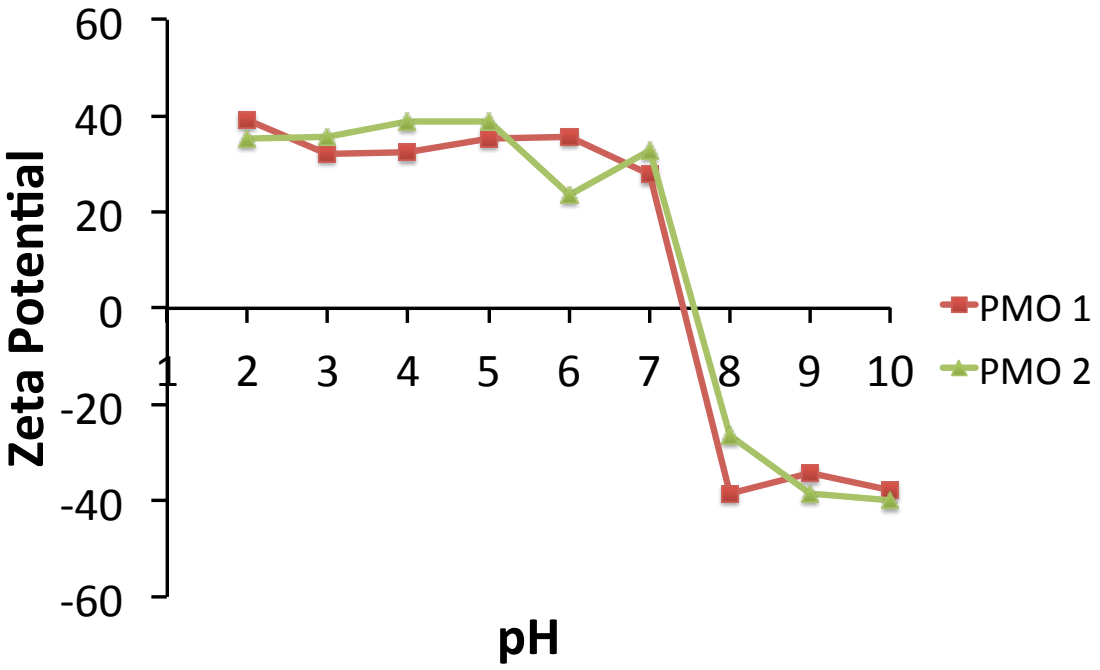

Figure 5.6 Zeta potentials of PMO 1 (red trace) and PMO 2 (green trace) under various pH conditions.

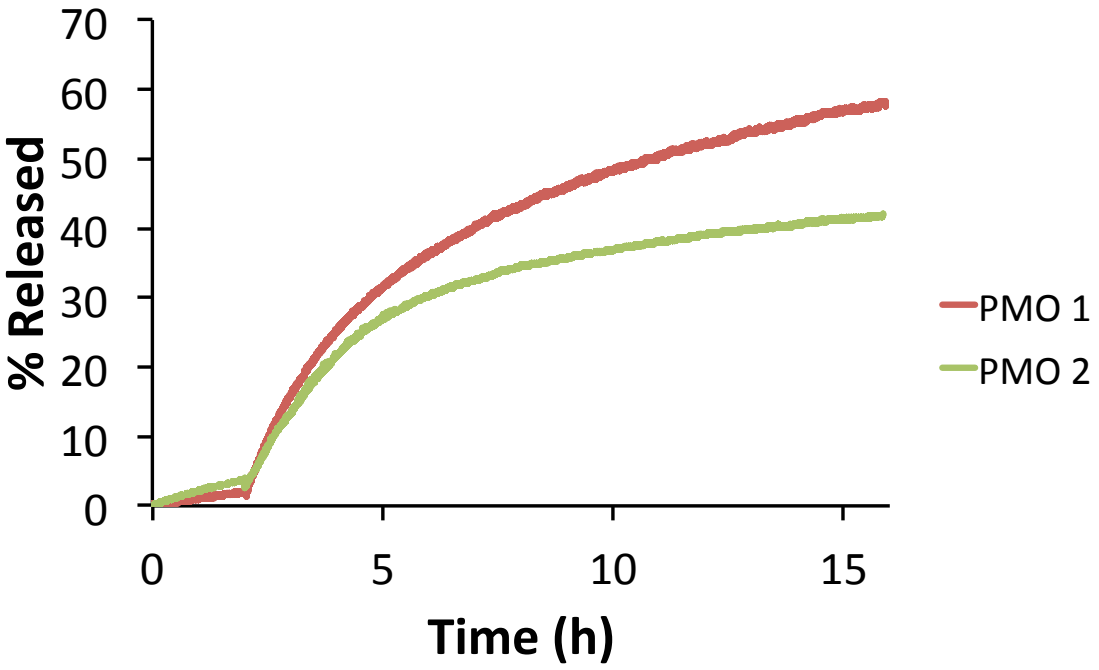

Figure 5.7 Release profiles of PMO 1 (red trace) and PMO 2 (green trace) using Rhodamine B as the cargo.

5.6 References

1. Kresge, C. T.; Leonowicz, M. E.; Roth, W. J.; Vartuli, J. C.; Beck, J. S., Ordered mesoporous molecular sieves synthesized by a liquid-crystal template mechanism. *nature* 1992, 359, 710-712.

2. Klichko, Y.; Liong, M.; Choi, E.; Angelos, S.; Nel, A. E.; Stoddart, J. F.; Tamanoi, F.; Zink, J. I., Mesostructured silica for optical functionality, nanomachines, and drug delivery. *Journal of the American Ceramic Society* 2008, 92, S2-S10.

3. Liong, M.; Lu, J.; Kovochich, M.; Xia, T.; Ruehm, S. G.; Nel, A. E.; Tamanoi, F.; Zink, J. I., Multifunctional inorganic nanoparticles for imaging, targeting, and drug delivery. *Acs Nano* 2008, 2, 889-896.

4. Lu, J.; Liong, M.; Zink, J. I.; Tamanoi, F., Mesoporous silica nanoparticles as a delivery system for hydrophobic anticancer drugs. *Small* 2007, 3, 1341-1346.

5. Beck, J. S.; Vartuli, J. C.; Roth, W. J.; Leonowicz, M. E.; Kresge, C. T.; Schmitt, K. D.; Chu, C. T. W.; Olson, D. H.; Sheppard, E. W., A new family of mesoporous molecular sieves prepared with liquid crystal templates. *Journal of the American Chemical Society* 1992, 114, 10834-10843.

6. Ozin, G. A.; Chomski, E.; Khushalani, D.; MacLachlan, M. J., Mesochemistry. *Current opinion in colloid & interface science* 1998, 3, 181-193.

7. Moller, K.; Bein, T., Inclusion chemistry in periodic mesoporous hosts. *Chemistry of materials* 1998, 10, 2950-2963.

8. Lim, M. H.; Stein, A., Comparative studies of grafting and direct syntheses of inorganic-organic hybrid mesoporous materials. *Chemistry of Materials* 1999, 11, 3285-3295.

9. Lim, M. H.; Blanford, C. F.; Stein, A., Synthesis of ordered microporous silicates with organosulfur surface groups and their applications as solid acid catalysts. *Chemistry of materials* 1998, 10, 467-470.

10. Asefa, T.; MacLachlan, M. J.; Coombs, N.; Ozin, G. A., Periodic mesoporous organosilicas with organic groups inside the channel walls. *Nature* 1999, 402, 867-871.

11. Inagaki, S.; Guan, S.; Fukushima, Y.; Ohsuna, T.; Terasaki, O., Novel mesoporous materials with a uniform distribution of organic groups and inorganic oxide in their frameworks. *Journal of the American Chemical Society* 1999, 121, 9611-9614.

12. Melde, B. J.; Holland, B. T.; Blanford, C. F.; Stein, A., Mesoporous sieves with unified hybrid inorganic/organic frameworks. *Chemistry of materials* 1999, 11, 3302-3308.

13. Hoffmann, F.; Fröba, M., Vitalising porous inorganic silica networks with organic functions—PMOs and related hybrid materials. *Chemical Society Reviews* 2011, 40, 608-620.

14. Guo, W.; Park, J.-Y.; Oh, M.-O.; Jeong, H.-W.; Cho, W.-J.; Kim, I.; Ha, C.-S., Triblock copolymer synthesis of highly ordered large-pore periodic mesoporous organosilicas with the aid of inorganic salts. *Chemistry of materials* 2003, 15, 2295-2298.

15. Muth, O.; Schellbach, C.; Fröba, M., Triblock copolymer assisted synthesis of periodic mesoporous organosilicas (PMOs) with large poresElectronic supplementary information (ESI) available: TG/DTA/MS data. See http://www. rsc. org/suppdata/cc/b1/b106636f. *Chemical Communications* 2001, 2032-2033.

16. Mizoshita, N.; Tani, T.; Inagaki, S., Syntheses, properties and applications of periodic mesoporous organosilicas prepared from bridged organosilane precursors. *Chemical Society Reviews* 2011, 40, 789-800.

17. Burleigh, M. C.; Jayasundera, S.; Spector, M. S.; Thomas, C. W.; Markowitz, M. A.; Gaber, B. P., A new family of copolymers: Multifunctional periodic mesoporous organosilicas. *Chemistry of materials* 2004, 16, 3-5.

18. Hatton, B.; Landskron, K.; Whitnall, W.; Perovic, D.; Ozin, G. A., Past, Present, and Future of Periodic Mesoporous Organosilicas The PMOs. *Accounts of chemical research* 2005, 38, 305-312.

19. Wahab, M. A.; Kim, I.; Ha, C.-S., Bridged amine-functionalized mesoporous organosilica materials from 1, 2-bis (triethoxysilyl) ethane and bis [(3-trimethoxysilyl) propyl] amine. *Journal of Solid State Chemistry* 2004, 177, 3439-3447.

20. Du, L.; Liao, S.; Khatib, H. A.; Stoddart, J. F.; Zink, J. I., Controlled-access hollow mechanized silica nanocontainers. *Journal of the American Chemical Society* 2009, 131, 15136.